

*Improved Mechanical Characterization of Soft, Hydrated,
Heterogeneous Materials for the Design of Tissue
Engineering Scaffolds*

by

ANDREW AURIN TOMASCHKE

B.S., University at Buffalo, 2011

M.S., University of Colorado Boulder, 2019

A thesis submitted to the
Faculty of the Graduate School of the
University of Colorado in partial fulfillment
of the requirement for the degree of
Doctor of Philosophy
Department of Mechanical Engineering
2022

Committee Members:

Virginia L. Ferguson, Ph.D

Frank W. DelRio, Ph.D

Rong Long, Ph.D

Robert R. McLeod, Ph.D

Francois Barthelat, Ph.D

Robert B. MacCurdy, Ph.D

Abstract

Tomaschke, Andrew Aurin (Ph.D., Mechanical Engineering)

Improved Mechanical Characterization of Soft, Hydrated, Heterogeneous Materials for the Design of Tissue Engineering Scaffolds

Thesis directed by Professor Virginia L. Ferguson, Ph.D.

Tissue engineering is a growing discipline that uses a combination of engineering disciplines to develop novel materials and therapeutic strategies for the repair or replacement of damaged tissues and organs. Current strategies typically focus on the development of tissue engineering scaffolds using hydrogels. Scaffolds are application specific and may require interfacing multiple hydrogel materials to mimic the properties of the native tissue. In addition, the resulting design must be mechanically robust so as to withstand physiological loading without failure. Thus, the success of a given application is dependent on 1) the ability to accurately characterize the properties of the native tissue and scaffold materials and 2) the ability to integrate multiple hydrogel materials in a robust manner.

One key challenge is that the influence of surface roughness on the indentation of soft, hydrated materials is poorly understood. Surface roughness is known to influence the properties of traditional engineered materials, but this influence has not been evaluated in the context of soft tissues and hydrogels with rough surfaces. This challenge is addressed through microscale indentation testing of agarose hydrogels, and articular cartilage. The mechanical properties of both rough and smooth surfaces were evaluated using a range of probe sizes,

displacement rates, and indentation depths. Experiments demonstrated that rough surfaces reduce the measured indentation properties by as much as 90%.

Another key challenge is the robust integration of dissimilar hydrogels. Composite hydrogels can be used to tune the properties of a scaffold, but stresses concentrate at the interfaces between materials with dissimilar mechanical properties and may fail under loading. Functionally graded interfaces (FGIs) reduce the property mismatch at the interfaces, but the influence of the width of the FGI on the fracture toughness of hydrogel interfaces. This challenge is first addressed via single edge notch fracture tensile tests of dissimilar polymer interfaces with varying interfacial widths and will subsequently be extended to study dissimilar hydrogel interfaces. Preliminary results demonstrate a strong dependence on the dimensions of the soft phase that may be mitigated through elimination of the stress concentration at the interface between the soft phase and the steel grips used during testing.

Acknowledgments

I would like to express my deepest thanks to my advisor, Dr. Virginia L. Ferguson. Her patience, understanding, hard work, and guidance has been invaluable. Without her willingness to advocate for me and my mental health, none of this work would have been possible. She has helped me grow as a researcher, a writer, and a person. I'm so incredibly thankful for the time I have spent in her lab. I would also like to thank Dr. Frank DelRio for his guidance, advice, and the numerous learning opportunities he has gone out of his way to provide. His commitment to helping others is something I will strive to emulate for the rest of my career.

I would like to thank the other members of my dissertation committee. Dr. Bob McLeod has lent his support from practically day one and has always helped push me to think more deeply about my research. Dr. Rong Long has also been part of my committees since my research prelim and has always made time to give advice. Dr. Francois Barthelat and Dr. Rob MacCurdy have also been invaluable in helping me towards the completion of my Ph.D.

During my time here, I've been part of an amazing lab group and have met countless other fantastic people along the way. Chelsea Heveran, Jenn Coulombe, and Ellyse Schneider, your support has meant the world to me and I'm lucky to call you both friends. Victor Crespo, Bhavya Senwar, Kevin Eckstein, and Kristine Fischenich, thank you for always sharing advice and food, for pushing me to have a little more fun, and for being there to listen to me vent when the going got tough. Diego and Lea, you are both wonderful people and I wish you the best of luck in your Ph.Ds. I would also like to thank Kaitlin McCreery for always being willing to lend a helping hand in my research.

Outside of my research, I would first like to thank Mike Lippert. You're my best friend and you have always had my back. You're probably the sole reason I have a work-life balance and I can't thank you enough for everything you've done for me. You and Jenn are family and always will be. Same goes for Shane Frazier and the rest of the Frazier clan, you guys have always supported me and I'm lucky to have you all in my life.

Last, but certainly not least, I want to thank my family. Dad and Mom, thank you for supporting me through everything. I wouldn't be here without you. Matt, Jon, Greta, Eli, and Ani, you're the best siblings a guy could ask for. Thank you for always making me feel like I'm still part of the family, even when I'm on the other side of the country and buried under a mountain of work.

I would also like to thank the Mechanical Engineering department and my funding sources (NSF MRI Award CBET # 1338154, NSF MRI Award CMMI # 1726864, National Institute of Arthritis and Musculoskeletal and Skin Diseases R01AR069060, Soft Materials Research Center under NSF MRSEC Grant No. DMR-1420736) as well as John Watt and the Center for Integrated Nanotechnologies.

Table of Contents

CHAPTER 1 INTRODUCTION	1
1.1.0 Cartilage	1
1.1.1 Collagen.....	2
1.1.2 Proteoglycans and Glycosaminoglycans	4
1.1.3 Water	5
1.1.4 Chondrocytes	5
1.1.5 Zonal Composition and Organization	6
1.1.6 Mechanical Behavior of Articular Cartilage	8
1.1.7 Osteoarthritis and Therapeutic Approaches	10
1.2.0 Hydrogel Materials	15
1.2.1 General Composition and Structure	16
1.2.2 Classification of Hydrogels.....	16
1.2.3 Mechanical Behavior	18
1.2.4 Composite Hydrogels and Functionally Graded Interfaces.....	22
1.3.0 Indentation.....	24
1.3.1 History and Overview	24
1.3.2 Microindentation of Soft, Hydrated Materials	36
1.3.3 Key Assumptions and Challenges	43
1.3.4 Adhesion.....	44
1.3.5 Surface Roughness	45
1.4.0 Fracture of Graded Hydrogel Interfaces.....	50
1.4.1 Overview of Linear-Elastic Fracture Mechanics, Strain Energy Release Rate	50
1.4.2 Work of Fracture	52
1.4.3 Fracture Modes	54
1.4.4 Fracture of Soft Materials.....	54
1.4.5 Fracture toughness of functionally graded interfaces.....	57
1.5.0 Motivation and Specific Aims	59
1.5.1 Motivation	59
1.5.2 Specific Aims.....	60

1.6.0 References:.....	63
CHAPTER 2 Surface Roughness Influences Microindentation Property Assessment of Agarose Hydrogels	78
2.1.0 Abstract	78
2.2.0 Introduction.....	79
2.3.0 Methods	82
2.3.1 Materials	82
2.3.2 Sample preparation	82
2.3.3 Surface roughness measurements	83
2.3.4 Cryogenic SEM and FIB measurements	84
2.3.5 Microindentation measurements.....	84
2.3.6 Microindentation analysis	86
2.3.7 Unconfined compression.....	88
2.3.8 Statistical analysis.....	88
2.4.0 Results	89
2.4.1 Surface Roughness Measurements	89
2.4.2 Cryogenic FIB and SEM.....	91
2.4.3 Unconfined compression testing.....	92
2.4.4 Microindentation testing.....	93
2.4.5 Statistical Analysis	95
2.5.0 Discussion.....	96
2.6.0 Conclusions.....	100
2.7.0 Conflicts of Interest	101
2.8.0 Author Contributions.....	101
2.9.0 References.....	102
CHAPTER 3 The Influence of Surface Roughness on the Microscale Indentation Behavior of Porcine Articular Cartilage.....	105
3.1.0 Abstract	105
3.2.0 Introduction.....	106
3.3.0 Materials and Methods	108
3.3.1 Sample preparation	108
3.3.2 Preparation of rough and smooth surfaces.....	108
3.3.3 Surface Roughness Measurements	109
3.3.4 Depth-sensing microindentation measurements	110

3.3.5 AFM-based microindentation measurements.....	112
3.3.6 Depth-sensing Microindentation Analysis.....	114
3.3.7 AFM-based Microindentation Analysis.....	115
3.3.8 Statistical Analysis	116
3.4.0 Results	116
3.4.1 Surface Roughness Measurements	116
3.4.2 Depth-sensing Microindentation.....	118
3.4.3 AFM-based Microindentation	120
3.4.4 Statistical Analyses	121
3.5.0 Discussion.....	122
3.6.0 Conclusions.....	125
3.7.0 Conflicts of Interest	125
3.8.0 Author Contributions.....	126
3.9.0 References.....	126
CHAPTER 4 Fracture Toughness of Functionally Graded Interfaces Between Polymeric Materials with Divergent Mechanical Properties	129
4.1.0 Abstract	129
4.2.0 Introduction.....	130
4.3.0 Materials and Methods	132
4.3.1.A Materials for Study A.....	132
4.3.1.B Materials for Study B.....	132
4.3.2.A Samples for Notch Fracture Testing – Study A	133
4.3.2.B Samples for Notch Fracture Testing – Study B	134
4.3.3.A Notching of Samples – Study A.....	135
4.3.3.B Notching of Samples – Study B.....	135
4.3.4 Notch Fracture Testing – Study A	136
4.3.4 Notch Fracture Testing – Study B	136
4.3.5 Work of Fracture Analysis – Study A and Study B.....	136
4.4.0.A Results – Study A.....	137
4.4.1.A Notching – Study A.....	138
4.4.2.A Fracture Testing – Study A	139
4.4.0.B Results – Study B	141
4.4.1.B Notching – Study B	141

4.4.2.B Fracture Testing – Study B.....	141
4.5.0 Discussion.....	142
4.5.1 FGIs vs. Bi-material Interfaces	143
4.5.2 Influence of the Soft Phase.....	144
4.5.3 Crack Propagation Behavior	146
4.6.0 Limitations.....	150
4.7.0 Conclusions.....	151
4.8.0 Conflicts of Interest	151
4.9.0 Author Contributions.....	151
4.10.0 References.....	152
Chapter 5 Conclusions.....	155
5.1 Overview	155
5.1 Summary of Results.....	156
5.2 Discussion of future research directions	160
5.2.1 Experiments to further elucidate the influence of surface roughness on indentation of soft, hydrated materials.....	160
5.2.2 Translational considerations	161
5.2.3 Further fracture testing experiments	161
Bibliography	162

List of Tables

Chapter 2

Table 2. 1 <i>Measured Surface Roughness Parameters of 10 wt. % agarose samples</i>	90
--	----

Chapter 3

Table 3. 1 <i>Measured Surface Roughness Parameters</i>	118
--	-----

List of Figures

Chapter 1

Figure 1. 1 Structure of the Osteochondral unit and the unit's individual components.	2
Figure 1. 2 Articular Cartilage Zonal Composition & Organization	7
Figure 1. 3 Evolution of total stress and interstitial fluid pressure of articular cartilage during a stress-relaxation test.	10
Figure 1. 4 Illustration of Healthy (Lateral condyle) versus Osteoarthritic (medial condyle) articular cartilage..	12
Figure 1. 5 Surgical strategies for repair of focal defects.	14
Figure 1. 6 Different types of cross-linking in hydrogels.	18
Figure 1. 7 Viscoelastic response associated with step loading and unloading.	19
Figure 1. 8 Creep response following step loading and Stress relaxation response following step deformation	20
Figure 1. 9 Apparent stiffening of 10 wt. % agarose with increasing indentation rate.....	21
Figure 1. 10 Schematic depicting the abrupt change in material properties at a bi-material interface and a more gradual change in material properties with the inclusion of functionally graded interface	24
Figure 1. 11 Illustration of increasing size of interference fringes with increasing applied load	25
Figure 1. 12 Schematic representation of deformation processes during loading and unloading of a conical indenter.....	28
Figure 1. 13 Schematic depicting extrapolation of the initial portion of the unloading curve..	30
Figure 1. 14 Schematic representation of a cross-section of an indent with relevant quantities labeled..	31
Figure 1. 15 Schematic depicting the effective indenter shape..	34

Figure 1. 16 Schematic depicting the cross-section of a spherical indentation with relevant quantities used in Hertz Elastic Contact Theory labeled.	35
Figure 1. 17 Evolution of fluid load support with increasing Peclet number.	42
Figure 1. 18 Sample force curves in air, water, and detergent.....	45
Figure 1. 19 Schematic depicting contact between a spherical probe and a rough surface.	46
Figure 1. 20 Schematic depicting the change in potential energy with crack propagation	51
Figure 1. 21 Fracture Modes.	54
Figure 1. 22 Illustration of Mode I fracture of a soft, energy-dissipating material.	56
Chapter 2	
Figure 2. 1 Sample Preparation: Workflow to Produce Rough & Smooth surfaces.....	83
Figure 2. 2 Load Functions and Representative curves for 10 wt% Agarose.	85
Figure 2. 3 10 wt. % Agarose Surface Roughness measurements	90
Figure 2. 4 Images from Cyro FIB & SEM of 10 wt. % agarose.	92
Figure 2. 5 Measurands from Indentation testing of 10 wt% Agarose.....	94
Chapter 3	
Figure 3. 1 Sample harvesting and preparation of rough and smooth surfaces.	109
Figure 3. 2 Depth-sensing Microindentation Load Functions and Representative Curves.	112
Figure 3. 3 Representative Curves from AFM-based microndentation.....	114
Figure 3. 4 Representative Areas Used in Surface Roughness Measurements.....	117
Figure 3. 5 Depth-Sensing Microindentation Results.....	120
Figure 3. 6 AFM-Based Microindentation Results	121
Chapter 4	
Figure 4. 1 Study A Designs.....	134
Figure 4. 2 Study B Designs.....	135

Figure 4. 3 Images of the initial crack lengths 139

Figure 4. 4 Load vs. Extension curves from fracture testing of samples from Study A. 140

Figure 4. 5 Load vs. Extension curves from fracture testing of samples from Study B. 142

Figure 4. 6 Crack propagation behavior of samples from Study A 149

Figure 4. 7 Crack propagation behavior of samples from Study B 150

CHAPTER 1

INTRODUCTION

1.1.0 Cartilage

Articular cartilage covers the articulating ends of long bones. to provide smooth, lubricated articulation of joints (e.g., knees, hips) and resist the various compressive and shearing forces encountered during daily activities. It has a multiphasic composition, consisting of an extracellular matrix (ECM), the fluid that resides within the interfibrillar spaces of the ECM, ions which serve to bind the interstitial fluid to the ECM, and chondrocytes, which are responsible for the synthesis of the ECM. The ECM itself is composed of several types of collagens, proteoglycans, and various other non-collagenous proteins and glycoproteins (Fig. 1.1). Together, the various nano- and microscale components and different phases interact to form a multi-scale hierarchy and grant articular cartilage with its excellent wear resistance and compressive properties under physiological loading. Furthermore, when the integrity of the tissue is disrupted, the microscale changes to composition and structure lead to striking changes in articular cartilage's macroscopic mechanical function. The link between microscale composition/organization and macroscopic mechanical properties has inspired an entire field of research dedicated to using small scale property assessments to understand the link to macroscale tissue properties.

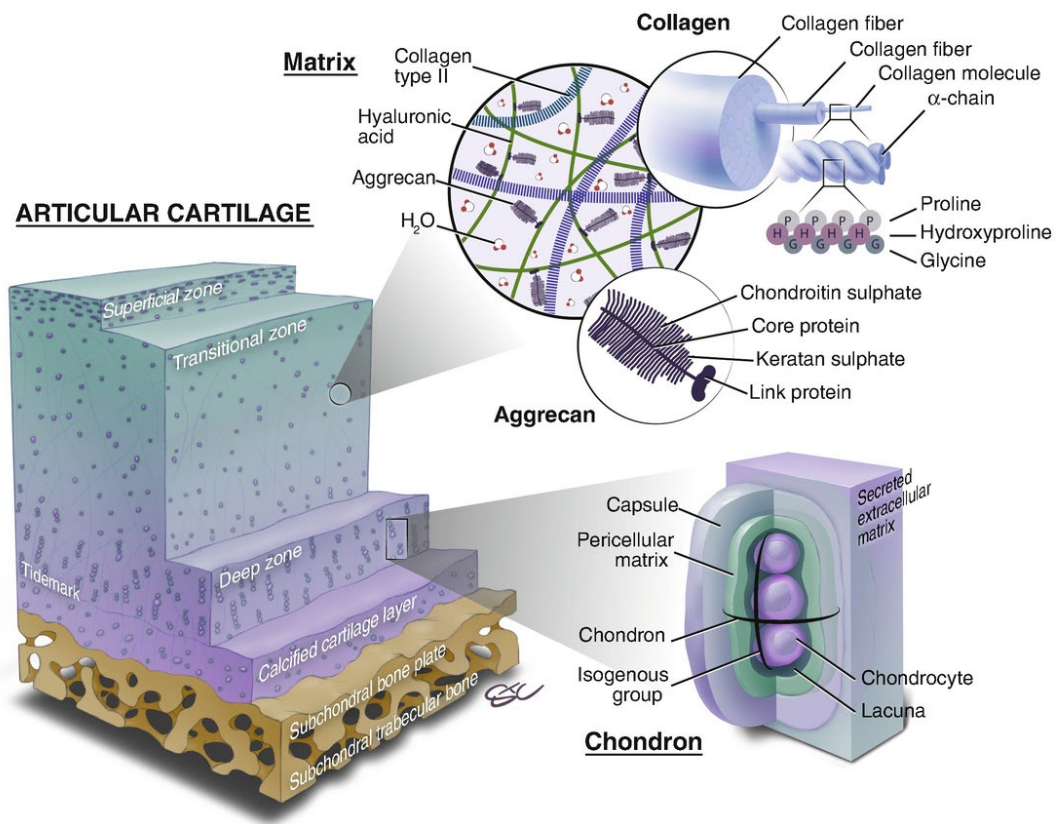


Figure 1. 1 Structure of the Osteochondral unit and the unit's individual components. Reprinted/adapted by permission from Springer Nature Customer Service Centre GmbH: Springer Joint Preservation of the Knee by Adam B. Yanke and Brian J. Cole Springer Nature Switzerland AG (2019)

1.1.1 Collagen

Collagen accounts for the bulk of the ECM, making up approximately 60% of the dry weight of articular cartilage. Multiple types of cartilage are found in the ECM, including types II, VI, X, and XI¹. Of these, type II collagen is the most-abundant, accounting for 90-95% of the total collagen¹. Type II collagen, in conjunction with types IX & XI, forms the cross-banded collagen fibrils that provide the structure for the ECM as well as the interfibrillar spaces for macromolecules like proteoglycans. The type II collagen molecule is composed of three α_1 chains that wrap around one another to form a triple helix. The ends of the triple helix provide sites for cross-links to form. Cross-links can either be intramolecular (Type II linking with type II)

or intermolecular (Type II linking with type IX or type XI). Type IX collagen makes up 1% to 5% of the total collagen content and binds covalently to cross-banded collagen fibrils, helping to stabilize the collagen network². Type XI collagen, which accounts for approximately 3% of the total collagen content, binds covalently to type II collagen and may help regulate cartilage formation³.

Other types of collagen, such as types VI and X, are much less abundant, but still serve important roles. Type VI makes up less than 1% of the total collagen content and is found in the ECM in close vicinity to chondrocytes. Type VI collagen is able to bind to a wide variety of ECM proteins, and forms networks that serve to anchor chondrocytes to the pericellular matrix (PCM) in articular cartilage and may be an important part of chondrocyte mechanosensing⁴. Type X also makes up less than 1% of the total collagen content⁵. This type of collagen is produced by mature hypertrophic chondrocytes and is believed to play a key role in modifying the cartilage matrix for subsequent endochondral ossification⁶.

Collagen's primary function may be to maintain the shape of the tissue by resisting the internal swelling pressure, but it also contributes to cartilage's resistance to deformation under loading⁷. As an example, under indentation loading, collagen fibers oriented parallel to the surface are pulled into tension to resist further deformation of the material surface⁸. The disruption of the collagen network, and the subsequent drop in bulk mechanical stiffness, is considered a hallmark of osteoarthritis^{9,10}.

1.1.2 Proteoglycans and Glycosaminoglycans

Proteoglycans are the second most abundant component of the ECM, accounting for approximately 20-30% of the total dry weight. Proteoglycans are macromolecules and consist of one or more glycosaminoglycans (GAGs) chains covalently attached to a core protein. There are several types of GAGs, including hyaluronic acid, chondroitin sulfate, keratan sulfate, and dermatan sulfate¹. Each GAG is composed repeating disaccharides, and each unit of disaccharide has at least one negatively charged carboxylate or sulfate group. As a result, GAGs form long strings of negative charges that repel other GAGs while attracting cations and water molecules.

While proteoglycans come in several forms, including decorin, biglycan, and fibromodulin, the most common proteoglycan is aggrecan, which makes up greater than 90% of the proteoglycans found in articular cartilage. Aggrecan possesses upwards of 100 chondroitin sulfinate and keratan sulfate chains¹¹, and therefore a large negative charge. Aggrecan molecules are defined by their interaction with hyaluronic acid and link proteins to form large aggregates with as many as 300 associated aggrecan molecules per aggregate¹. These large aggregates help physically confine proteoglycans within the interfibrillar space of the ECM and grant cartilage its osmotic properties.

The concentration of confined proteoglycan aggregates results in a localized negative charge, typically referred to as the fixed charge density (FCD). To maintain local electro-neutrality, ions dissolved in the interstitial fluid are attracted to the proteoglycan aggregates, which in-turn creates an ion imbalance between the interstitial and external fluid¹². The imbalance in ions creates an influx of water into the tissue, referred to as the Donnan osmotic

pressure¹³. The internal swelling pressure holds the collagen network in tension and acts to resist compressive loads. Additionally, it has been demonstrated that permeability decreases with increasing proteoglycan concentration¹⁴. Thus, under dynamic loading, the presence of proteoglycan aggregates resists interstitial fluid flow, gives rise to larger interstitial fluid pressures, and as a result, contributes to cartilage's resistance to compression.

1.1.3 Water

Water resides within the interfibrillar spaces of the ECM and makes up approximately 80% of the wet weight of articular cartilage. The water residing within the ECM of articular cartilage contains various components, including gases, small proteins, metabolites, and a high concentration of cations to balance the negative charges created by the large aggregates of proteoglycans¹. There are two types of water found within the ECM: bound and free water. Free water is responsible for solute transport into and out of mature tissue which provides nutrition to the chondrocytes, as well as solutes required to maintain the chemical and mechanical environments¹⁵. Bound water, as the name implies, is bound to the extracellular matrix as a function of attraction between the positively charged cations present in the water, and the negatively charged proteoglycan aggregates found in the interfibrillar spaces of the ECM. The bound water creates an osmotic pressure which pulls the collagen network into tension¹ as well as frictional drag when the water is squeezed through the ECM under loading¹¹, granting cartilage with its unique ability resist large compressive loads¹⁶.

1.1.4 Chondrocytes

Chondrocytes are the only type of cell found in articular cartilage and make up approximately 2% of the total articular cartilage volume. Chondrocytes, like osteocytes,

neurons, myocytes, and adipocytes, differentiate from mesenchymal stem cells under specific conditions. These highly specialized chondrocyte cells are responsible for the development and maintenance of the ECM in their immediate vicinity. During development, chondrocytes produce new ECM to expand and remodel the articular surface covering the ends of long bones. In this stage, chondrocytes are densely packed, have a high level of metabolic activity, and proliferate rapidly in order to rapidly form new ECM. As the skeleton matures, metabolic activity, ECM production, and cell proliferation all decline and once skeletal maturity is reached, chondrocytes become extremely limited in their capacity to replicate and proliferate, which is, in part, responsible for articular cartilages limited healing capacity^{1,11}. In this stage, chondrocytes will continue to turn over the ECM provided that an optimal chemical and mechanical environment is maintained. Damage to articular cartilage as a result of injury or aging disrupts the mechanical environment, limiting the ability of chondrocytes to respond to stimuli and maintain tissue, thus further contributing to the degeneration of cartilage with aging and disease⁹.

1.1.5 Zonal Composition and Organization

The relative amounts of each constituent and its organization varies with depth. These variations are grouped into three different zones: superficial, middle, and deep (Fig. 1.2). The specific organization and concentration of the individual constituents imparts the three different zones with the ability to resist the various forces imparted on the articular cartilage macrostructure.

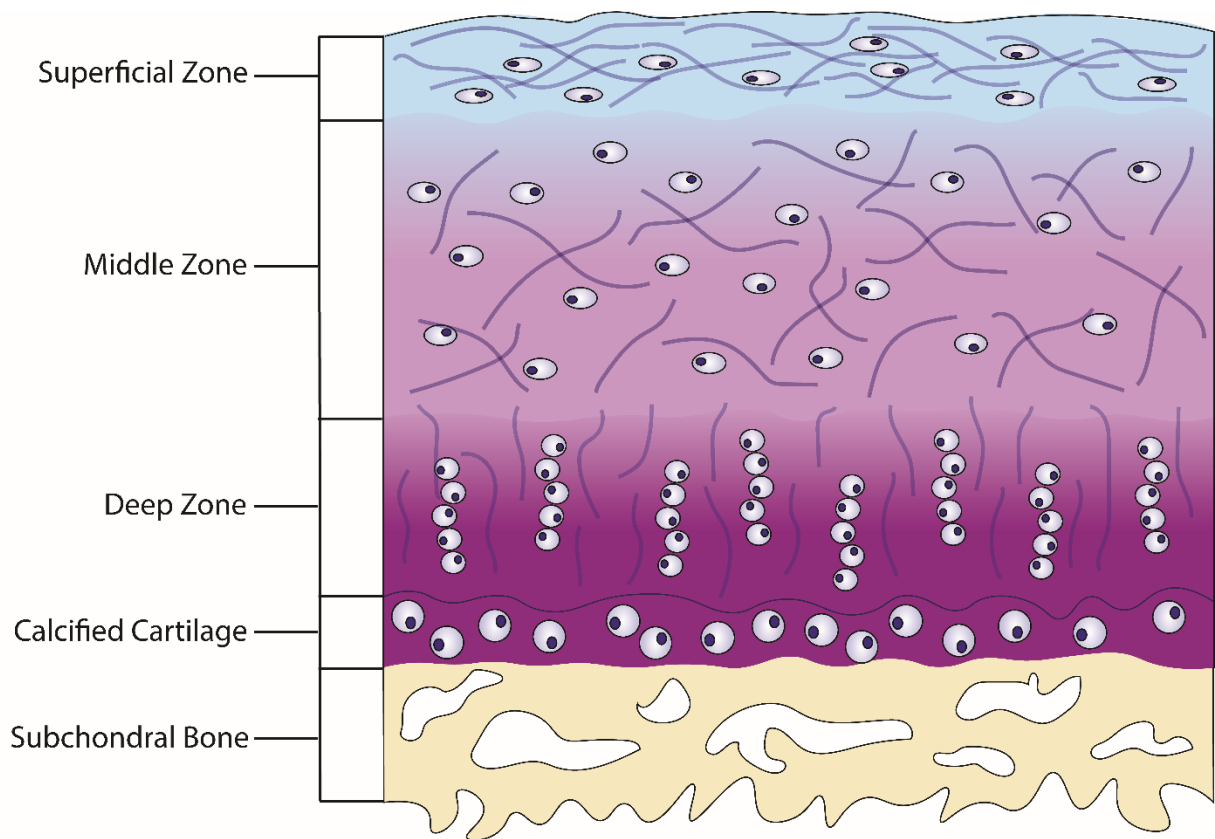


Figure 1. 2 Articular Cartilage Zonal Composition & Organization

osteoarthritis, increasing permeability, and decreasing tensile strength, which leads to further damage and degradation¹⁷.

The middle zone lies directly below the superficial zone and makes up the largest fraction of the overall structure, representing 40% to 60% of the total cartilage thickness^{1,11}. Collagen is less abundant in the middle zone as compared to the superficial zone, and fibrils are more randomly arranged than in the superficial zone, but the fibril diameters are much thicker. The concentration of water is also lower than that of the superficial zone. In contrast to collagen and water, proteoglycan content is highest in the middle zone. The middle zone acts as the first line of defense against external compressive loads.

The deep zone makes up the remainder of articular cartilage's thickness, representing approximately 30% of the total thickness. The deep zone contains the largest-diameter collagen fibrils, which are oriented perpendicular to the articular surface and anchored into the underlying calcified cartilage¹. While proteoglycan content is lower than in the middle zone, the lower water content provides the deep zone with the highest FCD^{14,18,19}. The result is a zone with the highest compressive stiffness of any of the three zones^{19,20}.

1.1.6 Mechanical Behavior of Articular Cartilage

The mechanical behavior of cartilage is best described as a biphasic material, where the two phases are the solid matrix and the water residing within it²¹⁻²³. Biphasic theory models cartilage as a composite material made up of two phases, a solid phase representing the collagen-proteoglycan matrix, and a fluid phase representing the water residing within the matrix. In this model, the solid phase is permeable to the fluid phase. Thus, when the tissue is

loaded, the applied load is counteracted by the stress in solid matrix, the fluid pressure generated in the fluid phase, and the frictional drag created as the fluid moves through the solid matrix. The pressurization of the interfibrillar fluid and frictional drag drive articular cartilage's time dependence and is referred to either as biphasic or poroelastic behavior, where the prefix "poro-" describes the time-dependence resulting from the fluid phase, and the suffix "-elastic", describes the elastic response of the solid matrix. Articular cartilage has a very low permeability²⁴ (i.e., fluid movement throughout the matrix is restricted and tortuous), thus resulting in large interstitial pressures and slow dissipation of under compressive loading²⁵ (Fig. 1.3). These large interstitial pressures and slow dissipation endow cartilage with its excellent compressive stiffness. Studies of articular cartilage's biphasic mechanical behavior have demonstrated that the interstitial fluid pressure generated under loading is capable of supporting over 80% of the applied load^{22,23,25}. This mechanism has been claimed to shield the solid matrix from damage during strenuous physical activities like running and jumping, thus protecting the tissue from damage, and maintaining an optimal mechanical environment for chondrocyte health^{26,27}.

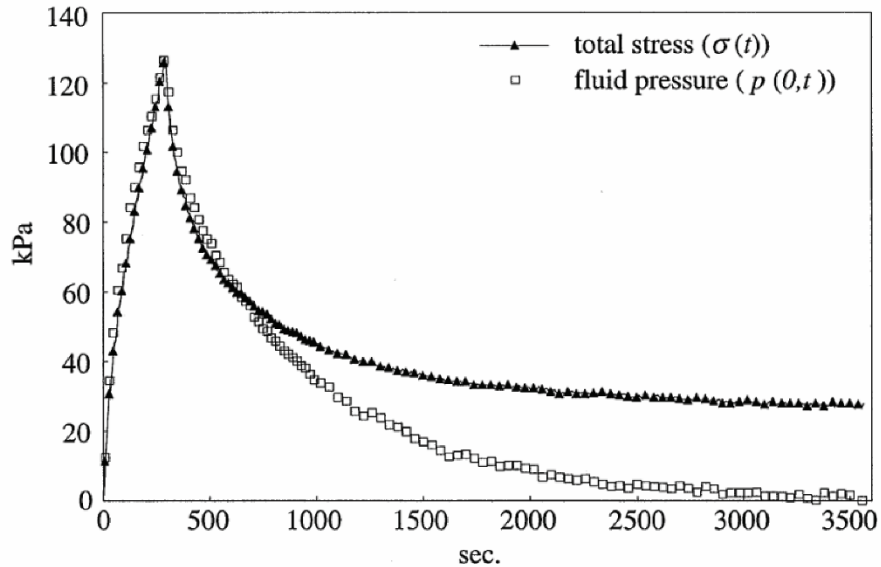


Figure 1. 3 Evolution of total stress and interstitial fluid pressure of articular cartilage during a stress-relaxation test. Figure reprinted from (Soltz & Ateshian, 1998) under CC license BY-NC-ND 4.0

While the mechanical behavior of cartilage appears to be well represented by biphasic theory, this approach is more empirical than mechanistic. Most notably, biphasic theory ignores the FCD and the resulting Donnan osmotic pressure^{13,28}. If the FCD and the Donnan osmotic pressure are not accounted for, such as with biphasic theory, any measured properties will be the “apparent properties” of the tissue, i.e., the properties are specific to the environment that the tissue is residing in^{29,30}. Triphasic theory was developed to consider the FCD and describes the intrinsic properties of the tissue, i.e., the properties of the tissue in absence of any osmotic pressure effects^{29,30}. Measurements using triphasic theory require additional experiments in the form of testing in a hypertonic environment or biochemical assays, which may explain why biphasic theory is still commonly utilized^{22,23,31–33}.

1.1.7 Osteoarthritis and Therapeutic Approaches

Osteoarthritis (OA) is a painful and debilitating degenerative joint disease affecting over 32.5 million US adults, according to the Center for Disease Control. The onset of OA results

from either chronic or acute mechanical damage to articular cartilage. Chronic damage can be caused altered loading as a result of meniscal tears³⁴, obesity³⁵⁻⁴⁰, aging^{41,42}, varus malalignment (i.e., bow-legged)^{43,44}, as well as other conditions including uncorrected congenital dysplasia⁴⁵ and femoroacetabular impingement (FAI)⁴⁶⁻⁴⁸. Acute mechanical damage takes the form of focal lesions that typically occur during traumatic joint injuries, such as tearing of the anterior cruciate ligament (ACL)⁴⁹. In other tissue types, minor damage would heal on its own. Cartilage, on the other hand, is avascular and aneural, and therefore possesses only a limited capacity for self-healing¹.

The inability of articular cartilage to repair itself leads to further degradation if left untreated. As an example, onset of OA in the knee is typically accompanied by malalignment of the joint. The malalignment of the knee alters physiological loading, creating a narrowed area near the medial or lateral condyle, depending on whether the malalignment is varus or valgus. The cartilage in the narrowed region of the knee is subjected to increased loading as compared to neutrally aligned knees, leading to increased cartilage damage and fibrillation of the articular surface^{10,50}. Damaged cartilage undergoes decreased compressive stiffness^{51,52}, thus increasing strain in the cartilage under loading to further overload chondrocytes and damage the tissue. The increased loading also transmits more of the load to the underlying bone, which may lead to more malalignment, further joint narrowing, increased focal stresses, and additional cartilage damage⁵³. Without intervention, this feedback loop continues unchecked and eventually leads to painful bone on bone contact (Fig. 1.4).

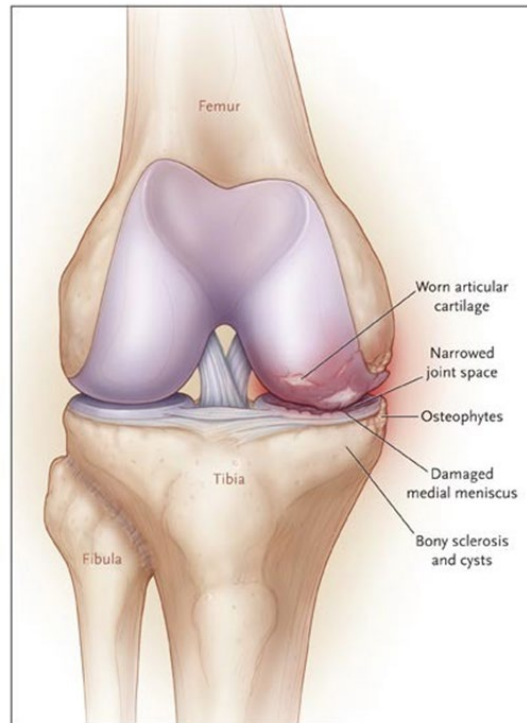


Figure 1. 4 Illustration of Healthy (Lateral condyle) versus Osteoarthritic (medial condyle) articular cartilage. Reproduced with permission from (Felson, 2006), Copyright Massachusetts Medical Society.

Current treatments which attempt to halt the progression of OA vary in both invasiveness and efficacy. The least invasive and least effective method of treatment is oral medication in the form of traditional anti-inflammatory drugs, glucosamine supplements, and chondroitin sulfate supplements. Anti-inflammatory drugs only mask symptoms^{54,55}, while the efficacy of supplements is, at most, described as a mild positive effect⁵⁶⁻⁵⁸. An alternative, and more invasive approach is to rid the joints of debris created in the early stages of OA. While the effectiveness of the treatment is debatable⁵⁹⁻⁶² this treatment does not repair the injured tissue. Similarly, others have attempted to remove fibrillated cartilage surrounding osteochondral defects using shaving, debridement, or laser ablation. However, unlike debris removal, this approach has been largely debunked. Studies that used shaving and debridement

showed no improvement or further damage to the cartilage surrounding defects⁶³⁻⁶⁶, and studies that used laser ablation demonstrated no positive outcomes^{67,68}.

In addition to treatments strictly focused on halting the progression of OA, a variety of treatments focus on repairing the damaged cartilage. One such strategy for repairing the injured cartilage is to invoke the body's natural clotting and fibrocartilage response via microfracture (Fig 1.5a). This procedure is typically performed arthroscopically, using an awl to punch small holes into the subchondral bone beneath the defect. The holes allow bone marrow to flow into the damaged cartilage and results in the formation of fibrocartilage within the osteochondral defect⁶⁹. While this procedure has demonstrated short-term efficacy⁷⁰⁻⁷³, fibrocartilage is mechanically inferior to that of articular cartilage⁷⁴⁻⁷⁶, leading to worsening clinical outcomes when evaluated 18-24 months after surgery⁷⁷. Autologous chondrocyte implantation (ACI) is another method that attempts to repair defects in the cartilage tissue. In this two-part procedure, a cartilage biopsy is performed to harvest native chondrocytes. These chondrocytes are then cultured for six to eight weeks to allow proliferation. Lastly, the cultured cells are inserted into the cartilage defect allowing, in theory, the chondrocytes to produce new tissue inside of the defect. Studies show mixed results regarding the efficacy of ACI with some studies claiming better outcomes⁷⁸⁻⁸⁰ while others show no statistically significant difference^{81,82} or worse outcomes as compared to microfracture^{70,77}. Similar to ACI, osteochondral autografts harvest healthy tissue with the goal of repairing the cartilage defect (Fig 1.5b). However, in this procedure, full thickness osteochondral plugs are taken from a non-load-bearing region of the joint. The repair site is then prepared by removing the damaged cartilage and underlying bone. The resulting hole is filled with one or more osteochondral plugs

that, ideally, will integrate with the surrounding healthy tissue. While theoretically sound from a mechanics standpoint, some studies have shown that cartilage may begin to degrade at the tissue harvest sites, ultimately only delaying the onset of OA⁸³⁻⁸⁹.

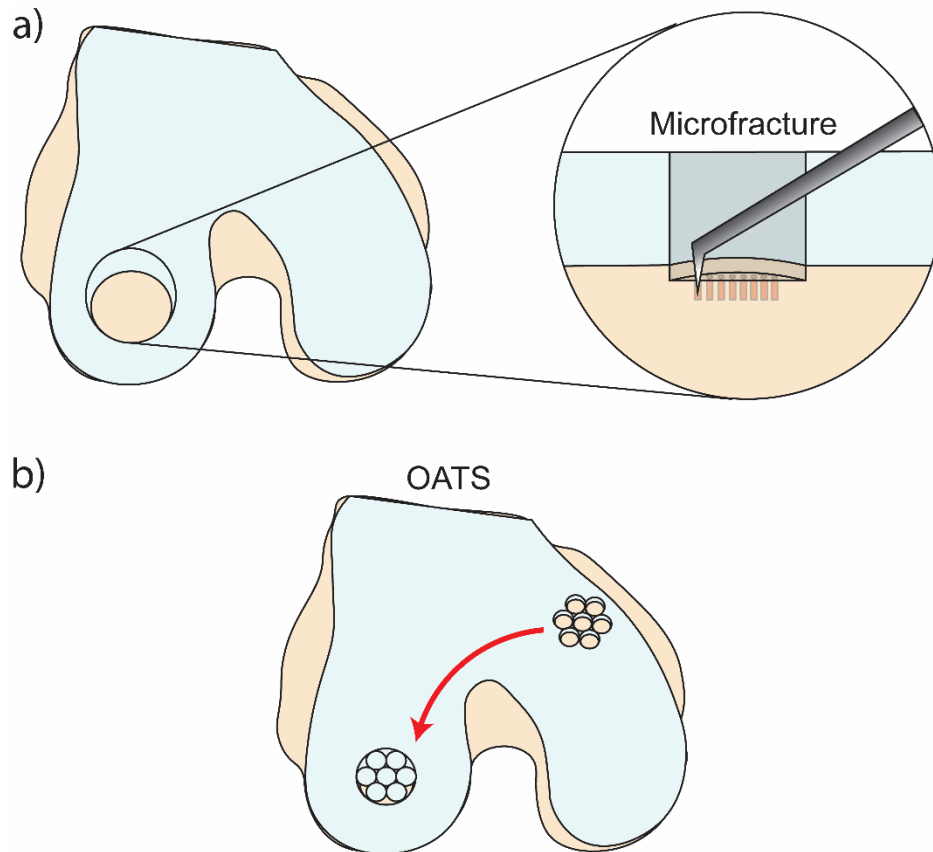


Figure 1. 5 Surgical strategies for repair of focal defects. **a)** Microfracture **b)** Osteochondral autograph transfer system (OATS)

The most intensive treatment for osteoarthritis is a total joint replacement. Total joint replacements are often used as a last resort, to relieve pain and improve mobility in late-stage OA. This treatment is a surgical procedure in which parts of the arthritic joint are removed and replaced with a prosthesis that is designed to restore movement and function to the affected joint⁹⁰. The invasiveness of this procedure results in long recovery times as in addition to the

trauma from surgery, the immobilized muscles surrounding are weakened⁹⁰. Furthermore, total joint replacements have a revision rate of approximately 6% at 5 years and 12% at 10 years⁹¹.

The lack of less invasive, effective, treatment options has spawned an entire field of research which seeks to use tissue engineering scaffolds to repair focal defects and halt OA before it even begins. Some strategies focus solely on putting components into the defect that are capable of producing new tissue and integrating with existing tissue⁹²⁻⁹⁶ while others focus on the matching the mechanical properties of the scaffold to native cartilage with the goal of restoring mechanical function⁹⁷⁻¹⁰¹. Recently, some have sought to combine these strategies, creating mechanically robust scaffolds which degrade over time as new tissue is produced inside of the defect¹⁰²⁻¹⁰⁴. Despite the variety of strategies, the approaches share a common element in the incorporation of hydrogel materials. The long-term success of hydrogel-based approaches will depend on the short-term ability to restore mechanical function to the tissue and the long-term ability to regenerate tissue with native mechanical properties. One obstacle to achieving both short-term and long-term goals is the lack of microscale property data of human cartilage required to design biomimetic scaffolds and evaluate quality of repair tissue. Thus, there is a critical need to accurately characterize the microscale mechanical properties of healthy, human, articular cartilage.

1.2.0 Hydrogel Materials

Hydrogels were discovered over 60 years ago and were first reported Wichterle and Lím¹⁰⁵. Since their discovery, hydrogels have garnered interest due to their unique structure and properties^{106,107}. This interest has steadily increased over time, as researchers have

discovered promising potential applications of different hydrogels for use in tissue engineering and targeted drug delivery.

1.2.1 General Composition and Structure

Hydrogels are porous, polymeric networks capable of retaining large volumes of water relative to the volume occupied by the polymeric network, often containing water volume fractions upwards of 70%^{107,108}. Hydrogels are given their structure/shape through the interaction of water with hydrophilic functional groups attached to a polymeric backbone. The hydrophilic functional groups attract water molecules, which pulls polymer chains into tension as the network swells, granting the hydrogel its solid shape^{107,108}.

1.2.2 Classification of Hydrogels

The term “hydrogel” encompasses a wide range of different materials with vastly different compositions, structures, and properties; thus, it is important to understand how hydrogels are classified. Most frequently, hydrogels are classified according to the origins of the polymer network, the method of preparation, and type of cross-linking. These factors need to be taken into consideration when designing materials that mimic the quasi-static mechanical properties and dynamic behavior of native tissues, including articular cartilage.

The origins of the polymeric network can be grouped into either synthetic or natural. Synthetic hydrogels, as the name implies, possess networks of synthetic polymer chains whereas natural hydrogels are made up of natural polymers including protein polymers and polysaccharide polymers. The most common examples of synthetic hydrogels include poly(2-hydroxyethyl methacrylate) (PHEMA), poly(vinyl alcohol) (PVA), polyethylene glycol (PEG),

poly(acrylic acid) (PAA), poly (methyl methacrylate) (PMMA), and polyacrylamide (PAAm). The most common natural hydrogels include hyaluronic acid, chitosan, alginate, and agarose.

The method of preparation can be grouped into one of three categories: homopolymeric, copolymeric, and Interpenetrating networks (IPNs). Homopolymeric hydrogels, such as agarose, possess networks composed of a single species of monomer¹⁰⁷⁻¹⁰⁹. Copolymeric hydrogels are composed of two or more species of monomer, where at least species must be hydrophilic so as to retain fluid within the polymeric network¹⁰⁷⁻¹⁰⁹. Lastly, IPNs consist of two networks that interpenetrate one another, but are independently cross-linked^{107,108}.

The type of cross-linking can be described as either chemical or physical (Fig. 1.6). Chemical hydrogels, such as PEG, possess cross-linked networks consisting of permanent, covalent bonds between polymer chains¹⁰⁷⁻¹⁰⁹. Physical hydrogels have networks consisting of reversible cross-links created through ionic interactions, hydrogen bonding, hydrophobic interactions, or more commonly, through physical entanglements¹⁰⁷⁻¹⁰⁹. Agarose, a hydrogel formed through physical entanglements of polymer chains, is therefore classified as a physical hydrogel¹¹⁰. From the perspective of mechanical characterization, the type of cross-linking is perhaps the most important classification, as it can be used to predict how a hydrogel behaves under mechanical loading¹⁰⁸.

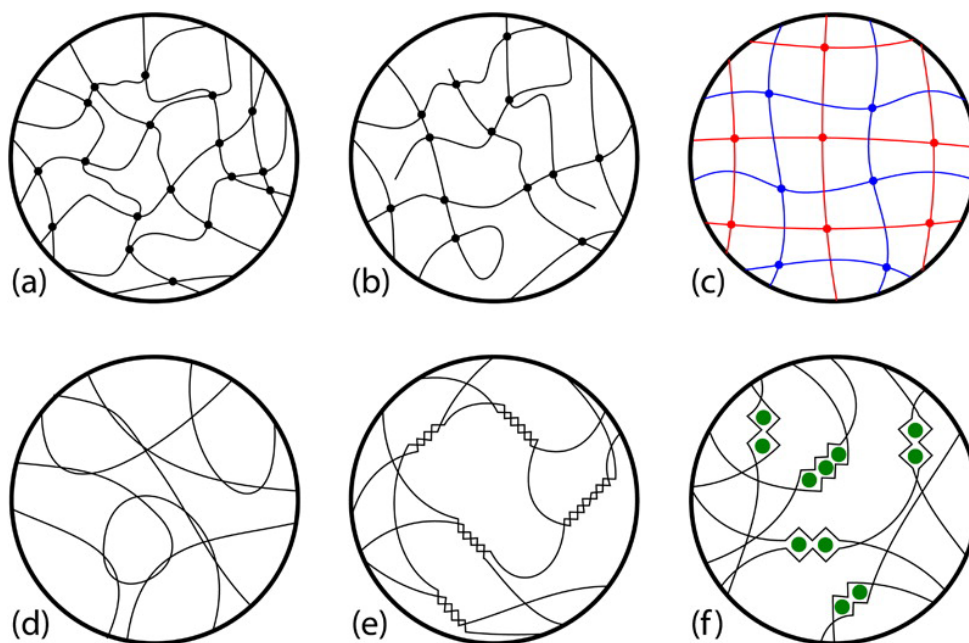


Figure 1. 6 Different types of cross-linking in hydrogels. **a)** Ideal chemical cross-linking **b)** Non-ideal chemical cross-linking **c)** Interpenetrating networks **d)** Physical cross-linking via entanglement **e)** Physical cross-linking via formation of helices **f)** Physical cross-linking via ionic interactions (Oyen, 2013)

1.2.3 Mechanical Behavior

Depending on the type, and relative degree of cross-linking, the mechanical behavior of a hydrogel can be described as either hyperelastic, viscoelastic, or poroelastic. Physical gels demonstrate viscoelasticity and/or poroelasticity, owing to the non-permanence of their physical entanglements and ionic bonds. Whereas chemical gels typically display poroelastic or hyperelastic behavior, owing to the permanence and immobility of the chemical crosslinks. The mechanical behavior can only be described as hyperelastic when a chemical hydrogel possesses a high degree of cross-linking, such as found in PVA hydrogels¹¹¹ or polyampholytic gelatin hydrogels¹¹². The majority of hydrogels are time-dependent and cannot be treated as hyperelastic. Instead, the mechanical behavior is best described as viscoelastic, poroelastic, or a combination of the two behaviors, typically referred to as poro-viscoelastic.

Viscoelasticity describes the mechanical behavior of a material that exhibits a combination of both elastic and viscous deformation. Elastic deformation occurs instantly upon application of an external load, and that same deformation is recovered instantaneously once the load is removed. Viscous deformation depends on the rate of application of the externally applied load and the recovery of the resulting deformation occurs over time (Fig. 1.7).

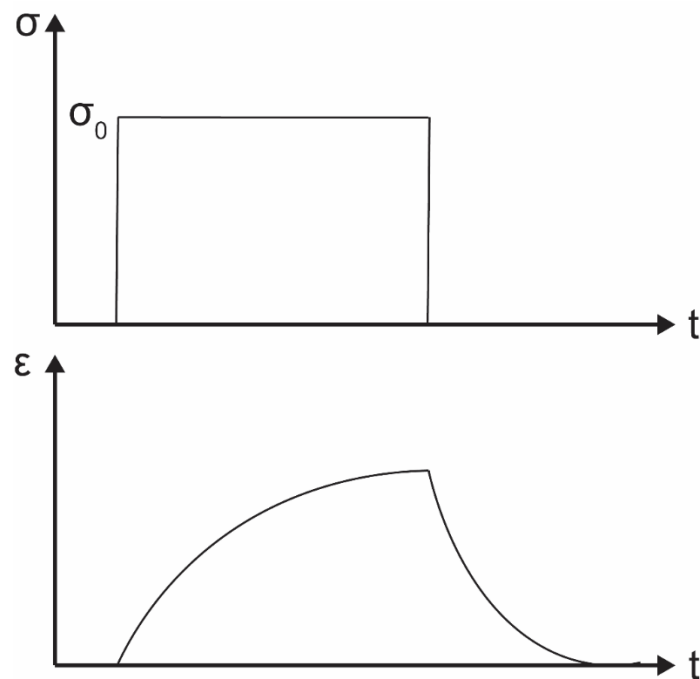


Figure 1. 7 Viscoelastic response associated with step loading and unloading.

If a load is applied faster than the characteristic time it takes for the polymer network to rearrange and relax, no energy is dissipated by relaxation of the polymer network, and the material will appear stiffer (i.e., small deformation with applied load). Whereas if the load is applied slowly, the network is able to rearrange and dissipate energy, and so the material appears softer. Viscoelastic behavior is most evident in creep and stress-relaxation tests (Fig. 1.8). In a stress relaxation test, a specified strain is applied and held. Initially there is a stress

that results from the applied strain. However, as the strain is held, the network is able to rearrange and the stress-relaxes to an equilibrium stress associated with the elastic behavior of the material. Creep tests are similar to stress-relaxation, with the exception that a constant stress is maintained instead of a constant strain. When a constant stress is held, the material will continue to deform until an equilibrium strain associated with the elastic properties of the material.

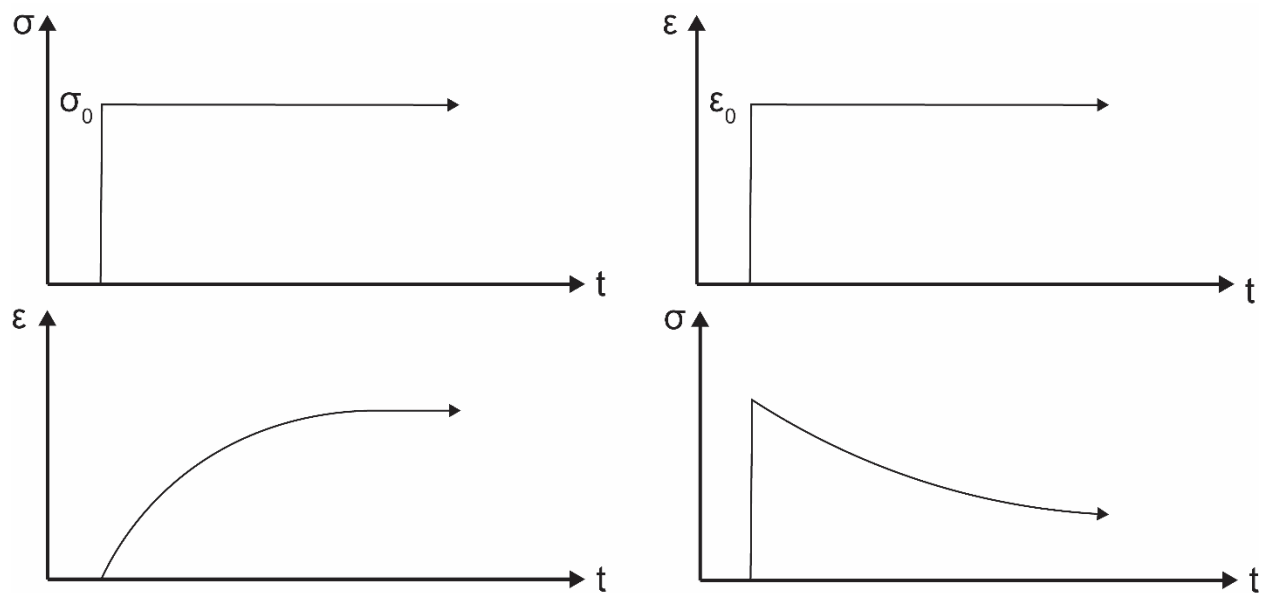


Figure 1. 8 Left: Creep response following step loading Right: Stress relaxation response following step deformation

Poroelasticity, similar to viscoelasticity, describes a material that exhibits both elastic and time-dependent mechanical behavior. However, in contrast to viscoelasticity, this energy-dissipating behavior is not driven by rearrangement of the network, and instead by the fluid movement through the network under mechanical loading. As a poroelastic material is loaded, the volume of the interstitial spaces in the network are reduced, which pressurizes the interstitial fluid. The newly formed pressure gradients create a flow from the volume under contact towards the boundaries of the material. If loaded slowly enough, the fluid moves freely

through the polymer network, and the mechanical behavior of the material is representative of its elastic properties. If loaded quickly, the fluid flow out from under contact is restricted and results in interstitial fluid pressurization, which slowly dissipates over time until the material reaches an equilibrium state. Poroelastic behavior allows both hydrogels and hydrated tissues (i.e., articular cartilage) to effectively stiffen as the rate of the applied load is increased (Fig 1.9). In the case of articular cartilage, this poroelastic stiffening allows the ECM, which possesses an elastic stiffness of less than 1 MPa, to support contact stresses as high as 5 MPa found in normal activity^{113,114}.

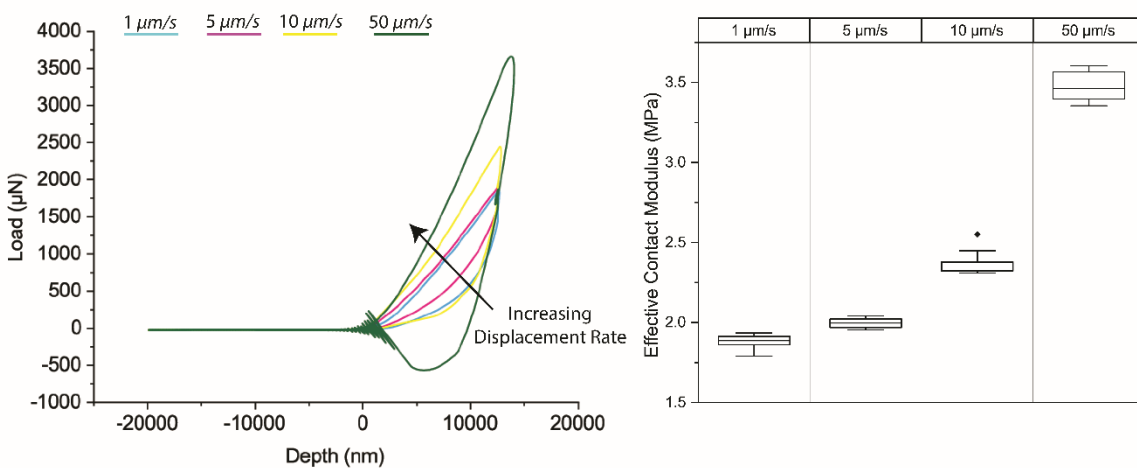


Figure 1. 9 Apparent stiffening of 10 wt. % agarose with increasing indentation rate.

Poroelastic stiffening also reduces the load carried by the network. In articular cartilage, this fluid load support has been claimed to shield the matrix from high normal stresses and strains as a mechanism to maintain the integrity of the collagen network under abrupt loading^{26,27}. However, it should be noted that the aforementioned shielding effect does not shield other non-mechanical components residing within the matrix, including chondrocytes residing within the ECM¹¹⁵. This shared mechanical behavior of hydrogels and hydrated tissues

has spawned an entire field of research known as tissue-engineering, which seeks to regenerate, repair, and/or grow new tissue using hydrogels designed to match the mechanical performance of native tissue.

1.2.4 Composite Hydrogels and Functionally Graded Interfaces

Composite materials are frequently utilized in applications where a single material does not possess all of the desired properties. This is no different in the case of hydrogels. With advances in hydrogel chemistry and manufacturing techniques like 3D printing, scientists are able to combine two or more hydrogels with different mechanical, optical, electrical, and chemical properties to fit the demands of many biomedical applications. As an example, double network hydrogels, consisting of a stiff brittle hydrogel network and a second, soft and ductile hydrogel network have fracture strengths several times greater than that of either individual network¹¹⁶.

While composite hydrogels remain a promising solution to a host of challenging biomedical applications, they are not without drawbacks. It is well-understood that interfaces between materials with divergent mechanical properties create stress-concentrations. Stress-concentrations increase the likelihood of fracture under mechanical loading. For example, Evans *et al.* demonstrated an increase in strain energy release rate (i.e., reduction in fracture toughness) with increasing modulus mismatch for a fiber pull-out test¹¹⁷. In composite hydrogels, the likelihood of interfacial failure is further increased through differential swelling. Most hydrogels are manufactured in the absence of water and swollen after post-processing to make the final material. Stiff hydrogels tend to swell to a lesser extent than softer hydrogels. Thus, when a stiff and soft hydrogel are bonded at an interface in an unswollen state, a residual

stress is created at the interface by swelling following post-processing. As an example, Zawko *et al.* demonstrated that the differential swelling between two halves of hyaluronic acid hydrogels with different degrees of crosslinking. It was found that the likelihood of failure at the interface between the two halves increased when the differential swelling was maximized¹¹⁸. The stress caused by differential swelling in combination with the existing stress-concentration makes the interface between hydrogels a likely point of failure.

Functionally graded interfaces have been demonstrated to improve the fracture toughness between materials with mismatched mechanical properties^{119,120}. Graded interfaces create a more gradual spatial change in mechanical properties than that of a sharp bi-material interface by continually transitioning from one material to another (Fig. 1.10). Recently, researchers demonstrated a stereolithography-based approach for programmable integration of two hydrogels with divergent material properties. Near the interface, the conversion of the stiff hydrogel was reduced to permit infiltration of the second, soft hydrogel. Using this approach, researchers achieved a 33% increase in failure strain¹²¹. While promising, there is crucial need for parametric studies which evaluate the improvement of fracture toughness as a function of controllable parameters including the shape of the gradient function (i.e., step vs. continuous gradient) and relative interfacial widths.

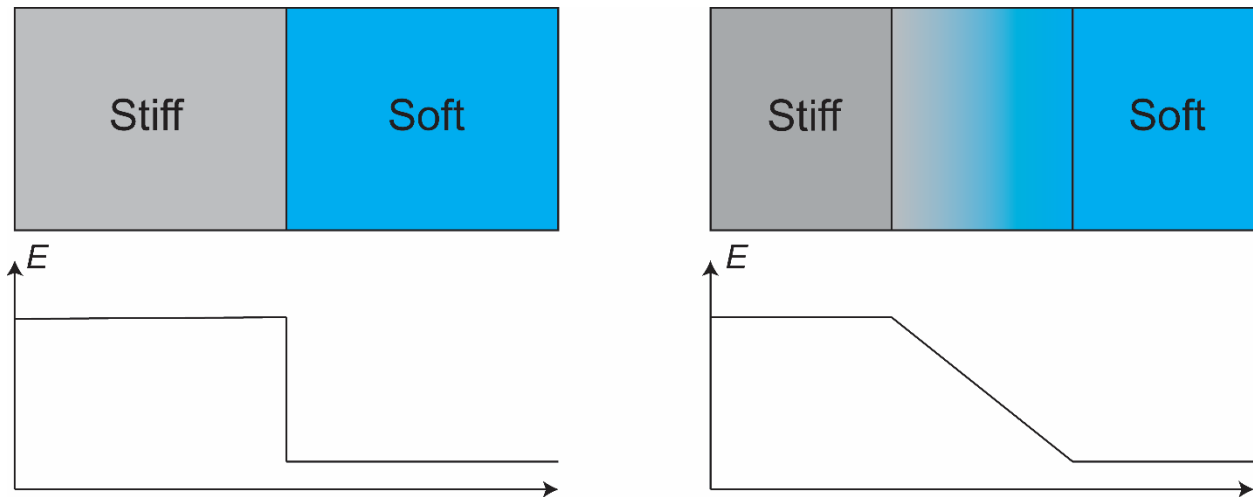


Figure 1. 10 Schematic depicting the abrupt change in material properties at a bi-material interface (left) and a more gradual change in material properties with the inclusion of functionally graded interface (right).

1.3.0 Indentation

1.3.1 History and Overview

Indentation-based characterization of materials has its origins in Moh's hardness scale. Moh's hardness scale was first introduced in 1822 as a practical way of qualitatively assessing the hardness of geological samples. In application, a geological sample is scratched with a set of standard materials ranging from talc to diamond. If the material standard left a scratch on the unknown sample, the sample was softer than the standard. If no scratch was visible, the geological sample was harder than the material standard. While simplistic, the process of using a known material to determine the properties of an unknown material represents an early foray into the field of contact mechanics to determine properties of a material.

The second major contribution to the field of contact mechanics came from Heinrich Hertz in the 1880. While studying Newton's optical interference fringes in the gap between two glass lenses (Fig 1.11), Hertz became concerned of the influence of elastic deformation of the surfaces of the lenses as a result of pressure used to bring them in to contact¹²². From these

experiments, Hertz developed equations to describe the contact between two elastic spheres of varying radii, R_1 and R_2 .

$$a = \left(\frac{3PR}{4E^*} \right)^{\frac{1}{3}}$$

Where a is the radius of contact, P is the applied load, R is the relative radius of the two elastic spheres in contact, defined as:

$$\frac{1}{R} = \frac{1}{R_1} + \frac{1}{R_2}$$

and E^* is the reduced modulus, defined as:

$$\frac{1}{E^*} = \frac{1 - \nu_1^2}{E_1} + \frac{1 - \nu_2^2}{E_2}$$

And the subscripts 1 and 2 represent the two spheres in contact. Work from Hertz represented the transition of contact mechanics from the qualitative to the quantitative realm.

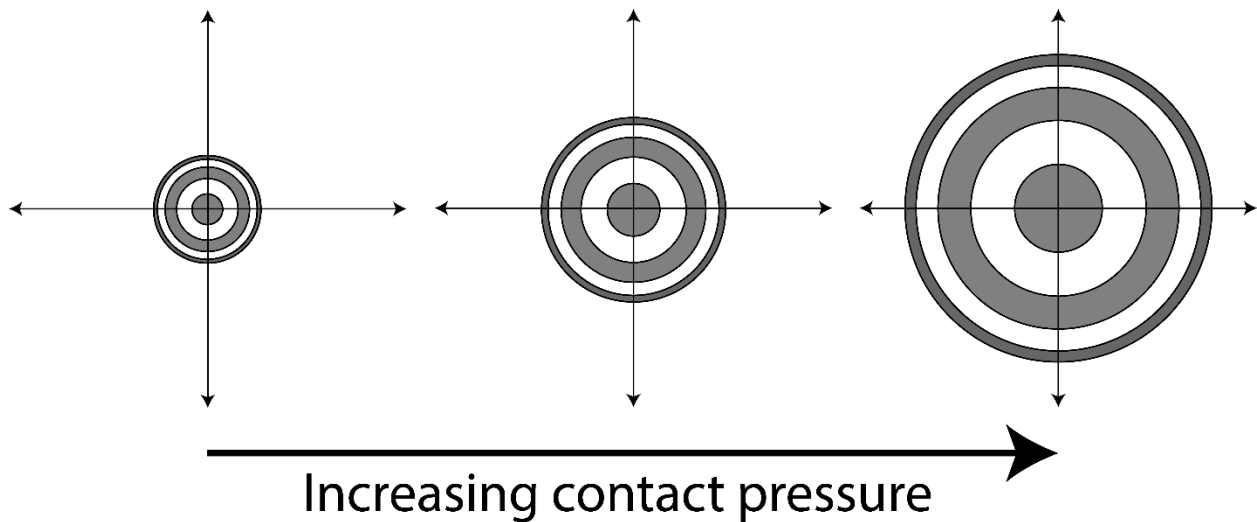


Figure 1. 11 Illustration of increasing size of interference fringes with increasing applied load (i.e., contact pressure)

The third major contribution came from Boussinesq in 1885. Boussinesq derived the solution to the problem of an axis-symmetric rigid body penetrating an elastic half-space oriented normal to the direction of loading¹²³. Boussinesq's solution allowed the determination of the normal stresses at any point in an elastic medium below a concentrated load applied at the surface:

$$\sigma_z = \frac{3P}{2\pi} * \frac{z^3}{R^5}$$

Boussinesq's work represented the first approach to the problem of determining the distribution of stress under contact.

The next major contribution came from Sneddon. Sneddon derived relations between load, displacement, and contact for a rigid conical indenter and a linearly elastic half space¹²⁴:

$$P = \frac{2E \tan(\alpha)}{\pi(1 - \nu^2)} h^2$$

Where P is the applied load, E is Young's modulus, ν is Poisson's ratio, α is the half angle of the cone, and h is the displacement of the indenter. A similar solution was determined for a cylindrical punch¹²⁴:

$$P = \frac{2ER}{(1 - \nu^2)} h$$

Where R is the radius of the cylindrical punch. Sneddon later demonstrated that a general relationship of the form:

$$P = \alpha h^m$$

Could be used to describe the load-displacement relationship for any punch of simple, axis-symmetric geometry¹²⁵. Where α and m are constants. The exponent m is related to the shape of indenter with $m=1$ for a cylindrical punch, $m=1.5$ for spherical probes, and $m=2$ for conical probes. Sneddon's work would later be used extensively in the development of depth-sensing indentation analysis techniques^{126,127}.

Up until this point, contact mechanics was studied solely at the macroscale and properties were typically derived using dead-weight loading and direct measurements of the residual impressions left by the indentation experiment. Tabor was the first to use load and displacement¹²⁸ sensing indentation methods and was joined later on by Stillwell. From the experiments carried about by Stillwell and Tabor revealed a key finding, that the shape of the residual impression from both spherical and conical indentation probes were spherical and conical, respectively, but with a slightly larger radius than that of the indenter probe¹²⁹. From this finding existing solutions for spherical contact in a spherical hole and conical contact in a conical hole could be used to account for the ways in which plasticity affects the interpretation of elastic unloading (Fig 1.12). Additionally, the shape of the total unloading curve and the depth recovered could be used to accurately determine the modulus and the size of contact impression. Thus, paving the path for depth-sensing indentation.

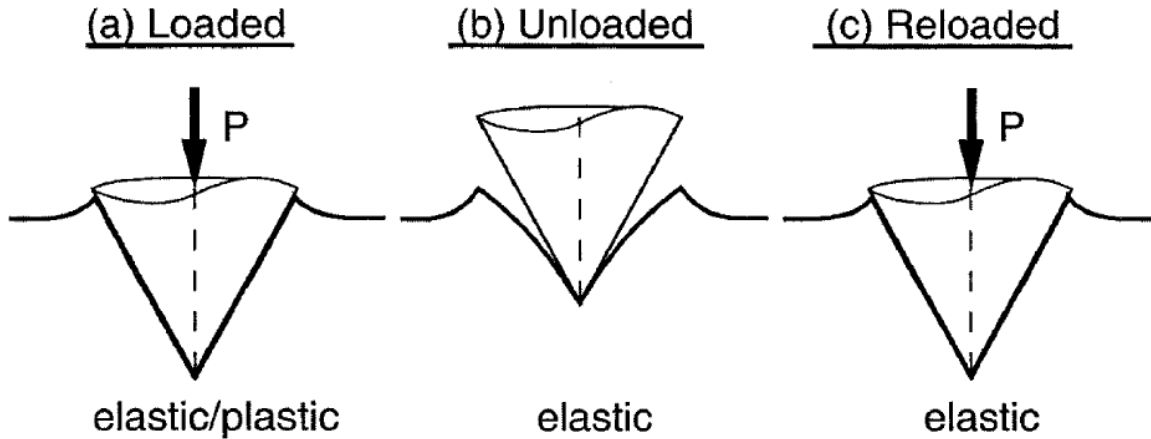


Figure 1. 12 Schematic representation of deformation processes during loading and unloading of a conical indenter. Reprinted by permission from Springer Nature Customer Service Centre GmbH: Springer Nature Journal of Materials Research Understanding nanoindentation unloading curves, G.M. Pharr and A. Bolshakov, Springer Nature (2002).

Depth-sensing indentation was first put into practical use in the 1970s. Buylchev, Alekhin, Shorshorov and other collaborators modified microhardness testing machines to obtain load versus displacement data^{130–134}. From the load versus displacement data, the researchers isolated the initial portion of the unloading curve and measured an unloading stiffness, S , defined as:

$$S = dP/dh$$

The unloading stiffness, in conjunction with the optically measured residual impression, were then used to calculate a reduced modulus from the equation:

$$S = \frac{dP}{dh} = \frac{2}{\sqrt{\pi}} E^* \sqrt{A}$$

Where, E^* , is the reduced modulus (defined previously) and A is the measured area of the residual impression. Furthermore, Buylchev demonstrated that the solution was equally valid

for spherical and conical indenters and predicted that the solution would hold up to the use of pyramidal indenters as well.

With depth-sensing indentation validated on the macroscale, attention was turned to the development of submicron depth-sensing indentation methods for determining the properties of thin films and surface layers. In contrast to macroscale experiments, microscale indentations leave residual impressions which are not easily measured directly. This limitation was addressed by Pethica, Hutchings and Oliver, who proposed a method of using the knowledge of the indenter geometry to develop a relationship between indenter displacement and the projected cross-sectional area in contact¹³⁵. The relationship took the form of:

$$A = F(h)$$

And was based on the idea that the material conforms to the shape of the probe to some unspecified depth. Thus, knowing the shape of the indenter, and a characteristic depth, the projected area could be determined. From the load versus displacement curves, both the maximum displacement and final displacement could be readily determined. Oliver ultimately found that the final displacement, h_f , gave a better estimate of the projected area when the calculated area was compared to measurements of the residual impression from transmission electron microscopy (TEM)¹³⁶.

Dorner and Nix applied the knowledge of Bulychev and company along with the findings of Oliver, Pharr, and Pethica and developed a simple empirical method for determining contact area¹³⁷. The initial portion of the unloading curve was extrapolated back to zero load and the extrapolated depth at zero load was used with the indenter shape function (the relationship

between contact area and displacement) to determine a contact area which proved to be more accurate than estimations based on peak load or final depth (Fig. 1.13). The contact area could then be used in solutions developed by Bulychev *et al.* to allow the determination of elastic modulus and hardness on the microscale.

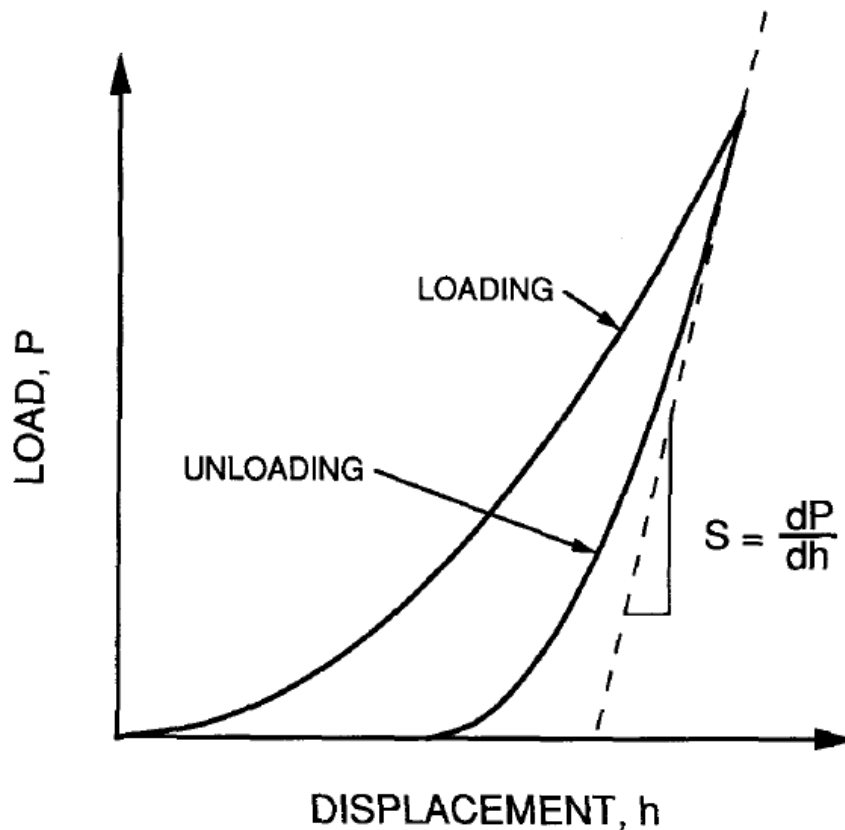


Figure 1. 13 Schematic depicting extrapolation of the initial portion of the unloading curve. Reprinted by permission from Springer Nature Customer Service Centre GmbH: Springer Nature Journal of Materials Research On the generality of the relationship among contact stiffness, contact area, and elastic modulus during indentation, G.M. Pharr, W.C. Oliver, and F.R. Brotzen, Springer Nature (1992).

Notably, there was one invalid assumption of the Dorner-Nix approach, in that the initial portion of the unloading curve was assumed to be linear. Experimentally, unloading curves are rarely, if ever, linear and are better described by power laws, similar to the solution derived by Sneddon, with exponents ranging from 1.2 to 1.6. To combat this challenge, Oliver and Pharr

introduced a technique which accounted for the curvature in the unloading curve and provided a more accurate prediction of the contact area at peak load¹²⁶. First, they introduced an updated definition of the total displacement, which stated that the total displacement at any point during the indentation could be described as a sum of two depths: the depth over which the material conformed to the shape of the indenter, h_c , and the displacement of the surface at the perimeter of contact, h_s (Fig. 1.14).

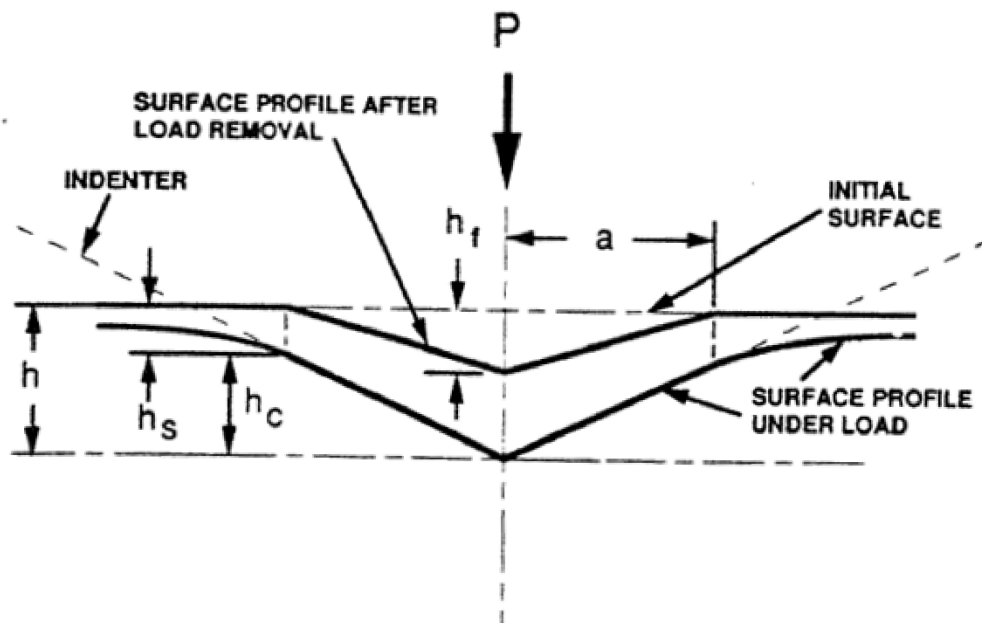


Figure 1. 14 Schematic representation of a cross-section of an indent with relevant quantities labeled. Reprinted by permission from Springer Nature Customer Service Centre GmbH: Springer Nature Journal of Materials Research An improved technique for determining hardness and elastic modulus using load and displacement sensing indentation experiments, W.C. Oliver, G.M. Pharr, Springer Nature (1992).

Thus, the contact depth, h_c , could be calculated from the load versus displacement curve as:

$$h_c = h_{max} - h_s$$

Then, from Sneddon's force-displacement relation, h_s was determined as:

$$h_s = \epsilon \frac{P_{max}}{S}$$

Where ϵ was a geometric constant based on the shape of the indenter (0.72 for a cone, 1 for a flat punch).

Next, they rewrote solutions from Bulychev *et al.* as:

$$E^* = \frac{\sqrt{\pi}}{2} \frac{S}{\sqrt{A}}$$

To evaluate stiffness, the unloading curve was first fit to the power law relationship:

$$P = A(h - h_f)^m$$

Where the A , h_f , and m were all determined from the fitting procedure. The exponent m is based on the indenter geometry ($m = 2$ for a conical probe, and 1 for a flat punch). The above equation was then differentiated at peak load and displacement to find the stiffness, solving the problem in Doerner and Nix's method. Once stiffness was determined, contact depth could be calculated, from which the projected area was determined, and the reduced modulus could be evaluated.

This technique was updated in 2004 to describe several refinements and caution against certain pitfalls¹²⁷. For the refinements, the concept of an effective indenter shape was introduced (Fig. 1.15), where the "effective indenter shape" is defined as the shape "which produces the same normal surface displacements on a flat surface that would be produced by the conical indenter on the unloaded, deformed surface of the hardness impression". The

effective indenter shape can be used to mathematically determine the (previously estimated) geometric constant, ϵ , using:

$$\epsilon = m \left[1 - \frac{2\Gamma\left(\frac{m}{2(m-1)}\right)}{\sqrt{\pi}\Gamma\left(\frac{1}{2(m-1)}\right)} (m-1) \right]$$

Where m is determined from the power law curve fit of the unloading curve and Γ is the Gamma function. The other refinement to the determination of the reduced modulus was the introduction of the correction factor, β , which in part describes the deviation of the indenter cross-sectional area from a circle. Thus, the updated equation for determining the reduced modulus became:

$$E^* = \left(\frac{1}{\beta}\right) \frac{\sqrt{\pi}}{2} \frac{S}{\sqrt{A}}$$

Other refinements to calibration procedures were described by Oliver and Pharr but will not be discussed here.

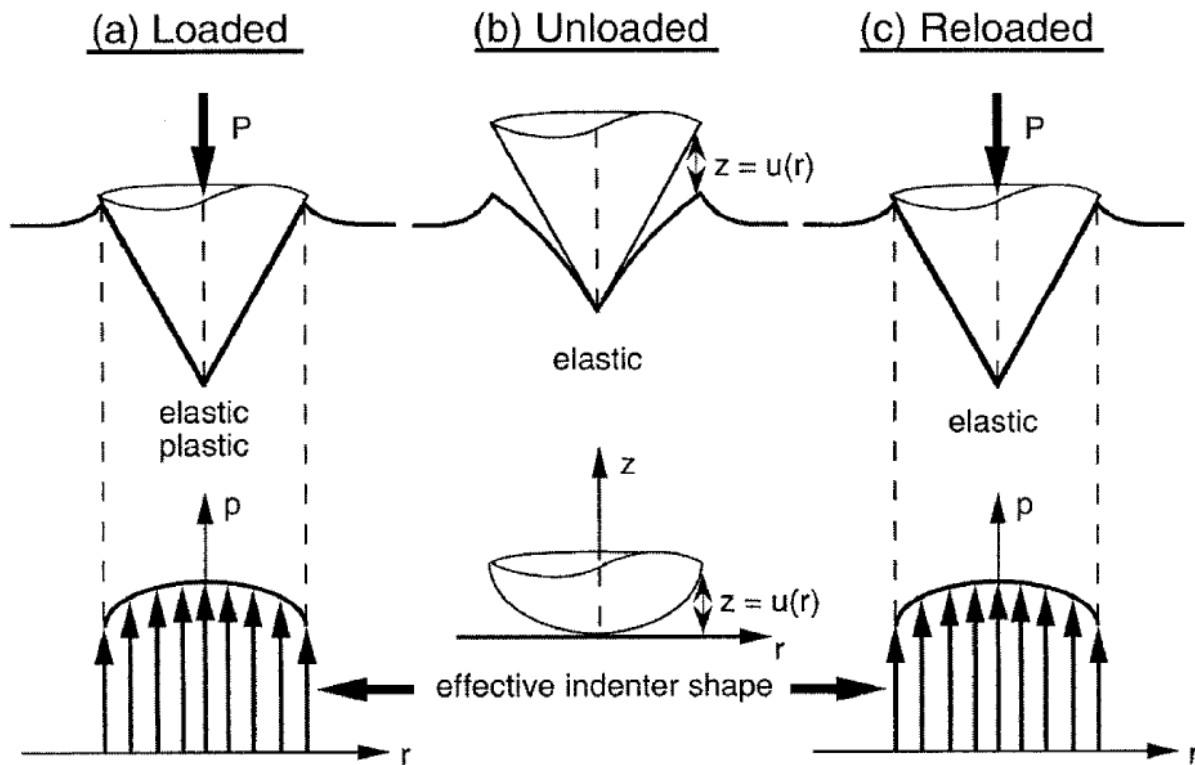


Figure 1. 15 Schematic depicting the effective indenter shape. Reprinted by permission from Springer Nature Customer Service Centre GmbH: Springer Nature Journal of Materials Research Understanding nanoindentation unloading curves, G.M. Pharr and A. Bolshakov, Springer Nature (2002).

Lastly, Oliver and Pharr described a potential pitfall affecting the accuracy of contact area calculations, referred to as “pile-up”. When pile-up exists around the area of contact, the actual contact area is greater than the calculated area, leading to overestimation of the determined reduced modulus and hardness. Pile-up occurs for materials which have a yield strength much smaller than that of the reduced modulus. From experimentation, it was found that the existence of pile-up could be predicted from the ratio of h_f/h_{max} , where pile-up occurs when $h_f/h_{max} \geq 0.7$. For $h_f/h_{max} \geq 0.7$, Oliver and Pharr recommended optical measurement of the contact area. The Oliver-Pharr approach with the described refinements is considered the gold standard for the assessment of stiff, linear-elastic-plastic materials.

While the Oliver-Pharr method of analysis uses the unloading curve to extract material properties, it is also possible to use the loading curve through the use of Hertz Elastic Contact Theory. While originally developed for two spherical bodies in contact, Hertz equations of elastic contact are easily expanded to the problem of a rigid probe in contact with an elastic half space by setting R_2 , the radius of the material to be tested, to infinity (Fig. 1.16), the load-displacement relationship can be determined:

$$P = \frac{4}{3} E^* R^{1/2} \delta^{3/2}$$

Though inappropriate for testing materials with plastic deformation, Hertz analysis is an easy method for determining material properties with spherical indentation probes and is frequently applied to glassy polymers.

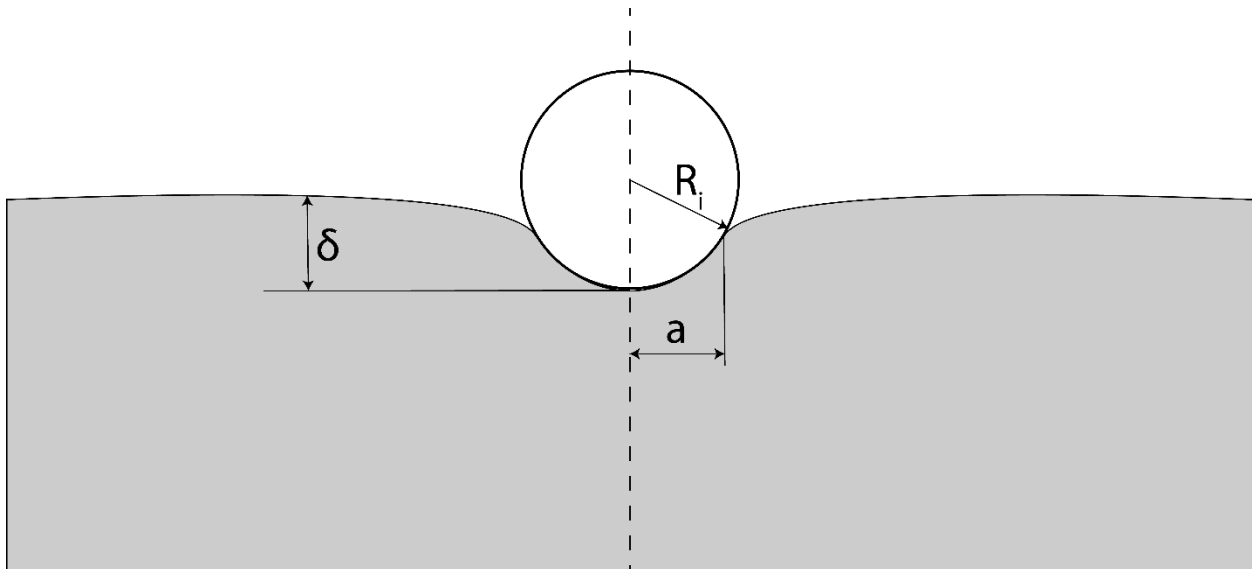


Figure 1. 16 Schematic depicting the cross-section of a spherical indentation with relevant quantities used in Hertz Elastic Contact Theory labeled.

1.3.2 Microindentation of Soft, Hydrated Materials

While Hertzian and Oliver-Pharr analyses are considered the gold standards for a wide-range of traditional materials, these analyses are only valid for linear-elastic and linear-elastic-plastic materials (i.e., materials that do not exhibit time-dependent mechanical behavior). However, nearly all soft, hydrated materials, including most hydrogels and biological tissues, are viscoelastic and/or poroelastic¹⁰⁸. Thus, alternative analyses were needed to describe these time dependent behaviors.

Viscoelastic behavior can be assessed using two types of indentation tests: creep and load-relaxation. In a standard indentation creep test, a probe of known geometry (typically spherical with a known radius, R_i) is displaced into the surface of a material until a specified peak load, P_0 is reached. This load is then held, and the displacement required to maintain the peak load as the material relaxes under contact is measured as a function of time, $h(t)$. To determine material properties, an approach described by Oyen *et al.* is utilized¹³⁸. This approach begins with the governing equation for spherical indentation in an incompressible ($\nu = 0.5$) elastic medium:

$$h^{\frac{3}{2}} = \frac{3}{8 * R_i^{0.5}} \left[\frac{P}{2G} \right]$$

The term $[P/2G]$ is then replaced by a viscoelastic hereditary integral operator for creep to give:

$$h^{\frac{3}{2}}(t) = \frac{3}{8 * R_i^{0.5}} k \int_0^{t_R} J(t - u) du$$

Where t_R is equal to the ramp time to peak load, k is equal to the ramp loading rate (i.e., $k = dP/dt$), $J(t)$ is the material creep function, and u is the dummy variable of integration for time.

The solution for $J(t)$ depends on the rheological model selected to represent the material being tested. However, in most cases the solution for a standard linear solid model (free spring in series with a Kelvin parallel spring and dashpot), thus $J(t)$ becomes:

$$J(t) = C_0 - \sum_{i=1}^j C_i \exp\left(-\frac{t}{\tau_i}\right)$$

and equation (2) becomes:

$$h^{\frac{3}{2}}(t) = \frac{3}{8 * R_i^{0.5}} k \left\{ C_0 t_R - \sum C_i \tau_i \exp\left(-\frac{t}{\tau_i}\right) \left[\exp\left(\frac{t_R}{\tau_i}\right) - 1 \right] \right\}$$

By fitting equation () to the $h(t)$ data collected during the hold portion of the test, the constants C_0 & C_i , and the time constants τ_i , can be determined. The instantaneous shear modulus, G_0 , and the equilibrium shear modulus, G_∞ , can be calculated using the constants as follows:

$$G_0 = \frac{1}{2(C_0 - \sum C_i)}$$

$$G_\infty = \frac{1}{2C_0}$$

A load-relaxation microindentation test is similar to a creep test, except in this case, a peak displacement is held and the decrease in load is monitored over time as the material relaxes under contact to give $P(t)$ ¹³⁹. Using a similar approach to that of creep analysis, $P(t)$ can be represented as:

$$P(t) = \frac{8 * R_i^{0.5}}{3} \int_0^i G(t-u) \left[\frac{d}{du} h^{\frac{3}{2}}(u) \right] du$$

Unlike the solution for creep behavior, the integral used here has no closed-form analytical solution and must instead be solved numerically. From numerical integration of the above using $h(t) = kt_R = h_{max}$, and a material relaxation function of the form:

$$G(t) = C_0 + \sum_{i=1}^j C_i \exp\left(-\frac{t}{\tau_i}\right)$$

the load-relaxation solution takes the form of:

$$P(t) = B_0 + \sum_{i=1}^j B_i \exp\left(-\frac{t}{\tau_i}\right)$$

The constants B_0 & B_i can then be related to the material parameters, C_0 & C_i using the experimental parameters h_{max} , t_R , and R_i via:

$$C_0 = \frac{B_0}{h_{max}^{\frac{3}{2}} \left(\frac{8 * R_i^{\frac{1}{2}}}{3} \right)}$$

and

$$C_i = \frac{B_i}{(RCF_i) h_{max}^{\frac{3}{2}} \left(\frac{8 * R_i^{\frac{1}{2}}}{3} \right)}$$

Where RCF_k is the ramp correction factor defined as:

$$RCF_i = \left(\frac{\tau_i}{t_R} \right) \left[\exp\left(\frac{t_R}{\tau_i} \right) - 1 \right]$$

The instantaneous shear modulus, G_0 , and the equilibrium shear modulus, G_∞ , can be calculated using the constants as follows:

$$G_0 = \frac{\sum C_i}{2}$$

$$G_\infty = \frac{C_0}{2}$$

From either of the above tests and corresponding analyses, three important characteristics of the material are determined: i.e., the instantaneous response to an applied load (G_0), the equilibrium behavior (G_∞), and the characteristic relaxation times of the material (τ_i).

Poroelastic behavior, as discussed in a previous section, is time-dependent behavior that results from interstitial fluid pressurization and fluid flow through a porous network as a material is deformed. To assess this poroelastic behavior using indentation, a method of analysis called “Hertz Biphasic Theory” or HBT can be used²³. The HBT approach allows the determination of an effective contact modulus, E_c , equilibrium contact modulus, E_{c0} , tensile modulus, E_t and permeability, k . Equilibrium contact modulus, tensile modulus, and permeability are all material properties, whereas the effective contact modulus is an experimental-parameter-dependent measure of the effective stiffness resulting from both fluid and solid contributions.

HBT was developed by Moore & Burris to improve upon linear biphasic theory approach adapted for indentation by Mak¹⁴⁰, and later improved upon by Mow¹⁴¹. The linear biphasic approach allows the determination of an aggregate modulus, Poisson’s ratio, and permeability from a single indentation creep test using a plane ended indentation probe (i.e, a flat punch).

While relatively straightforward, the linear biphasic approach has several limitations, as pointed out by Moore & Burris. First, the use of a plane-ended indentation probe creates stress concentrations at the periphery of contact which can cause damage to the material's surface. Second, these stress concentrations increase with decreasing probe size, effectively limiting the spatial resolution when mapping variations across a material's surface. Third, the linear biphasic model cannot reproduce the stresses observed for joint loading *in-vivo* of 1-5 MPa. Lastly, use of the linear biphasic approach requires access to a custom curve-fitting program developed by the authors. In contrast, the HBT approach uses spherical indentation probes, which eliminate stress concentrations at the periphery of contact, and is capable of reproducing pressures consistent with physiological loading²³.

To use the HBT approach, indentation tests must be performed to allow the computation of the effective contact modulus for multiple displacement rates, $\dot{\delta}$, and an equilibrium modulus. Effective contact modulus is computed by fitting the loading portion of the load, P , versus displacement, δ , curve to the Hertz equation:

$$P = \frac{4}{3} E_c R_i^{\frac{1}{2}} (\delta - \delta_{off})^{\frac{3}{2}}$$

where R_i is the radius of the spherical indentation probe, and δ_{off} is the effective displacement offset for contact of the "true" surface of the material. The inclusion of the offset term adjusts the point of contact for a rough surface to that of an ideally flat and smooth surface. The equilibrium contact modulus is also computed with the Hertz equation, using the equilibrium load and an equilibrium displacement determined from either an indentation creep tests or

stress relaxation test. Once the effective contact modulus and equilibrium modulus are known for each displacement rate tested, the fluid load fraction, F' , can be determined using:

$$F' = \frac{E_c - E_{c0}}{E_c}$$

The fluid load fraction describes the fraction of the applied load supported by the pressurization of the interstitial fluid upon loading. The fluid load fraction data for each displacement rate tested, in conjunction with the equilibrium contact modulus, indentation probe radius, and are then fit to the following equation to determine the tensile modulus and permeability:

$$F' = \left(\frac{E_t}{E_t + E_{c0}} \right) \left(\frac{\dot{\delta}R_i}{\dot{\delta}R_i + E_{c0}k} \right)$$

The first term, $E_t/(E_t + E_{c0})$ represents the maximum achievable fluid load fraction and increases with the lateral stiffness of a material. Cartilage, as an example, has exhibited fluid load fractions as high as 0.85 in indentation experiments²², owing to the high lateral stiffness that results from a tightly woven collagen matrix and the attachment to the underlying subchondral bone. The second term $\dot{\delta}R_i/(\dot{\delta}R_i + E_{c0}k)$ represents where the fluid load fraction falls on the scale between 0 and the asymptote governed by the first term. This second term comes from the Peclet number for indentation, which is defined as:

$$Pe = \frac{\dot{\delta}R_i}{E_{c0}k}$$

The Peclet number describes the ratio of the rate of deformation of the material relative to the characteristic velocity of interstitial fluid flow in the material. When $Pe \ll 1$, the rate of

deformation is slow relative to movement of fluid. As such, little to no fluid pressurization occurs and fluid load fraction approaches 0. When $Pe = 1$, the rate of deformation is equal to the characteristic velocity of fluid movement and so the fluid load fraction approaches 50% of the asymptote value. When $Pe > 1$, the rate of deformation is greater than the characteristic fluid velocity. Thus, the interstitial fluid movement is restricted, and the fluid supports a greater fraction of the load. Lastly, when $Pe \gg 1$, fluid movement is significantly restricted, and the maximum possible fluid load support is achieved (Fig. 1.17).

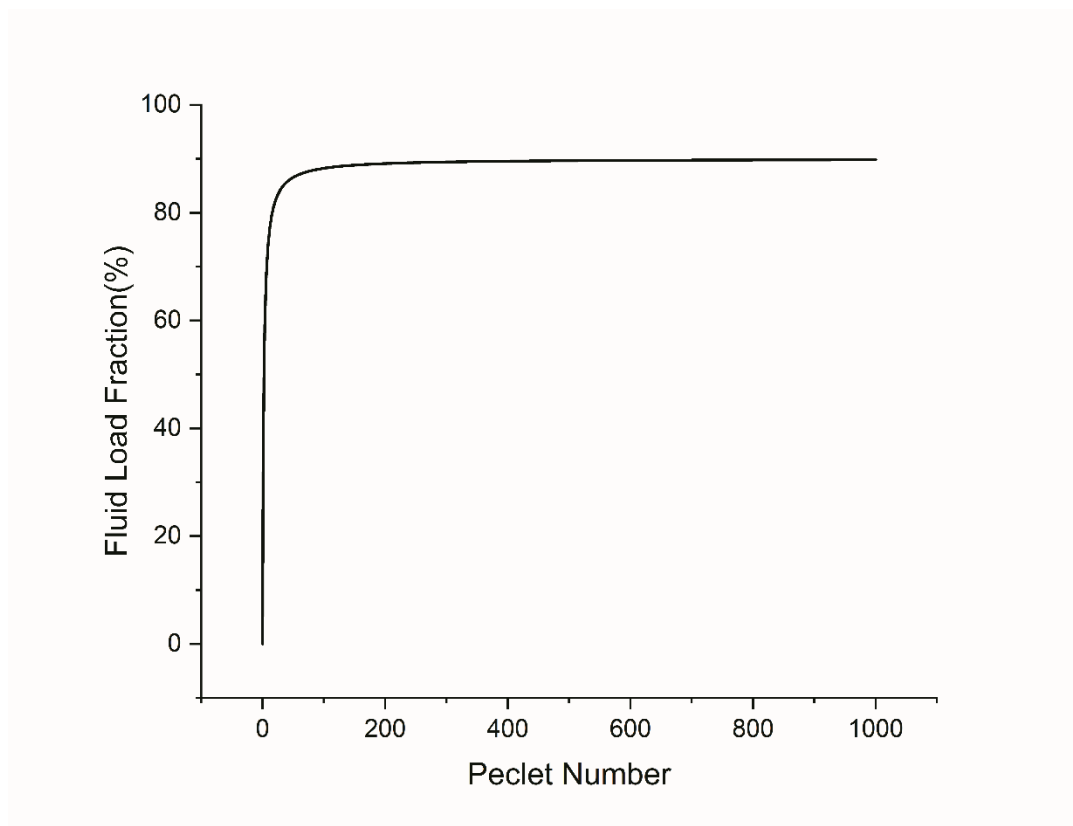


Figure 1. 17 Evolution of fluid load support with increasing Peclet number

These viscoelastic and poroelastic analyses allow researchers to understand the time-dependent behavior of a material, predict the performance under various loading conditions, and select materials for specific applications. As an example, Chaudhuri *et al.* demonstrated

that cell spreading was increased for materials that exhibited greater stress relaxation than materials of the same modulus that exhibited only elastic behavior^{142,143}. In the case of soft, hydrated tissues such as articular cartilage, poroelastic analyses can assess both the change in mechanical behavior with the onset of disease (e.g., Osteoarthritis) and provide design criteria to replicate using hydrogel tissue engineering scaffolds. It should be noted, however, that these microindentation analyses are only as valuable as they are accurate.

1.3.3 Key Assumptions and Challenges

The analyses described above, including linear-elastic, viscoelastic, and biphasic/poroelastic analyses, assume that the material being characterized is homogenous, the sample volume approximates an infinite half-space, and that the relationship between indenter displacement and contact area is well-defined. If the material characteristics violate any of these assumptions, errors are introduced into the calculations of material properties. Heterogeneity is overcome easily enough through additional indentation experiments that evaluate properties as a function of location and depth. Finite volumes of material that violate the assumption of an infinite half-space can be assessed using analyses that correct for the limited thickness¹⁴⁴ of the sample, which is readily measurable. In direct contrast, the contact area is not directly measurable and instead, is based on the geometry of the probe and the displacement into the material. Thus, material characteristics which affect this relationship cannot be accounted for by comparing the actual area in contact with the contact area in an ideal material. As such, the following will focus on material characteristics which alter the relationship between indenter displacement and contact area.

1.3.4 Adhesion

Adhesion between the probe and material is frequently encountered when testing soft, hydrated materials. Adhesion results in larger contact areas as a function of indenter displacement than the relationship used in traditional indentation analyses predicts. Larger contact areas require greater force to displace the probe into the material leading to an increased apparent stiffness and overestimated moduli. Despite this, adhesion is often ignored during the evaluation of compliant materials, likely as a result of load-controlled indentations that do not capture the adhesion behavior that occurs as the probe lifts off of the surface of the material following a displacement-controlled indent¹⁴⁵. Thankfully, there exist a few strategies to deal with adhesion in indentation.

One strategy to account for adhesion in compliant materials is to change the testing environment. Ebenstein demonstrated that indenting PDMS in air (i.e., unsubmerged) or while submerged in water resulted in significant pull-off forces (i.e., negative values for load as the probe lifts off of a material's surface) and overestimations of the indentation modulus by 60% and 30%, respectively¹⁴⁵. However, when the PDMS was submerged in a detergent solution, the pull-off forces disappeared, and the indentation modulus was accurately determined (Fig 1.18). The other approach, described by Ebenstein and Wahl¹⁴⁶, and later validated for use with hydrogels by Ebenstein and Kohn¹⁴⁷, uses the Johnson-Kendall-Roberts adhesion model¹⁴⁸ to correct for adhesion behavior. In short, this approach uses a curve-fit of the unloading curve from a displacement-controlled indent to determine the maximum adhesion force and the contact radius when the load, $P = 0$. The maximum adhesion force is used to determine the work of adhesion, which is then used in conjunction with the contact radius at zero load to

determine an accurate reduced modulus for the material using the JKR model. The reader is directed to the above-mentioned studies for further details on the approach and analysis, as adhesion is not the focus of this work.

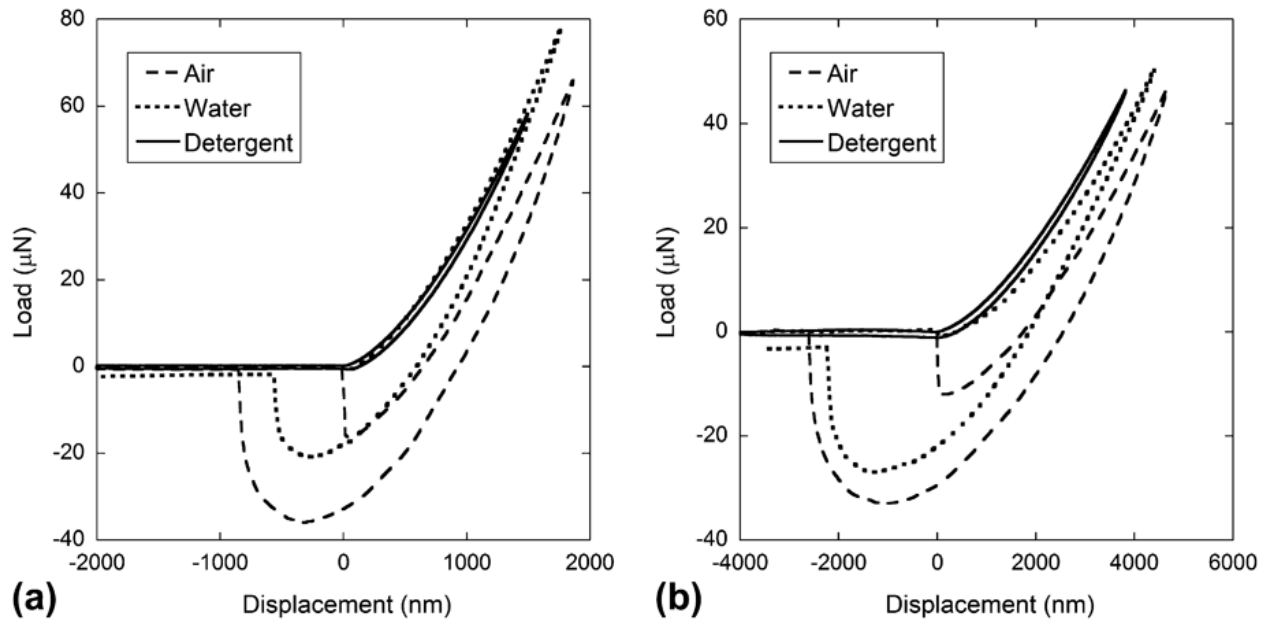


Figure 1. 18 Sample force curves in air, water, and detergent for (a) 10:1 PDMS sample with a 130- μm radius tip and (b) 20:1 PDMS sample with a 94- μm radius tip. Reprinted by permission from Springer Nature Customer Service Centre GmbH: Springer Nature Journal of Materials Research Nano-JKR force curve method overcomes challenges of surface detection and adhesion for nanoindentation of a compliant polymer in air and water, Donna M. Ebenstein, Springer Nature (2011).

1.3.5 Surface Roughness

Surface roughness is the deviation of a material's surface topography from that of an ideally flat smooth plane. In reality, all material surfaces are rough, and even the smoothest surfaces viewed with the naked eye appear rough when observed on the nanoscale. Rough surfaces are often created via manufacturing processes, wear, or, in the case of mechanical testing applications, sample preparation. Rough surfaces are typically described in terms of asperities on the material surface. These asperities form peaks and valleys, the peaks are

obviously the tops of the asperities, whereas the valleys are created by the space between asperities (Fig 1.19).

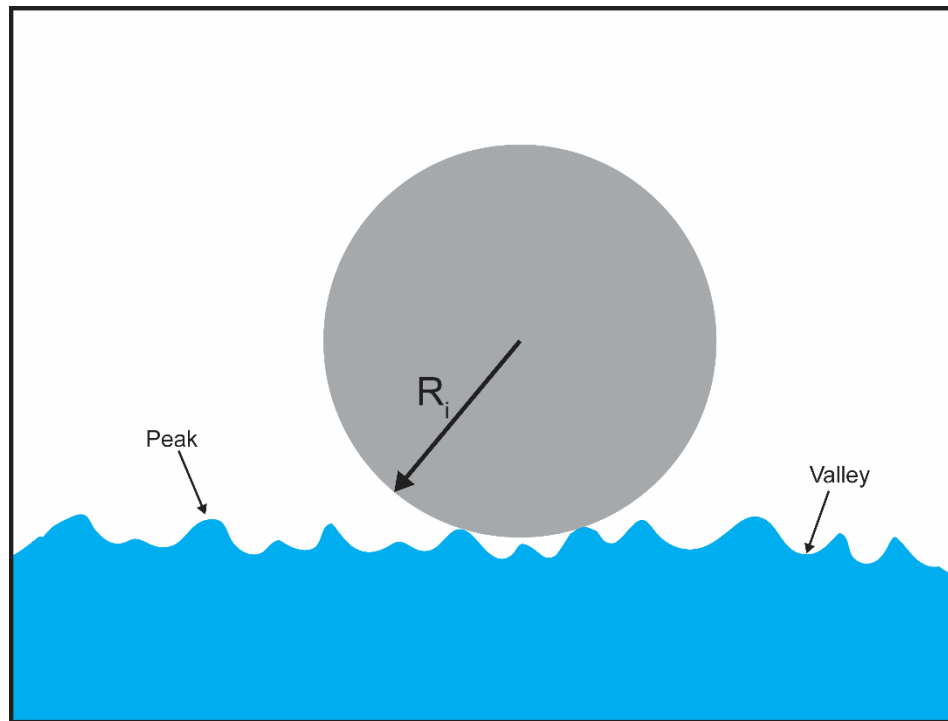


Figure 1. 19 Schematic depicting contact between a spherical probe and a rough surface.

It can almost certainly be claimed that Holm was the first to make progress to describe the influence of surface roughness on contact mechanics while studying electrical contact resistance between two surfaces¹⁴⁹. Holm introduced the idea that, although the average stress resulting from two surfaces in contact was in the elastic regime, the local stresses at the points of contact were much higher and would likely lead to plastic flow. Archard pointed that while it was reasonable to assume plastic flow (i.e., flattening of contact asperities) during initial contact between rough surfaces, plastic flow could only occur once¹⁵⁰. Thus, a steady state must be reached in which the contact between two surfaces was purely elastic. Archard demonstrated that although Hertz elastic contact theory does not predict proportionality

between load, P , and contact area, A , a model of multiscale roughness (i.e., asperities on top of asperities) predicted increased proportionality as smaller and smaller scales were considered. He explained that if the number of contacts remained constant during increased loading, Hertz elastic contact theory predicted the change in contact area with increasing load ($A \propto P^{2/3}$). In contrast, if the number of contacts increases with additional loading, as would be the case for microscale contact, $A \propto P$. Thus, establishing the basis for the influence of surface roughness on microindentation.

This seminal work led to future investigations into the influence of surface roughness on microindentation property assessments on a wide variety of different materials. Greenwood, Johnson, and Matsubara investigated the influence of surface roughness on Hertz elastic contact theory using a steel ball and roughened steel plate¹⁵¹. Their investigation revealed that the ideal contact area assumed by the Hertz equation could be corrected using a non-dimensional parameter:

$$\alpha = \frac{\sigma R}{a_0^2}$$

where σ is the combined roughness of the two surfaces, R is the radius of the steel ball, and a_0 is the ideal contact area assumed by the Hertz equation. This correction theoretically allows an accurate computation of an indentation modulus, provided the roughness of the indentation probe and sample are known. Rather than focus on a correction to contact area, Xia *et al.* focused on a correction for the contact depth used in Oliver-Pharr analysis by adding an offset value which corresponds to an effective point of contact¹⁵². The offset is determined by shifting the displacement from individual load versus displacement curves so a resulting set of curves

fall on top one another, at which point, a single set of material properties can be determined. Additionally, the researchers found that the standard deviation of the shift was linearly related to the surface roughness when measured using a scan size similar to the dimensions of contact.

Other investigations into the influence of surface roughness focused less on a mathematical correction, and more on the change in measured properties as a function of controllable indentation parameters like probe size and indentation depth. In 2004, Wai *et al.* investigated the influence of surface roughness on microindentation property assessments of glassy polymers by testing polystyrene samples, roughened to three different finishes, using two different probe radii and three different peak loads¹⁵³. They demonstrated that the indentation depth required to obtain bulk properties was partly related to the largest peak-to-valley height evaluated from AFM-based surface roughness measurements over an area of similar size to that of the maximum contact radius achieved during indentation. In 2005, Chung and Yap investigated the influence of surface roughness on microindentation property measurement of polymeric dental composites of varying roughness using a Vickers indentation probe¹⁵⁴. They found that the measured properties were independent of surface finish provided that the peak indentation depth was 30 times larger than the average roughness, R_a . In contrast, Donnelly *et al.* demonstrated just a year later that the maximum indentation depth did not affect the mean value for the measured indentation modulus of bone using a Berkovich probe¹⁵⁵. Instead, indentation depth affected the variability, and that same variability was eliminated by indenting to depths greater than 3 times the RMS roughness. Qasmi and Delobelle, also in 2006, performed a detailed investigation into the influence of surface roughness on microindentation using various metals and ceramics, and showed that surface

roughness only affected the measured Young's modulus at shallow depths, whereas indentation depths greater than 10 times the RMS roughness did not affect the mean value¹⁵⁶. In 2008, Miller *et al.* showed experimentally that indentation depths greater than 5 times eliminate the influence of surface roughness provided that the RMS surface roughness is measured using a scan size with an edge length of 200 times the maximum indentation depth¹⁵⁷. Chen and Diebels carried out a numerical investigation was performed using FEA to simulate contact between spherical indentation probes and a rough polymer surface¹⁵⁸. From these simulations, they concluded that surface roughness should not influence microindentation property measurements provided that the indentation depth was at least 3 times greater than the asperity heights on the rough surface, similar to that which was found by Donnelly *et al.*

It would be an impossible task to gather a single conclusion or strategy for eliminating the influence of surface roughness using the work identified above. However, a few things are clear. First, the roughness, and corresponding relationships between roughness and indentation depth depend on the scan size. Both Wai *et al.* and Xia noted a more predictive correlation between indentation depth and roughness when the scan size was approximately equal to the dimensions of contact. Second, the required peak indentation depth also appears to depend on probe geometry. Wai *et al.* demonstrated a peak indentation depth equal to the largest peak to valley was required to eliminate the influence of surface roughness on microindentation with spherical probes, while Chung and Yap found that a peak depth of 30 times the average roughness was required when using a Vickers probe. Lastly, and perhaps most importantly, the influence of surface roughness appears to depend on the material being

tested. Polymers demonstrate both a decreasing indentation modulus and scatter with indentation depth (e.g., Wai *et al.* and Chung and Yap), whereas only the scatter is affected for stiffer materials (e.g., Donnelly *et al.* and Miller *et al.*). This realization that the influence of surface roughness appears to be material-dependent motivates investigations into all classes of material, including that of soft, hydrated materials like agarose and articular cartilage.

1.4.0 Fracture of Graded Hydrogel Interfaces

1.4.1 Overview of Linear-Elastic Fracture Mechanics, Strain Energy Release Rate

Flaws are present in every material and at different scales. Flaws can take the form of internal cracks, surface cracks, and even imperfect bonding at the interface between materials. These imperfections create stress concentrations in materials under applied loads, effectively amplifying the stress, which may result in failure at significantly lower loads than predicted by the strength required to separate two planes of atoms. Silica glass, as an example, has a theoretical fracture strength of 7 GPa, but fractures at stresses between only 30 and 100 MPa in physical experiments¹⁵⁹. Engineering fracture mechanics is used to study the propagation of flaws in materials and predict the conditions under which a material with a flaw of known dimensions will fail.

The quantitative framework for characterizing the fracture toughness of materials comes from linear elastic fracture mechanics (LEFM) and is based on ideal elasticity. There are two parallel approaches for calculating fracture toughness in LEFM. One is a stress-intensity-factor-based approach where a global stress intensity, K , is used to define the local stresses and displacements near a crack tip. The other energy-based approach where a global strain energy

release rate, G , is used to define the net change in potential energy with the extension of the crack (Fig. 1.20). While the two approaches are related to one another, as demonstrated by Irwin¹⁶⁰, the energy-based approach is preferred in the polymer community and will therefore be the focus of the following sections.

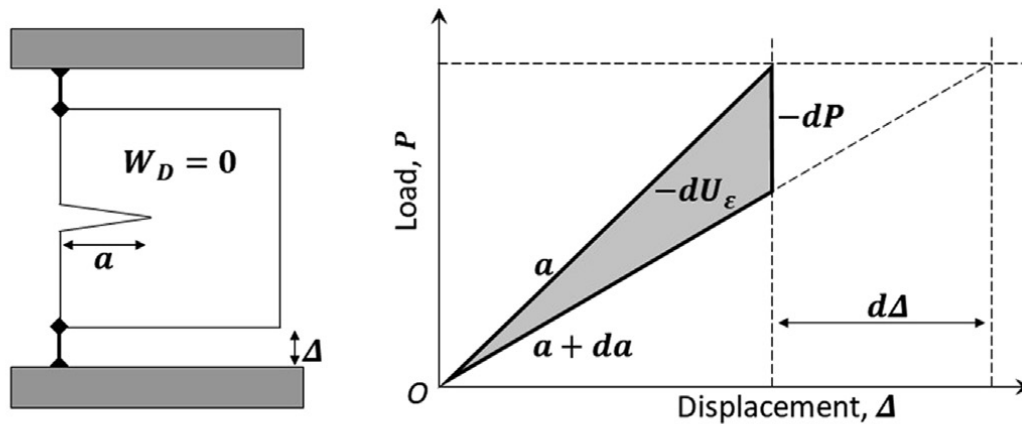


Figure 1. 20 Schematic depicting the change in potential energy with crack propagation. Reprinted from *Introduction to Fracture Mechanics*, 1st Edition, Rob. O. Ritchie and Dong Liu, *Linear Elastic Fracture Mechanics*, 11-48, Elsevier Books (2021), with permission from Elsevier.

The energy-based approach, developed by Irwin¹⁶⁰, is based on a strain energy release rate, G , where the critical strain-energy release rate, G_c , is defined as the value of G associated with the onset of fracture. defined as the change in potential energy, U_{PE} , per unit increase of crack area, A :

$$G = \frac{dU_{PE}}{dA}$$

Where the potential energy, U_{PE} , is defined as the difference between the stored strain energy, U_{ϵ} , and the work done by the externally applied load, W_D :

$$U_{PE} = U_{\epsilon} - W_D$$

To compute G , we consider a specimen with an edge crack of length, a , under a fixed displacement, Δ , such that $W_D = 0$. Thus, the potential energy becomes:

$$U_{PE} = U_\varepsilon = \int_0^P \Delta dP = \frac{\Delta P}{2}$$

From the above, G can be calculated using:

$$G = -\left(\frac{1}{B}\right)\left(\frac{dU_{PE}}{dA}\right)_\Delta = -\left(\frac{\Delta}{2B}\right)\left(\frac{dP}{dA}\right)_\Delta$$

1.4.2 Work of Fracture

It is important to note that the definitions and formulae described above only apply when the conditions of LEFM are met. The most important of these conditions is the assumption of small-scale yielding, which specifies that any plasticity that occurs near the crack tip is at least an order of magnitude smaller than the in-plane dimensions of the crack. Polymeric materials often violate this assumption as a result of crazing, where crack-tip advancement is preceded by the formation of fibrils that bridge the crack tip opening and carry a significant fraction of the applied load¹⁶¹. While there are alternative analyses, such as that of the J-integral, that can be used to determine a geometry-specific fracture toughness, it is occasionally preferable to use a relative measurement of fracture toughness. Relative toughness measures are particularly useful during component design in which fracture toughness is a parameter to be maximized as a function of material formulation and/or part geometry. In such cases, an analogous measure of fracture toughness can be determined from the area under a load versus displacement curve in an approach referred to as the work of fracture.

The approach is utilized by integrating the load-displacement to determine the “work of fracture”, U_f :

$$U_f = \int_0^{v_{Lf}} P dv_L$$

Where v_L is the load-line displacement, defined as the vertical displacement of the specimen from its original position as a result of loading, and v_{Lf} is the load-line displacement at complete fracture. From the previous section, remember that the energy release rate is the change in potential energy per unit change of crack area and that at complete fracture, the total potential energy has been converted to the work of fracture. Thus, an average strain energy release rate, G_c can be determined by dividing the work of fracture by the total initial unfractured area ahead of the crack, A_f .

$$G_c = \frac{U_f}{A_f}$$

From the above formulae, it is readily apparent that viscoelasticity is a major source of error surrounding the work of fracture approach. Viscoelastic materials, by definition, dissipate energy over time. Thus, the work of fracture is strongly dependent on the rate of extension/loading utilized during testing, preventing this approach from defining a single parameter capable of describing a material’s fracture toughness. This issue is readily resolved in comparative analyses, as the goal is to maximize fracture toughness in the presence of other constraints, such as a prescribed geometry or rate of loading.

1.4.3 Fracture Modes

A material with a pre-existing flaw (i.e., crack) can fracture in several different ways depending on the “mode” of the externally applied loading. Mode I fracture occurs when a tensile load is applied to the crack, causing the crack to open orthogonal to the existing crack surface. This opening of the crack puts the crack tip under tension and causes it to propagate once stresses reach their critical level. Mode II fracture occurs under in-plane shear loading, where the shear stress acts parallel to the existing crack surface. Under mode II loading, the crack surfaces slide parallel to one another, creating shear stresses orthogonal to the crack surface ahead of the crack tip. Mode III fracture also occurs under shear loading, but the shear loading is anti-plane causing the crack surfaces to slide past one another orthogonal to the direction of crack propagation in a tearing fashion (Fig. 1.21).

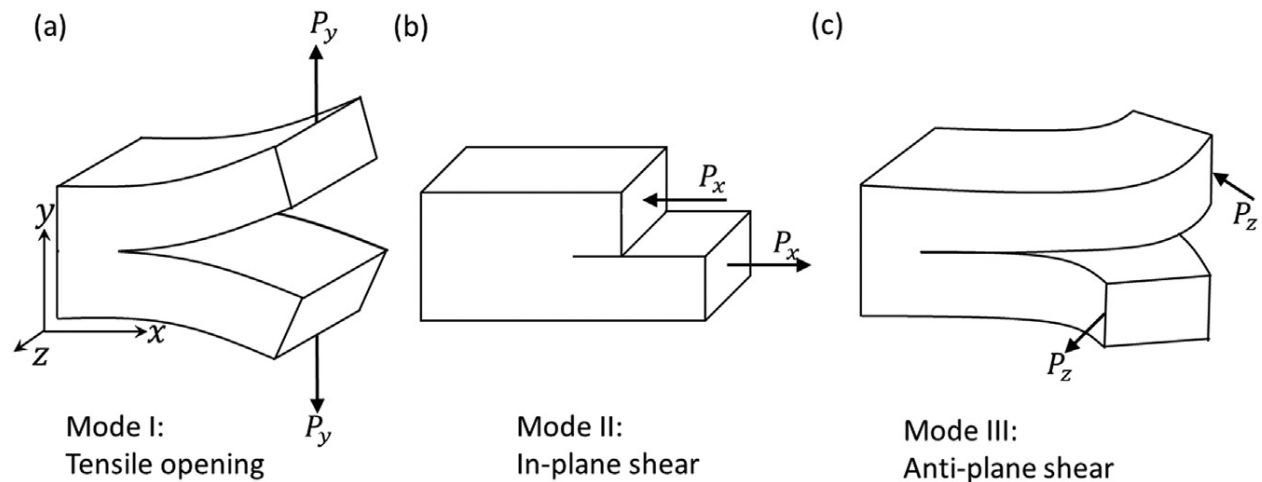


Figure 1. 21 Fracture Modes. Reprinted from *Introduction to Fracture Mechanics, 1st Edition*, Rob. O. Ritchie and Dong Liu, *Linear Elastic Fracture Mechanics*, 11-48, Elsevier Books (2021), with permission from Elsevier.

1.4.4 Fracture of Soft Materials

Soft materials are typically thought of as materials with a small Young’s modulus, $E =$ single kPa to a few MPa . In the context of fracture mechanics, a slightly different definition is

used, and soft materials are defined by an elasto-adhesive length¹⁶², defined as the ratio of the effective surface energy, Γ , and the elastic modulus, E :

$$l_{EA} = \Gamma/E$$

At length scales comparable or smaller than the elasto-adhesive length, a material can be considered to be “soft”. l_{EA} ranges from 4 nm to 40 μm for soft materials and increases significantly when mechanical dissipation occurs¹⁶² (e.g., viscoelasticity), as dissipation is accompanied by large effective surface energies, Γ_{eff} .

The elasto-adhesive length is effectively the elastic blunting size near the crack tip. Thus, when the thickness of the soft layer, h , decreases below the elasto-adhesive length, LEFM breaks down and it is no longer possible to define a critical stress intensity factor¹⁶². In contrast, Griffith’s solution for the strain energy release rate remains valid, so long as the bulk deformation is elastic or the region of dissipation is smaller than l_{EA} , h , and the crack length, a . However, if the region of dissipation is larger than l_{EA} , h , or a (as is often the case), LEFM breaks down and can no longer be used to characterize the intrinsic properties of the soft material. Instead, the energy required to propagate a crack is directly related to the structure. In other words, changes in the geometry of the fracture specimen result in changes to the apparent fracture energy.

To determine an intrinsic strain energy release rate, G , for these materials, the energy required to develop and maintain a dissipation zone at the crack tip, G_D , needs to be accurately predicted. The strain energy release rate can then be expressed as:

$$G = G_0 - G_D$$

Where G_0 is the total energy available to drive the crack tip supplied by external loading. While this would initially appear straightforward, accurate prediction of G_D would require computational models that incorporate both the bulk viscoelastic response under loading and a cohesive zone model capable of describing the complicated failure mechanisms at the crack tip (Fig. 1.22). Both are challenging to obtain and incorporate, and as a result, a quantitative prediction of the intrinsic strain energy release rate of soft, energy dissipating materials remains elusive.

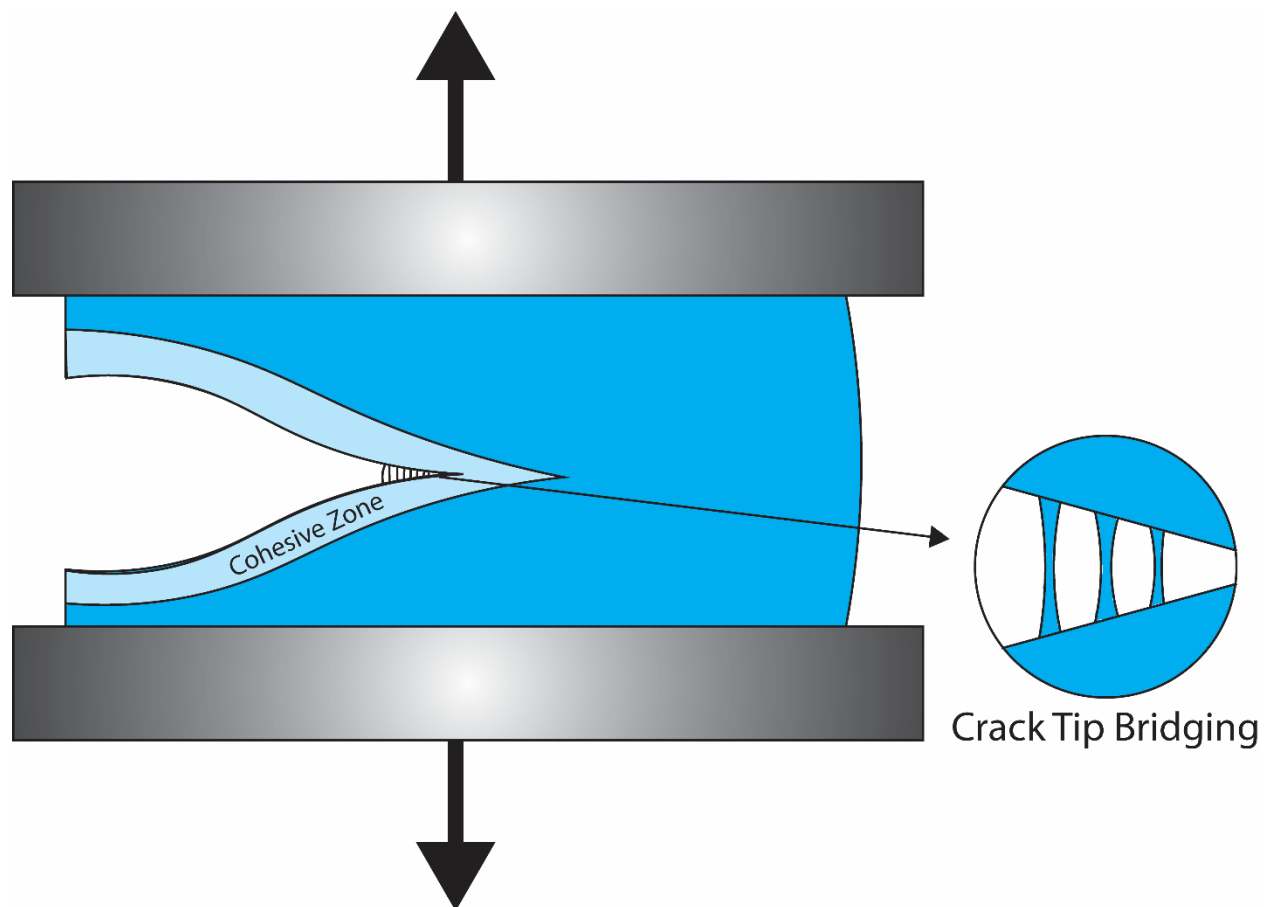


Figure 1. 22 Illustration of Mode I fracture of a soft, energy-dissipating material.

While computational models have proven difficult to obtain, progress towards characterizing G in through the use of phenomenological models has been encouraging. In

2015, Zhang *et al.* demonstrated the ability to accurately predict the critical parameters for crack propagation through phenomenological modeling of the damage mechanism in a tough hydrogel¹⁶¹. Using a different approach, Mayumi *et al.*¹⁶³ demonstrated a method to subtract the dissipated energy during loading to permit the use of Greensmith's relation¹⁶⁴. However, the work has not been validated as generally applicable to soft, viscoelastic materials. For now, it appears that the fracture mechanics of soft viscoelastic materials is limited to comparative analyses between specimens with identical geometries.

1.4.5 Fracture toughness of functionally graded interfaces

It is well understood that the interface between materials of divergent mechanical properties creates stress-concentrations under loading and is therefore more susceptible to failure than the bulk of either constituent. To reduce the stress concentrations at the interface, the mismatch in material properties must be reduced. One way of accomplishing this task would be to replace one of the materials with a material with properties similar to that of the other. Unfortunately, this is rarely a feasible solution, as at least one of the materials in such composite applications is likely selected for its chemical or electrical properties instead of its mechanical properties (e.g., chemically resistant coating on a structural material)¹⁶⁵. Another, more practical, solution is to increase the distance over which the mechanical property change occurs via the use of a graded interface, where the volume fractions of the two constituents or the mechanical properties differ continuously across an interfacial zone.

Previous investigations into the fracture mechanics of functionally graded materials (FGMs) and functionally graded interfaces (FGIs) have primarily focused on numerical analyses. These studies serve as the foundation for understanding how functionally graded interfaces can

be used to enhance the fracture toughness in dissimilar material interfaces. Erdogan and various coworkers have published extensively in this area of research and from his theoretical works, the following can be concluded about functionally graded materials: 1) Interfacial regions have a higher concentrations of stress and micrometer length scale flaws¹⁶⁶, 2) Fracture toughness tends to be lower in the interfacial zone between dissimilar materials than in adjacent homogenous materials¹⁶⁶, 3) Increasing the thickness of an FGM coating on a homogenous substrate decreases the resistance to interfacial crack propagation¹⁶⁷, and 4) The dominant mode of failure for an interfacial crack between a homogenous substrate and FGM coating is mode I¹⁶⁷. Shbeeb and Binienda expanded upon Erdogan's work by adding a second homogenous layer on the other side of the FGM, effectively creating a functionally graded interface in between two homogenous materials¹⁶⁸. This work demonstrated that the strain energy release rate for an interface crack between the substrate and FGM decreases with increasing FGM thickness. While Shbeeb and Binieda's study suggests that a functionally graded interface between dissimilar materials may increase the fracture toughness of a component compared to that of a bi-material interface, and that the improvement in toughness increases with FGM thickness, this study does not address the problem of a crack initiating in the graded interface. Marur and Tippur addressed this gap by investigating the strain energy release rate, mode mixity, and stress intensity factors for functionally graded interfaces of varying widths and cracks initiating in different locations¹⁶⁹. They demonstrated that the strain energy release rates decrease for functionally graded interfaces of increasing width with the exception of a crack that starts at the interface between the functionally graded interface and the softer homogenous material. With the recent rise of composite applications in hydrogels, researchers

can look to the existing literature for ideas on how to design more robust interfaces between different gels. However, it remains to be seen how the previous work, which primarily deals with functionally graded metals and ceramics, applies to composite hydrogels with mechanical properties that differ by several orders of magnitude.

Polymer-based investigations may be the first step towards addressing this gap in the literature. Additive manufacturing permits multi-material printing of polymers with divergent material properties similar to the differences found in composite hydrogel applications but, unlike the use of hydrogels, offer a key advantage in that hydration does not need to be maintained during testing. Recently, Mirzaali et al. investigated how different material property gradients affect the measured fracture toughness for a crack initiating in the soft phase of a stiff-soft-stiff composite produced via additive manufacturing¹⁷⁰. It was found that continuous gradients offer an enhanced fracture toughness as compared to multi-step gradients for materials that differed by three orders of magnitude. Additional work using similar polymer-based material systems, with focus on design parameters like interfacial width, will ultimately help to close this gap in the literature.

1.5.0 Motivation and Specific Aims

1.5.1 Motivation

Tissue engineering is a growing discipline that uses a combination of engineering disciplines to develop novel materials and therapeutic strategies for the repair or replacement of damaged tissues and organs. Current strategies typically focus on the development of tissue engineering scaffolds using hydrogels. Scaffolds are application specific and may require

interfacing multiple hydrogel materials to mimic the properties of the native tissue. In addition, the resulting design must be mechanically robust so as to withstand physiological loading without failure. Thus, the success of a given application is dependent on 1) the ability to accurately characterize the properties of the native tissue and scaffold materials and 2) the ability to integrate multiple hydrogel materials in a robust manner.

1.5.2 Specific Aims

The first objective of this work is to improve the ability to accurately characterize the mechanical properties and behavior of soft, hydrated tissues and hydrogel materials used in biomimetic, tissue engineering scaffolds. This objective will be accomplished via aims one and two, each with its own separate study. The second objective of this work is to improve the ability to integrate multiple hydrogel materials in a robust manner, which will be accomplished via aim three.

The first aim of this work is to evaluate the influence of surface roughness on small-scale indentation property assessments of hydrogel materials. Small-scale indentation testing is commonly used in the mechanical characterization of hydrogels as this mode of testing is non-destructive and readily performed in physiologically relevant environments (i.e. submerged in a bathing solution). Surface roughness is known to influence the properties measured via indentation. Yet, the influence of surface roughness on small-scale indentation of hydrogels has, to this point, been ignored. To address this gap, a microscale depth-sensing indentation study was performed on agarose gels with surfaces of varying roughness.

Related Work:

Uzcategui, A.C., Higgins, C.I., Hergert, J.E., **Tomaschke, A.A.**, Crespo-Cuevas, V., Ferguson, V.L., Bryant, S.J., McLeod, R.R. and Killgore, J.P., 2021. Microscale Photopatterning of Through-Thickness Modulus in a Monolithic and Functionally Graded 3D-Printed Part. *Small Science*, 1(3), p.2000017.

The second aim of this work is to experimentally determine the influence of surface roughness on small-scale indentation property assessments of soft tissues via AFM and depth-sensing indentation testing. The bulk mechanical behavior of a soft, hydrated tissue is driven by the microscale mechanical properties and the variation of those properties throughout the tissue. Furthermore, it is well understood that cells interact with the extra cellular matrix (ECM) on the microscale. Thus, small-scale indentation property assessments are frequently utilized to characterize the mechanical behavior of soft, hydrated tissues and determine the desired properties to replicate using tissue engineering scaffolds. However, soft tissues possess an inherent roughness, and excision of tissue for testing creates additional roughness as the ECM of the tissue is disrupted. Despite this, the influence of surface roughness on indentation testing of soft tissues remains uninvestigated. To address this gap, AFM and depth-sensing microindentation was performed on articular cartilage surfaces prepared using two-different cutting techniques, producing surfaces with distinctly different levels of surface roughness.

Related Work:

Aisenbrey, E.A., **Tomaschke, A.A.**, Schoonraad, S.A., Fischenich, K.M., Wahlquist, J.A., Randolph, M.A., Ferguson, V.L. and Bryant, S.J., 2019. Assessment and prevention of cartilage degeneration surrounding a focal chondral defect in the porcine model. *Biochemical and biophysical research communications*, 514(3), pp.940-945.

Schoonraad, S.A., Fischenich, K.M., Eckstein, K.N., Crespo-Cuevas, V., Savard, L.M., Muralidharan, A., **Tomaschke, A.A.**, Uzcategui, A.C., Randolph, M.A., McLeod, R.R. and Ferguson, V.L., 2021. Biomimetic and mechanically supportive 3D printed scaffolds for cartilage

and osteochondral tissue engineering using photopolymers and digital light processing. *Biofabrication*, 13(4), p.044106.

The third aim of this work is to evaluate the relative fracture toughness of a graded interface between two hydrogel materials with divergent mechanical properties. Complex tissue engineering applications, such as that of mechanically robust osteochondral scaffold for the repair of articular cartilage, demand properties that cannot be met using a single hydrogel material. Composite hydrogel materials provide a solution to this problem. While promising, it is well understood that a sharp interface between materials with divergent properties results in stress concentrations at the interface. Graded interfaces have been used in other material systems to extend the area over which the property change occurs, reducing stress concentrations near the interface. However, the use of graded interfaces in hydrogel composites has not been investigated. This may in part be due to the complexities of performing fracture tests on hydrogels (e.g., fabrication of test specimens, maintaining hydration during testing, slipping at the grips). To begin to address this gap, single edge notch fracture testing was performed on graded interfaces of varying width between two 3D printed polymers with divergent mechanical properties.

Related Work:

Aisenbrey, E.A., **Tomaschke, A.**, Kleinjan, E., Muralidharan, A., Pascual-Garrido, C., McLeod, R.R., Ferguson, V.L. and Bryant, S.J., 2018. A Stereolithography-Based 3D Printed Hybrid Scaffold for In Situ Cartilage Defect Repair. *Macromolecular bioscience*, 18(2), p.1700267.

1.6.0 References:

- (1) Buckwalter, J. A.; Mankin, H. J. Articular Cartilage: Part I. *Journal of Bone and Joint Surgery, American volume* **1997**, 79 (4), 600.
- (2) Hagg, R.; Hedbom, E.; Möllers, U.; Aszódi, A.; Fässler, R.; Bruckner, P. Absence of the A1(IX) Chain Leads to a Functional Knock-out of the Entire Collagen IX Protein in Mice *. *Journal of Biological Chemistry* **1997**, 272 (33), 20650–20654.
- (3) Xu, J.; Wang, W.; Ludeman, M.; Cheng, K.; Hayami, T.; Lotz, J. C.; Kapila, S. Chondrogenic Differentiation of Human Mesenchymal Stem Cells in Three-Dimensional Alginate Gels. *Tissue Engineering Part A* **2008**, 14 (5), 667–680.
- (4) Zelenski, N. A.; Leddy, H. A.; Sanchez-Adams, J.; Zhang, J.; Bonaldo, P.; Liedtke, W.; Guilak, F. Type VI Collagen Regulates Pericellular Matrix Properties, Chondrocyte Swelling, and Mechanotransduction in Mouse Articular Cartilage. *Arthritis & Rheumatology* **2015**, 67 (5), 1286–1294.
- (5) DR, E. The Collagens of Articular Cartilage. *Sem. Arthritis Rheumatism* **1991**, 21, 211.
- (6) Kwan, A. P.; Cummings, C. E.; Chapman, J. A.; Grant, M. E. Macromolecular Organization of Chicken Type X Collagen in Vitro. *Journal of Cell Biology* **1991**, 114 (3), 597–604.
- (7) Kääh, M. J.; Ito, K.; Clark, J. M.; Nötzli, H. P. Deformation of Articular Cartilage Collagen Structure under Static and Cyclic Loading. *Journal of Orthopaedic Research* **1998**, 16 (6), 743–751.
- (8) Korhonen, R. K.; Laasanen, M. S.; Töyräs, J.; Rieppo, J.; Hirvonen, J.; Helminen, H. J.; Jurvelin, J. S. Comparison of the Equilibrium Response of Articular Cartilage in Unconfined Compression, Confined Compression and Indentation. *J Biomech* **2002**, 35 (7), 903–909.
- (9) Buckwalter, J. A.; Mankin, H. J.; Grodzinsky, A. J. Articular Cartilage and Osteoarthritis. *Instructional Course Lectures-American Academy of Orthopaedic Surgeons* **2005**, 54, 465.
- (10) Sokoloff, L. *Biology of Degenerative Joint Disease*. **1969**.
- (11) Sophia Fox, A. J.; Bedi, A.; Rodeo, S. A. The Basic Science of Articular Cartilage: Structure, Composition, and Function. *Sports Health* **2009**, 1 (6), 461–468.
- (12) Maroudas, A. Distribution and Diffusion of Solutes in Articular Cartilage. *Biophysical Journal* **1970**, 10 (5), 365–379.

- (13) Donnan, F. G.; Harris, A. B. CLXXVII.—The Osmotic Pressure and Conductivity of Aqueous Solutions of Congo-Red, and Reversible Membrane Equilibria. *Journal of the Chemical Society, Transactions* **1911**, *99*, 1554–1577.
- (14) Maroudas, A. Physicochemical Properties of Cartilage in the Light of Ion Exchange Theory. *Biophysical Journal* **1968**, *8* (5), 575–595.
- (15) Torzilli, P. A.; Askari, E.; Jenkins, J. T. Water Content and Solute Diffusion Properties in Articular Cartilage. In *Biomechanics of Diarthrodial Joints*; Ratcliffe, A., Woo, S. L.-Y., Mow, V. C., Eds.; Springer: New York, NY, 1990; pp 363–390.
- (16) Seireg, A.; Arvikar, R. J. The Prediction of Muscular Load Sharing and Joint Forces in the Lower Extremities during Walking. *Journal of Biomechanics* **1975**, *8* (2), 89–102.
- (17) Guilak, F.; Ratcliffe, A.; Lane, N.; Rosenwasser, M. P.; Mow, V. C. Mechanical and Biochemical Changes in the Superficial Zone of Articular Cartilage in Canine Experimental Osteoarthritis. *Journal of Orthopaedic Research* **1994**, *12* (4), 474–484.
- (18) Maroudas, A.; Bannon, C. Measurement of Swelling Pressure in Cartilage and Comparison with the Osmotic Pressure of Constituent Proteoglycans. *Biorheology* **1981**, *18* (3–6), 619–632. <https://doi.org/10.3233/BIR-1981-183-624>.
- (19) Chen, A. C.; Bae, W. C.; Schinagl, R. M.; Sah, R. L. Depth- and Strain-Dependent Mechanical and Electromechanical Properties of Full-Thickness Bovine Articular Cartilage in Confined Compression. *Journal of Biomechanics* **2001**, *34* (1), 1–12.
- (20) Schinagl, R. M.; Gurskis, D.; Chen, A. C.; Sah, R. L. Depth-Dependent Confined Compression Modulus of Full-Thickness Bovine Articular Cartilage. *Journal of Orthopaedic Research* **1997**, *15* (4), 499–506.
- (21) Mow, V. C.; Kuei, S. C.; Lai, W. M.; Armstrong, C. G. Biphasic Creep and Stress Relaxation of Articular Cartilage in Compression: Theory and Experiments. *Journal of Biomechanical Engineering* **1980**, *102* (1), 73–84.
- (22) Bonnevie, E. D.; Baro, V. J.; Wang, L.; Burris, D. L. Fluid Load Support during Localized Indentation of Cartilage with a Spherical Probe. *Journal of Biomechanics* **2012**, *45* (6), 1036–1041.
- (23) Moore, A. C.; Zimmerman, B. K.; Chen, X.; Lu, X. L.; Burris, D. L. Experimental Characterization of Biphasic Materials Using Rate-Controlled Hertzian Indentation. *Tribology International* **2015**, *89*, 2–8.
- (24) McCutchen, C. W. The Frictional Properties of Animal Joints. *Wear* **1962**, *5* (1), 1–17.

- (25) Soltz, M. A.; Ateshian, G. A. Experimental Verification and Theoretical Prediction of Cartilage Interstitial Fluid Pressurization at an Impermeable Contact Interface in Confined Compression. *Journal of Biomechanics* **1998**, *31* (10), 927–934.
- (26) Ateshian, G. A.; Lai, W. M.; Zhu, W. B.; Mow, V. C. An Asymptotic Solution for the Contact of Two Biphasic Cartilage Layers. *Journal of Biomechanics* **1994**, *27* (11), 1347–1360.
- (27) Spilker, R. L.; Suh, J.-K.; Mow, V. C. A Finite Element Analysis of the Indentation Stress-Relaxation Response of Linear Biphasic Articular Cartilage. *Journal of Biomechanical Engineering* **1992**, *114* (2), 191–201.
- (28) Maroudas, A. Physicochemical Properties of Articular Cartilage. *Adult articular cartilage* **1979**.
- (29) Lai, W. M.; Hou, J. S.; Mow, V. C. A Triphasic Theory for the Swelling and Deformation Behaviors of Articular Cartilage. *Journal of Biomechanical Engineering* **1991**, *113* (3), 245–258.
- (30) Lu, X. L.; Sun, D. D. N.; Guo, X. E.; Chen, F. H.; Lai, W. M.; Mow, V. C. Indentation Determined Mechanochemical Properties and Fixed Charge Density of Articular Cartilage. *Annals of Biomedical Engineering* **2004**, *32* (3), 370–379.
- (31) Wahlquist, J. A.; DelRio, F. W.; Randolph, M. A.; Aziz, A. H.; Heveran, C. M.; Bryant, S. J.; Neu, C. P.; Ferguson, V. L. Indentation Mapping Revealed Poroelastic, but Not Viscoelastic, Properties Spanning Native Zonal Articular Cartilage. *Acta Biomaterialia* **2017**, *64*, 41–49.
- (32) Fischenich, K. M.; Wahlquist, J. A.; Wilmoth, R. L.; Cai, L.; Neu, C. P.; Ferguson, V. L. Human Articular Cartilage Is Orthotropic Where Microstructure, Micromechanics, and Chemistry Vary with Depth and Split-Line Orientation. *Osteoarthritis and Cartilage* **2020**, *28* (10), 1362–1372.
- (33) Chen, X.; Zimmerman, B. K.; Lu, X. L. Determine the Equilibrium Mechanical Properties of Articular Cartilage from the Short-Term Indentation Response. *Journal of Biomechanics* **2015**, *48* (1), 176–180.
- (34) Fairbank, T. J. Knee Joint Changes after Meniscectomy. *The Journal of Bone and Joint Surgery. British volume* **1948**, *30-B* (4), 664–670.
- (35) Felson, D. T.; Anderson, J. J.; Naimark, A.; Walker, A. M.; Meenan, R. F. Obesity and Knee Osteoarthritis. *Ann Intern Med* **1988**, *109* (1), 18–24.
- (36) Blazek, K.; Favre, J.; Asay, J.; Erhart-Hledik, J.; Andriacchi, T. Age and Obesity Alter the Relationship between Femoral Articular Cartilage Thickness and Ambulatory Loads in Individuals without Osteoarthritis. *Journal of Orthopaedic Research* **2014**, *32* (3), 394–402.
- (37) Collins, K. H.; Hart, D. A.; Seerattan, R. A.; Reimer, R. A.; Herzog, W. High-Fat/High-Sucrose Diet-Induced Obesity Results in Joint-Specific Development of Osteoarthritis-like Degeneration in a Rat Model. *Bone & Joint Research* **2018**, *7* (4), 274–281.

- (38) Reijman, M.; Pols, H. a. P.; Bergink, A. P.; Hazes, J. M. W.; Belo, J. N.; Lievense, A. M.; Bierma-Zeinstra, S. M. A. Body Mass Index Associated with Onset and Progression of Osteoarthritis of the Knee but Not of the Hip: The Rotterdam Study. *Annals of the Rheumatic Diseases* **2007**, *66* (2), 158–162.
- (39) Widmyer, M. R.; Utturkar, G. M.; Leddy, H. A.; Coleman, J. L.; Spritzer, C. E.; Moorman, C. T.; DeFrate, L. E.; Guilak, F. High Body Mass Index Is Associated With Increased Diurnal Strains in the Articular Cartilage of the Knee. *Arthritis & Rheumatism* **2013**, *65* (10), 2615–2622.
- (40) Grotle, M.; Hagen, K. B.; Natvig, B.; Dahl, F. A.; Kvien, T. K. Obesity and Osteoarthritis in Knee, Hip and/or Hand: An Epidemiological Study in the General Population with 10 Years Follow-Up. *BMC Musculoskelet Disord* **2008**, *9* (1), 132.
- (41) Martin, J. A.; Buckwalter, J. A. Aging, Articular Cartilage Chondrocyte Senescence and Osteoarthritis. *Biogerontology* **2002**, *3* (5), 257–264.
- (42) Jeon, O. H.; David, N.; Campisi, J.; Elisseeff, J. H. Senescent Cells and Osteoarthritis: A Painful Connection. *J Clin Invest* **2018**, *128* (4), 1229–1237.
- (43) Sharma, L.; Song, J.; Dunlop, D.; Felson, D.; Lewis, C. E.; Segal, N.; Torner, J.; Cooke, T. D. V.; Hietpas, J.; Lynch, J.; Nevitt, M. Varus and Valgus Alignment and Incident and Progressive Knee Osteoarthritis. *Annals of the Rheumatic Diseases* **2010**, *69* (11), 1940–1945.
- (44) Brouwer, G. M.; Tol, A. W. V.; Bergink, A. P.; Belo, J. N.; Bernsen, R. M. D.; Reijman, M.; Pols, H. a. P.; Bierma-Zeinstra, S. M. A. Association between Valgus and Varus Alignment and the Development and Progression of Radiographic Osteoarthritis of the Knee. *Arthritis & Rheumatism* **2007**, *56* (4), 1204–1211.
- (45) Lane, N. E.; Lin, P.; Christiansen, L.; Gore, L. R.; Williams, E. N.; Hochberg, M. C.; Nevitt, M. C. Association of Mild Acetabular Dysplasia with an Increased Risk of Incident Hip Osteoarthritis in Elderly White Women: The Study of Osteoporotic Fractures. *Arthritis & Rheumatism* **2000**, *43* (2), 400–404.
- (46) Gosvig, K. K.; Jacobsen, S.; Sonne-Holm, S.; Palm, H.; Troelsen, A. Prevalence of Malformations of the Hip Joint and Their Relationship to Sex, Groin Pain, and Risk of Osteoarthritis: A Population-Based Survey. *JBJS* **2010**, *92* (5), 1162–1169.
- (47) Doherty, M.; Courtney, P.; Doherty, S.; Jenkins, W.; Maciewicz, R. A.; Muir, K.; Zhang, W. Nonspherical Femoral Head Shape (Pistol Grip Deformity), Neck Shaft Angle, and Risk of Hip Osteoarthritis: A Case–Control Study. *Arthritis & Rheumatism* **2008**, *58* (10), 3172–3182.
- (48) Bardakos, N. V.; Villar, R. N. Predictors of Progression of Osteoarthritis in Femoroacetabular Impingement. *The Journal of Bone and Joint Surgery. British volume* **2009**, *91-B* (2), 162–169.

- (49) Mandelbaum, B. R.; Browne, J. E.; Fu, F.; Micheli, L.; Mosely, J. B.; Erggelet, C.; Minas, T.; Peterson, L. Articular Cartilage Lesions of the Knee. *Am J Sports Med* **1998**, *26* (6), 853–861.
- (50) Mankin, H. J. Biochemistry and Metabolism of Articular Cartilage in Osteoarthritis. *Osteoarthritis, diagnosis and medical/surgical management*. **1984**, 109–154.
- (51) Sah, R. L.; Yang, A. S.; Chen, A. C.; Hant, J. J.; Halili, R. B.; Yoshioka, M.; Amiel, D.; Coutts, R. D. Physical Properties of Rabbit Articular Cartilage after Transection of the Anterior Cruciate Ligament. *Journal of Orthopaedic Research* **1997**, *15* (2), 197–203.
- (52) Setton, L. A.; Elliott, D. M.; Mow, V. C. Altered Mechanics of Cartilage with Osteoarthritis: Human Osteoarthritis and an Experimental Model of Joint Degeneration. *Osteoarthritis and Cartilage* **1999**, *7* (1), 2–14.
- (53) Felson, D. T. Osteoarthritis as a Disease of Mechanics. *Osteoarthritis and Cartilage* **2013**, *21* (1), 10–15.
- (54) James Williams, H.; Ward, J. R.; Egger, M. J.; Neuner, R.; Brooks, R. H.; Clegg, D. O.; Field, E. H.; Skosey, J. L.; Alarcón, G. S.; Willkens, R. F.; Paulus, H. E.; Jon Russell, I.; Sharp, J. T. Comparison of Naproxen and Acetaminophen in a Two-Year Study of Treatment of Osteoarthritis of the Knee. *Arthritis & Rheumatism* **1993**, *36* (9), 1196–1206.
- (55) Bradley, J. D.; Brandt, K. D.; Katz, B. P.; Kalasinski, L. A.; Ryan, S. I. Comparison of an Antiinflammatory Dose of Ibuprofen, an Analgesic Dose of Ibuprofen, and Acetaminophen in the Treatment of Patients with Osteoarthritis of the Knee. *New England Journal of Medicine* **1991**, *325* (2), 87–91.
- (56) Clegg, D. O.; Reda, D. J.; Harris, C. L.; Klein, M. A.; O’Dell, J. R.; Hooper, M. M.; Bradley, J. D.; Bingham, C. O.; Weisman, M. H.; Jackson, C. G.; Lane, N. E.; Cush, J. J.; Moreland, L. W.; Schumacher, H. R.; Oddis, C. V.; Wolfe, F.; Molitor, J. A.; Yocum, D. E.; Schnitzer, T. J.; Furst, D. E.; Sawitzke, A. D.; Shi, H.; Brandt, K. D.; Moskowitz, R. W.; Williams, H. J. Glucosamine, Chondroitin Sulfate, and the Two in Combination for Painful Knee Osteoarthritis. *New England Journal of Medicine* **2006**, *354* (8), 795–808.
- (57) McAlindon, T. E.; LaValley, M. P.; Gulin, J. P.; Felson, D. T. Glucosamine and Chondroitin for Treatment of Osteoarthritis: A Systematic Quality Assessment and Meta-Analysis. *JAMA* **2000**, *283* (11), 1469–1475.
- (58) Reginster, J. Y.; Deroisy, R.; Rovati, L. C.; Lee, R. L.; Lejeune, E.; Bruyere, O.; Giacovelli, G.; Henrotin, Y.; Dacre, J. E.; Gossett, C. Long-Term Effects of Glucosamine Sulphate on Osteoarthritis Progression: A Randomised, Placebo-Controlled Clinical Trial. *The Lancet* **2001**, *357* (9252), 251–256.
- (59) Livesley, P.; Doherty, M.; Needoff, M.; Moulton, A. Arthroscopic Lavage of Osteoarthritic Knees. *The Journal of Bone and Joint Surgery. British volume* **1991**, *73-B* (6), 922–926.

- (60) Chang, R. W.; Falconer, J.; David Stulberg, S.; Arnold, W. J.; Manheim, L. M.; Dyer, A. R. A Randomized, Controlled Trial of Arthroscopic Surgery versus Closed-Needle Joint Lavage for Patients with Osteoarthritis of the Knee. *Arthritis & Rheumatism* **1993**, *36* (3), 289–296.
- (61) Gibson, J.; White, M.; Chapman, V.; Strachan, R. Arthroscopic Lavage and Debridement for Osteoarthritis of the Knee. *The Journal of Bone and Joint Surgery. British volume* **1992**, *74-B* (4), 534–537.
- (62) Moseley, J. B.; Wray, N. P.; Kuykendall, D.; Willis, K.; Landon, G. Arthroscopic Treatment of Osteoarthritis of the Knee: A Prospective, Randomized, Placebo-Controlled Trial: Results of a Pilot Study. *Am J Sports Med* **1996**, *24* (1), 28–34.
- (63) Kim, H. K.; Moran, M. E.; Salter, R. B. The Potential for Regeneration of Articular Cartilage in Defects Created by Chondral Shaving and Subchondral Abrasion. An Experimental Investigation in Rabbits. *J Bone Joint Surg Am* **1991**, *73* (9), 1301–1315.
- (64) Tew, S. R.; Kwan, A. P. L.; Hann, A.; Thomson, B. M.; Archer, C. W. The Reactions of Articular Cartilage to Experimental Wounding: Role of Apoptosis. *Arthritis & Rheumatism* **2000**, *43* (1), 215–225.
- (65) Mitchell, N.; Shepard, N. Effect of Patellar Shaving in the Rabbit. *Journal of Orthopaedic Research* **1987**, *5* (3), 388–392.
- (66) Hunziker, E. B.; Quinn, T. M. Surgical Removal of Articular Cartilage Leads to Loss of Chondrocytes from Cartilage Bordering the Wound Edge. *JBJS* **2003**, *85* (suppl_2), 85–92.
- (67) Glossop, N. D.; Jackson, R. W.; Koort, H. J.; Reed, S. C.; Randle, J. A. The Excimer Laser in Orthopaedics. *Clin Orthop Relat Res* **1995**, No. 310, 72–81.
- (68) Tabib, W.; Beaufils, P.; Blin, J. L.; Trémoulet, J.; Hardy, P. [Arthroscopic meniscectomy with Ho-Yag laser versus mechanical meniscectomy. Mid-term results of a randomized prospective study of 80 meniscectomies]. *Rev Chir Orthop Reparatrice Appar Mot* **1999**, *85* (7), 713–721.
- (69) Breinan, H. A.; Martin, S. D.; Hsu, H.-P.; Spector, M. Healing of Canine Articular Cartilage Defects Treated with Microfracture, a Type-II Collagen Matrix, or Cultured Autologous Chondrocytes. *Journal of Orthopaedic Research* **2000**, *18* (5), 781–789.
- (70) Knutsen, G.; Engebretsen, L.; Ludvigsen, T. C.; Drogset, J. O.; Grøntvedt, T.; Solheim, E.; Strand, T.; Roberts, S.; Isaksen, V.; Johansen, O. Autologous Chondrocyte Implantation Compared with Microfracture in the Knee: A Randomized Trial. *JBJS* **2004**, *86* (3), 455–464.
- (71) Mithoefer, K.; Williams, R. J. I.; Warren, R. F.; Potter, H. G.; Spock, C. R.; Jones, E. C.; Wickiewicz, T. L.; Marx, R. G. The Microfracture Technique for the Treatment of Articular Cartilage Lesions in the Knee: A Prospective Cohort Study. *JBJS* **2005**, *87* (9), 1911–1920.

- (72) Steadman, J. R.; Rodkey, W. G.; Singleton, S. B.; Briggs, K. K. Microfracture Technique Forfull-Thickness Chondral Defects: Technique and Clinical Results. *Operative Techniques in Orthopaedics* **1997**, 7 (4), 300–304.
- (73) Steadman, J. R.; Briggs, K. K.; Rodrigo, J. J.; Kocher, M. S.; Gill, T. J.; Rodkey, W. G. Outcomes of Microfracture for Traumatic Chondral Defects of the Knee: Average 11-Year Follow-Up. *Arthroscopy: The Journal of Arthroscopic & Related Surgery* **2003**, 19 (5), 477–484.
- (74) DiBartola, A. C.; Everhart, J. S.; Magnussen, R. A.; Carey, J. L.; Brophy, R. H.; Schmitt, L. C.; Flanigan, D. C. Correlation between Histological Outcome and Surgical Cartilage Repair Technique in the Knee: A Meta-Analysis. *The Knee* **2016**, 23 (3), 344–349.
- (75) Nehrer, S.; Spector, M.; Minas, T. Histologic Analysis of Tissue after Failed Cartilage Repair Procedures. *Clin Orthop Relat Res* **1999**, No. 365, 149–162.
- (76) Buckwalter, J. A.; Mow, V. C.; Ratcliffe, A. Restoration of Injured or Degenerated Articular Cartilage. *JAAOS - Journal of the American Academy of Orthopaedic Surgeons* **1994**, 2 (4), 192–201.
- (77) Knutsen, G.; Drogset, J. O.; Engebretsen, L.; Grøntvedt, T.; Isaksen, V.; Ludvigsen, T. C.; Roberts, S.; Solheim, E.; Strand, T.; Johansen, O. A Randomized Trial Comparing Autologous Chondrocyte Implantation with Microfracture: Findings at Five Years. *JBJS* **2007**, 89 (10), 2105–2112.
- (78) Saris, D. B. F.; Vanlauwe, J.; Victor, J.; Almqvist, K. F.; Verdonk, R.; Bellemans, J.; Luyten, F. P. Treatment of Symptomatic Cartilage Defects of the Knee: Characterized Chondrocyte Implantation Results in Better Clinical Outcome at 36 Months in a Randomized Trial Compared to Microfracture. *Am J Sports Med* **2009**, 37 (1_suppl), 10–19.
- (79) Kon, E.; Gobbi, A.; Filardo, G.; Delcogliano, M.; Zaffagnini, S.; Marcacci, M. Arthroscopic Second-Generation Autologous Chondrocyte Implantation Compared with Microfracture for Chondral Lesions of the Knee: Prospective Nonrandomized Study at 5 Years. *Am J Sports Med* **2009**, 37 (1), 33–41.
- (80) Basad, E.; Ishaque, B.; Bachmann, G.; Stürz, H.; Steinmeyer, J. Matrix-Induced Autologous Chondrocyte Implantation versus Microfracture in the Treatment of Cartilage Defects of the Knee: A 2-Year Randomised Study. *Knee surgery, sports traumatology, arthroscopy* **2010**, 18 (4), 519–527.
- (81) Saris, D. B. F.; Vanlauwe, J.; Victor, J.; Haspl, M.; Bohnsack, M.; Fortems, Y.; Vandekerckhove, B.; Almqvist, K. F.; Claes, T.; Handelberg, F.; Lagae, K.; van der Bauwhede, J.; Vandenuecker, H.; Yang, K. G. A.; Jelic, M.; Verdonk, R.; Veulemans, N.; Bellemans, J.; Luyten, F. P. Characterized Chondrocyte Implantation Results in Better Structural Repair When Treating Symptomatic Cartilage Defects of the Knee in a Randomized Controlled Trial versus Microfracture. *Am J Sports Med* **2008**, 36 (2), 235–246.

- (82) Basad, E.; Stürz, H.; Steinmeyer, J. Treatment of Chondral Defects with MACI or Microfracture. First Results of a Comparative Clinical Study. *Orthopädische Praxis* **2004**, *40*, 6–10.
- (83) Hangody, L.; Vásárhelyi, G.; Hangody, L. R.; Sükösd, Z.; Tibay, G.; Bartha, L.; Bodó, G. Autologous Osteochondral Grafting—Technique and Long-Term Results. *Injury* **2008**, *39* (1, Supplement), 32–39.
- (84) Hangody, L.; Dobos, J.; Baló, E.; Pánics, G.; Hangody, L. R.; Berkes, I. Clinical Experiences With Autologous Osteochondral Mosaicplasty in an Athletic Population: A 17-Year Prospective Multicenter Study. *Am J Sports Med* **2010**, *38* (6), 1125–1133.
- (85) Jakob, R. P.; Franz, T.; Gautier, E.; Mainil-Varlet, P. Autologous Osteochondral Grafting in the Knee: Indication, Results, and Reflections. *Clinical Orthopaedics and Related Research (1976-2007)* **2002**, *401*, 170–184.
- (86) Kock, N. B.; van Tankeren, E.; Oyen, W. J. G.; Wymenga, A. B.; van Susante, J. L. C. Bone Scintigraphy after Osteochondral Autograft Transplantation in the Knee. *Acta Orthopaedica* **2010**, *81* (2), 206–210.
- (87) Koulalis, D.; Schultz, W.; Heyden, M.; König, F. Autologous Osteochondral Grafts in the Treatment of Cartilage Defects of the Knee Joint. *Knee Surg Sports Traumatol Arthrosc* **2004**, *12* (4), 329–334.
- (88) Quarch, V. M. A.; Enderle, E.; Lotz, J.; Frosch, K.-H. Fate of Large Donor Site Defects in Osteochondral Transfer Procedures in the Knee Joint with and without TruFit Plugs. *Arch Orthop Trauma Surg* **2014**, *134* (5), 657–666.
- (89) Reverte-Vinaixa, M. M.; Joshi, N.; Díaz-Ferreiro, E. W.; Teixidor-Serra, J.; Domínguez-Oronoz, R. Medium-Term Outcome of Mosaicplasty for Grade III-IV Cartilage Defects of the Knee. *J Orthop Surg (Hong Kong)* **2013**, *21* (1), 4–9.
- (90) Harris, W. H.; Sledge, C. B. Total Hip and Total Knee Replacement. *New England Journal of Medicine* **1990**, *323* (11), 725–731.
- (91) Labek, G.; Thaler, M.; Janda, W.; Agreiter, M.; Stöckl, B. Revision Rates after Total Joint Replacement. *The Journal of Bone and Joint Surgery. British volume* **2011**, *93-B* (3), 293–297.
- (92) Erickson, I. E.; Kestle, S. R.; Zellars, K. H.; Farrell, M. J.; Kim, M.; Burdick, J. A.; Mauck, R. L. High Mesenchymal Stem Cell Seeding Densities in Hyaluronic Acid Hydrogels Produce Engineered Cartilage with Native Tissue Properties. *Acta Biomaterialia* **2012**, *8* (8), 3027–3034.
- (93) Chung, C.; Burdick, J. A. Influence of Three-Dimensional Hyaluronic Acid Microenvironments on Mesenchymal Stem Cell Chondrogenesis. *Tissue Engineering Part A* **2009**, *15* (2), 243–254.

- (94) Almeida, H. V.; Eswaremoorthy, R.; Cunniffe, G. M.; Buckley, C. T.; O'Brien, F. J.; Kelly, D. J. Fibrin Hydrogels Functionalized with Cartilage Extracellular Matrix and Incorporating Freshly Isolated Stromal Cells as an Injectable for Cartilage Regeneration. *Acta Biomaterialia* **2016**, *36*, 55–62.
- (95) Naderi-Meshkin, H.; Andreas, K.; Matin, M. M.; Sittinger, M.; Bidkhorji, H. R.; Ahmadiankia, N.; Bahrami, A. R.; Ringe, J. Chitosan-Based Injectable Hydrogel as a Promising in Situ Forming Scaffold for Cartilage Tissue Engineering. *Cell Biology International* **2014**, *38* (1), 72–84.
- (96) Chao, P.-H. G.; Yodmuang, S.; Wang, X.; Sun, L.; Kaplan, D. L.; Vunjak-Novakovic, G. Silk Hydrogel for Cartilage Tissue Engineering. *Journal of Biomedical Materials Research Part B: Applied Biomaterials* **2010**, *95B* (1), 84–90.
- (97) Noguchi, T.; Yamamuro, T.; Oka, M.; Kumar, P.; Kotoura, Y.; Hyonyt, S.-H.; Ikadat, Y. Poly(Vinyl Alcohol) Hydrogel as an Artificial Articular Cartilage: Evaluation of Biocompatibility. *Journal of Applied Biomaterials* **1991**, *2* (2), 101–107.
- (98) Oka, M.; Ushio, K.; Kumar, P.; Ikeuchi, K.; Hyon, S. H.; Nakamura, T.; Fujita, H. Development of Artificial Articular Cartilage. *Proc Inst Mech Eng H* **2000**, *214* (1), 59–68.
- (99) Maher, S. a.; Doty, S. b.; Torzilli, P. a.; Thornton, S.; Lowman, A. m.; Thomas, J. d.; Warren, R.; Wright, T. m.; Myers, E. Nondegradable Hydrogels for the Treatment of Focal Cartilage Defects. *Journal of Biomedical Materials Research Part A* **2007**, *83A* (1), 145–155.
- (100) Nguyen, L. H.; Kudva, A. K.; Saxena, N. S.; Roy, K. Engineering Articular Cartilage with Spatially-Varying Matrix Composition and Mechanical Properties from a Single Stem Cell Population Using a Multi-Layered Hydrogel. *Biomaterials* **2011**, *32* (29), 6946–6952.
- (101) Nguyen, Q. T.; Hwang, Y.; Chen, A. C.; Varghese, S.; Sah, R. L. Cartilage-like Mechanical Properties of Poly (Ethylene Glycol)-Diacrylate Hydrogels. *Biomaterials* **2012**, *33* (28), 6682–6690.
- (102) Schoonraad, S. A.; Fischenich, K. M.; Eckstein, K. N.; Crespo-Cuevas, V.; Savard, L. M.; Muralidharan, A.; Tomaschke, A. A.; Uzcategui, A. C.; Randolph, M. A.; McLeod, R. R.; Ferguson, V. L.; Bryant, S. J. Biomimetic and Mechanically Supportive 3D Printed Scaffolds for Cartilage and Osteochondral Tissue Engineering Using Photopolymers and Digital Light Processing. *Biofabrication* **2021**, *13* (4), 044106.
- (103) Zhang, X.; Yan, Z.; Guan, G.; Lu, Z.; Yan, S.; Du, A.; Wang, L.; Li, Q. Polyethylene Glycol Diacrylate Scaffold Filled with Cell-Laden Methacrylamide Gelatin/Alginate Hydrogels Used for Cartilage Repair. *J Biomater Appl* **2021**, 08853282211044853..
- (104) Aisenbrey, E. A.; Tomaschke, A.; Kleinjan, E.; Muralidharan, A.; Pascual-Garrido, C.; McLeod, R. R.; Ferguson, V. L.; Bryant, S. J. A Stereolithography-Based 3D Printed Hybrid Scaffold for In Situ Cartilage Defect Repair. *Macromolecular Bioscience* **2018**, *18* (2), 1700267.

- (105) Wichterle, O.; Lím, D. Hydrophilic Gels for Biological Use. *Nature* **1960**, *185* (4706), 117–118.
- (106) Oyen, M. L. Mechanical Characterisation of Hydrogel Materials. *International Materials Reviews* **2014**, *59* (1), 44–59.
- (107) Ahmed, E. M. Hydrogel: Preparation, Characterization, and Applications: A Review. *Journal of Advanced Research* **2015**, *6* (2), 105–121.
- (108) Oyen, M. L. Mechanical Characterisation of Hydrogel Materials. *International Materials Reviews* **2014**, *59* (1), 44–59.
- (109) Gyles, D. A.; Castro, L. D.; Silva, J. O. C.; Ribeiro-Costa, R. M. A Review of the Designs and Prominent Biomedical Advances of Natural and Synthetic Hydrogel Formulations. *European Polymer Journal* **2017**, *88*, 373–392.
- (110) Xiong, J.-Y.; Narayanan, J.; Liu, X.-Y.; Chong, T. K.; Chen, S. B.; Chung, T.-S. Topology Evolution and Gelation Mechanism of Agarose Gel. *J. Phys. Chem. B* **2005**, *109* (12), 5638–5643.
- (111) Karimi, A.; Navidbakhsh, M. Mechanical Properties of PVA Material for Tissue Engineering Applications. *Materials Technology* **2014**, *29* (2), 90–100.
- (112) Deiber, J. A.; Ottone, M. L.; Piaggio, M. V.; Peirotti, M. B. Characterization of Cross-Linked Polyampholytic Gelatin Hydrogels through the Rubber Elasticity and Thermodynamic Swelling Theories. *Polymer* **2009**, *50* (25), 6065–6075.
- (113) Fukubayashi, T.; Kurosawa, H. The Contact Area and Pressure Distribution Pattern of the Knee: A Study of Normal and Osteoarthrotic Knee Joints. *Acta Orthopaedica Scandinavica* **1980**, *51* (1–6), 871–879.
- (114) Brand, R. A. Joint Contact Stress. *Iowa Orthop J* **2005**, *25*, 82–94.
- (115) Alexopoulos, L. G.; Williams, G. M.; Upton, M. L.; Setton, L. A.; Guilak, F. Osteoarthritic Changes in the Biphasic Mechanical Properties of the Chondrocyte Pericellular Matrix in Articular Cartilage. *Journal of Biomechanics* **2005**, *38* (3), 509–517.
- (116) Gong, J. p.; Katsuyama, Y.; Kurokawa, T.; Osada, Y. Double-Network Hydrogels with Extremely High Mechanical Strength. *Advanced Materials* **2003**, *15* (14), 1155–1158.
- (117) Evans, A. G.; Rühle, M.; Dalgleish, B. J.; Charalambides, P. G. The Fracture Energy of Bimaterial Interfaces. *Metall Mater Trans A* **1990**, *21* (9), 2419–2429.
- (118) Zawko, S. A.; Suri, S.; Truong, Q.; Schmidt, C. E. Photopatterned Anisotropic Swelling of Dual-Crosslinked Hyaluronic Acid Hydrogels. *Acta Biomaterialia* **2009**, *5* (1), 14–22.

- (119) Lee, Y. D.; Erdogan, F. Residual/Thermal Stresses in FGM and Laminated Thermal Barrier Coatings. *International Journal of Fracture* **1994**, *69* (2), 145–165.
- (120) Hasanov, S.; Gupta, A.; Nasirov, A.; Fidan, I. Mechanical Characterization of Functionally Graded Materials Produced by the Fused Filament Fabrication Process. *Journal of Manufacturing Processes* **2020**, *58*, 923–935.
- (121) Muralidharan, A.; Uzcategui, A. C.; McLeod, R. R.; Bryant, S. J. Stereolithographic 3D Printing for Deterministic Control over Integration in Dual-Material Composites. *Advanced Materials Technologies* **2019**, *4* (11), 1900592.
- (122) HERTZ, H. On the Contact of Elastic Solids. *Z. Reine Angew. Mathematik* **1881**, *92*, 156–171.
- (123) Boussinesq, J. Application Des Potentiels à l'étude de l'équilibre et Du Mouvement Des Solides Élastiques: Principalement Au Calcul Des Déformations et Des Pressions Que Produisent, Dans Ces Solides, Des Efforts Quelconques Exercés Sur Une Petite Partie de Leur Surface Ou de Leur Intérieur: Mémoire Suivi de Notes Étendues Sur Divers Points de Physique, Mathématique et d'analyse; Gauthier-Villars, 1885; Vol. 4.
- (124) Sneddon, I. N. Boussinesq's Problem for a Rigid Cone. *Mathematical Proceedings of the Cambridge Philosophical Society* **1948**, *44* (4), 492–507.
- (125) Sneddon, I. N. The Relation between Load and Penetration in the Axisymmetric Boussinesq Problem for a Punch of Arbitrary Profile. *International journal of engineering science* **1965**, *3* (1), 47–57.
- (126) Oliver, W. C.; Pharr, G. M. An Improved Technique for Determining Hardness and Elastic Modulus Using Load and Displacement Sensing Indentation Experiments. *Journal of Materials Research* **1992**, *7* (6), 1564–1583.
- (127) Oliver, W. C.; Pharr, G. M. Measurement of Hardness and Elastic Modulus by Instrumented Indentation: Advances in Understanding and Refinements to Methodology. *Journal of Materials Research* **2004**, *19* (1), 3–20.
- (128) Tabor, D.; Taylor, G. I. A Simple Theory of Static and Dynamic Hardness. *Proceedings of the Royal Society of London. Series A. Mathematical and Physical Sciences* **1948**, *192* (1029), 247–274.
- (129) Stilwell, N. A.; Tabor, D. Elastic Recovery of Conical Indentations. *Proc. Phys. Soc.* **1961**, *78* (2), 169–179.
- (130) Bulychev, S. I. Mechanical Properties of Materials Studied from Kinetic Diagrams of Load versus Depth of Impression during Microimpression. *Prob. Prochn.* **9**, 79 (1976) SI Bulychev, VP Alekhin. *Zavod Lab* **1987**, *53*, 76.

- (131) Bulychev, S. I.; Alekhin, V. P.; Shorshorov, M. Kh.; Ternovskii, A. P. Mechanical Properties of Materials Studied from Kinetic Diagrams of Load versus Depth of Impression during Microimpression. *Strength Mater* **1976**, *8* (9), 1084–1089.
- (132) Bulychev, S. I.; Alekhin, V. P.; Shorshorov, M. K.; Ternovskij, A. P.; Shnyrev, G. D. Determination of Young Modulus by the Hardness Indentation Diagram. *Zavodskaya Laboratoriya* **1975**, *41* (9), 1137–1140.
- (133) Ternovskii, A. P.; Alekhin, V. P.; Shorshorov, M. K.; Khrushchev, M. M.; Skvortsov, V. N. The Character of the Variation of Microhardness with Indentation Size and the Deformation Behavior of Materials under Conditions of Concentrated Surface Loading. *Zavodskaya Laboratoriya* **1973**, *39* (1242), 20.
- (134) Shorshorov, M. K.; Bulychev, S. I.; ALEKHIN, V. The Work of Plastic and Elastic-Deformation during Indicator Impression. *DOKLADY AKADEMII NAUK SSSR* **1981**, *259* (4), 839–842.
- (135) Pethicai, J. B.; Hutchings, R.; Oliver, W. C. Hardness Measurement at Penetration Depths as Small as 20 Nm. *Philosophical Magazine A* **1983**, *48* (4), 593–606.
- (136) Blau, P. J. Microindentation Techniques in Materials Science and Engineering: A Symposium Sponsored by ASTM Committee E-4 on Metallography and by the International Metallographic Society, Philadelphia, PA, 15-18 July 1984; Astm International, 1986.
- (137) Doerner, M. F.; Nix, W. D. A Method for Interpreting the Data from Depth-Sensing Indentation Instruments. *Journal of Materials Research* **1986**, *1* (04), 601–609.
- (138) Oyen, M. L. Spherical Indentation Creep Following Ramp Loading. *Journal of Materials Research* **2005**, *20* (08), 2094–2100.
- (139) Mattice, J. M.; Lau, A. G.; Oyen, M. L.; Kent, R. W. Spherical Indentation Load-Relaxation of Soft Biological Tissues. *Journal of Materials Research* **2006**, *21* (8), 2003–2010.
- (140) Mak, A. F.; Lai, W. M.; Mow, V. C. Biphasic Indentation of Articular Cartilage—I. Theoretical Analysis. *Journal of Biomechanics* **1987**, *20* (7), 703–714.
- (141) Mow, V. C.; Gibbs, M. C.; Lai, W. M.; Zhu, W. B.; Athanasiou, K. A. Biphasic Indentation of Articular Cartilage—II. A Numerical Algorithm and an Experimental Study. *Journal of Biomechanics* **1989**, *22* (8), 853–861.
- (142) Chaudhuri, O.; Gu, L.; Darnell, M.; Klumpers, D.; Bencherif, S. A.; Weaver, J. C.; Huebsch, N.; Mooney, D. J. Substrate Stress Relaxation Regulates Cell Spreading. *Nat Commun* **2015**, *6* (1), 6365.

- (143) Chaudhuri, O.; Gu, L.; Klumpers, D.; Darnell, M.; Bencherif, S. A.; Weaver, J. C.; Huebsch, N.; Lee, H.; Lippens, E.; Duda, G. N.; Mooney, D. J. Hydrogels with Tunable Stress Relaxation Regulate Stem Cell Fate and Activity. *Nature Materials* **2016**, *15* (3), 326–334..
- (144) Galli, M.; Oyen, M. L. Spherical Indentation of a Finite Poroelastic Coating. *Appl. Phys. Lett.* **2008**, *93* (3), 031911.
- (145) Ebenstein, D. M. Nano-JKR Force Curve Method Overcomes Challenges of Surface Detection and Adhesion for Nanoindentation of a Compliant Polymer in Air and Water. *Journal of Materials Research* **2011**, *26* (08), 1026–1035.
- (146) Ebenstein, D. M.; Wahl, K. J. A Comparison of JKR-Based Methods to Analyze Quasi-Static and Dynamic Indentation Force Curves. *Journal of Colloid and Interface Science* **2006**, *298* (2), 652–662..
- (147) Kohn, J. C.; Ebenstein, D. M. Eliminating Adhesion Errors in Nanoindentation of Compliant Polymers and Hydrogels. *Journal of the Mechanical Behavior of Biomedical Materials* **2013**, *20*, 316–326.
- (148) Johnson, K. L.; Kendall, K.; Roberts, A. D. Surface Energy and the Contact of Elastic Solids. *Proceedings of the Royal Society A: Mathematical, Physical and Engineering Sciences* **1971**, *324* (1558), 301–313.
- (149) Holm, R. Wissenschaftliche Veröffentlichungen Aus Den Siemens. *Werken* **1929**, *7* (2), 217–258.
- (150) Archard, J. F.; Allibone, T. E. Elastic Deformation and the Laws of Friction. *Proceedings of the Royal Society of London. Series A. Mathematical and Physical Sciences* **1957**, *243* (1233), 190–205.
- (151) Greenwood, J. A.; Johnson, K. L.; Matsubara, E. A Surface Roughness Parameter in Hertz Contact. *Wear* **1984**, *100* (1), 47–57.
- (152) Xia, Y.; Bigerelle, M.; Marteau, J.; Mazeran, P.-E.; Bouvier, S.; Iost, A. Effect of Surface Roughness in the Determination of the Mechanical Properties of Material Using Nanoindentation Test. *Scanning* **2014**, *36* (1), 134–149.
- (153) Wai, S. W.; Spinks, G. M.; Brown, H. R.; Swain, M. Surface Roughness: Its Implications and Inference with Regards to Ultra Microindentation Measurements of Polymer Mechanical Properties. *Polymer Testing* **2004**, *23* (5), 501–507.
- (154) Chung, S. M.; Yap, A. U. J. Effects of Surface Finish on Indentation Modulus and Hardness of Dental Composite Restoratives. *Dental Materials* **2005**, *21* (11), 1008–1016.

- (155) Donnelly, E.; Baker, S. P.; Boskey, A. L.; van der Meulen, M. C. H. Effects of Surface Roughness and Maximum Load on the Mechanical Properties of Cancellous Bone Measured by Nanoindentation. *J Biomed Mater Res A* **2006**, *77* (2), 426–435.
- (156) Qasmi, M.; Delobelle, P. Influence of the Average Roughness Rms on the Precision of the Young's Modulus and Hardness Determination Using Nanoindentation Technique with a Berkovich Indenter. *Surface and Coatings Technology* **2006**, *201* (3), 1191–1199.
- (157) Miller, M.; Bobko, C.; Vandamme, M.; Ulm, F.-J. Surface Roughness Criteria for Cement Paste Nanoindentation. *Cement and Concrete Research* **2008**, *38* (4), 467–476.
- (158) Chen, Z.; Diebels, S. Modelling and Parameter Re-Identification of Nanoindentation of Soft Polymers Taking into Account Effects of Surface Roughness. *Computers & Mathematics with Applications* **2012**, *64* (9), 2775–2786.
- (159) Ritchie, R. O.; Liu, D. Chapter 2 - Foundations of Fracture Mechanics. In *Introduction to Fracture Mechanics*; Ritchie, R. O., Liu, D., Eds.; Elsevier, 2021; pp 3–9.
- (160) Irwin, G. R. Onset of Fast Crack Propagation in High Strength Steel and Aluminum Alloys; Naval Research Lab Washington DC, 1956.
- (161) Zhang, T.; Lin, S.; Yuk, H.; Zhao, X. Predicting Fracture Energies and Crack-Tip Fields of Soft Tough Materials. *Extreme Mechanics Letters* **2015**, *4*, 1–8.
- (162) Creton, C.; Ciccotti, M. Fracture and Adhesion of Soft Materials: A Review. *Rep. Prog. Phys.* **2016**, *79* (4), 046601.
- (163) Mayumi, K.; Guo, J.; Narita, T.; Hui, C. Y.; Creton, C. Fracture of Dual Crosslink Gels with Permanent and Transient Crosslinks. *Extreme Mechanics Letters* **2016**, *6*, 52–59.
- (164) Greensmith, H. W. Rupture of Rubber. X. The Change in Stored Energy on Making a Small Cut in a Test Piece Held in Simple Extension. *Journal of Applied Polymer Science* **1963**, *7* (3), 993–1002.
- (165) Lee, W. Y.; Stinton, D. P.; Berndt, C. C.; Erdogan, F.; Lee, Y.-D.; Mutasim, Z. Concept of Functionally Graded Materials for Advanced Thermal Barrier Coating Applications. *Journal of the American Ceramic Society* **1996**, *79* (12), 3003–3012.
- (166) Delale, F.; Erdogan, F. Interface Crack in a Nonhomogeneous Elastic Medium. *International Journal of Engineering Science* **1988**, *26* (6), 559–568.
- (167) Chen, Y. F.; Erdogan, F. The Interface Crack Problem for a Nonhomogeneous Coating Bonded to a Homogeneous Substrate. *Journal of the Mechanics and Physics of Solids* **1996**, *44* (5), 771–787.

(168) Shbeeb, N. I.; Binienda, W. K. Analysis of an Interface Crack for a Functionally Graded Strip Sandwiched between Two Homogeneous Layers of Finite Thickness. *Engineering Fracture Mechanics* **1999**, *64* (6), 693–720.

(169) Marur, P. R.; Tippur, H. V. Numerical Analysis of Crack-Tip Fields in Functionally Graded Materials with a Crack Normal to the Elastic Gradient. *International Journal of Solids and Structures* **2000**, *37* (38), 5353–5370.

(170) Mirzaali, M. J.; Herranz de la Nava, A.; Gunashekar, D.; Nouri-Goushki, M.; Veeger, R. P. E.; Grossman, Q.; Angeloni, L.; Ghatkesar, M. K.; Fratila-Apachitei, L. E.; Ruffoni, D.; Doubrovski, E. L.; Zadpoor, A. A. Mechanics of Bioinspired Functionally Graded Soft-Hard Composites Made by Multi-Material 3D Printing. *Composite Structures* **2020**, *237*, 111867.

CHAPTER 2

Surface Roughness Influences Microindentation Property

Assessment of Agarose Hydrogels

2.1.0 Abstract

Surface roughness is understood to have an effect on the indentation of stiff materials but is typically ignored during the characterization of soft tissues and hydrogels and contributes to inaccurate microscale property assessments. To elucidate the influence of surface roughness on the measured properties of soft, hydrated materials, agarose gels were prepared with different surface roughness profiles to produce surfaces of controlled roughness, with the “rough” surface having more than 4x the roughness of the “smooth” surface ($S_q = 414 \pm 202$ nm vs. $S_q = 71 \pm 7$ nm, respectively). Indentation was performed on each surface using three different probe radii ($R_i = 50$ to 250 μm) and four different displacement rates ($\dot{\delta} = 1$ to 50 $\mu\text{m/s}$) to assess the influence of surface roughness on the effective contact modulus, equilibrium modulus, and fluid load fraction, calculated using Hertz Biphasic theory. The presence of a rough surface decreased moduli by up to 51% as compared to moduli measured using the “smooth” surface while the fluid load fraction remained unaltered. The dependence of the measurands on varying probe radius and displacement are also investigated, revealing that the equilibrium modulus increases with probe radius and indentation depth. Surfaces were

evaluated using Cryo Scanning Electron Microscopy (SEM) and Focused Ion Beam Milling (FIB), demonstrating markedly different near-surface regions in rough and smooth samples. Our results suggest that surface roughness profiles generated from different sectioning techniques may have a two-fold effect on the observed indentation behavior. In addition to altering the area of the probe of contact, the sectioned surface may also behave as a near-surface region of decreased stiffness.

2.2.0 Introduction

Microindentation is a valuable tool in the development of novel hydrogel materials for tissue engineering applications. Similar to macroscopic compression testing, microindentation permits the assessment of viscoelastic¹, biphasic²⁻⁴, and quasi-static mechanical behavior of hydrogels, but permits assessment of much smaller material volumes⁵. Thus, multiple indentation tests can be performed on a single sample to assess local heterogeneity and map property gradients⁶⁻⁸. These are key components of soft tissues (e.g., articular cartilage) that we seek to emulate using 3D printed hydrogels and graded soft material interfaces^{9,10}. The ability to perform multiple tests on a single surface represents an advantage over macroscopic compression testing, but also demonstrates the surface-sensitivity of indentation testing. If the surface of a sample differs from the underlying material, the properties measured via microindentation are not representative of the bulk material¹¹⁻¹⁴. A thorough understanding of how different surface characteristics influence the microindentation behavior of hydrogels is therefore needed to facilitate accurate assessments of mechanical properties beyond the macroscale.

One surface characteristic known to influence mechanical properties measured via microindentation is the surface roughness profile. Surface roughness is the deviation of a surface's topography from that of an ideal, flat surface. Deviations typically occur in the form of asperities created during sample preparation (e.g., roughness of the mold, sectioning, and grinding/polishing). These asperities, and the gaps between them, form peaks and valleys on the surface of a material. Contact with the peaks and valleys on a rough surface alters the well-defined relationship between displacement and contact area assumed for indentation analyses and leads to errors in the resulting properties. Many research groups have sought to elucidate the influence of surface roughness on microindentation measurements of different materials using varying probe geometries¹⁵⁻¹⁹. Greenwood, Johnson, and Matsuaba, investigated the condition of small wavelengths (i.e., small spacing between asperities) relative to the dimensions of contact on roughened copper surfaces. Under these conditions, the actual contact area was always reduced compared to the nominal area on a smooth surface and decreased the measured modulus of the material¹⁵. Wai *et al.* demonstrated the same effect using glassy a polymer surface but added that the influence of surface roughness could be eliminated by indenting to depths deep enough to flatten the largest asperities under contact¹⁶. In the case of large wavelengths relative to the dimensions of contact, surface roughness appears to influence the variation but not the mean of the measured properties. Donnelly *et al.*, using rough and smooth bone samples, found that the mean moduli did not differ but the coefficient of variance of measurements made on the rough sample was increased by 25 to 100% compared to the smooth sample¹⁷. Additionally, it was found that the influence of surface roughness was eliminated by indenting to depths approximately 3 times greater than the

measured RMS surface roughness. Chen & Diebels investigated both conditions of small and large wavelengths on contact with rough PDMS and silicone rubber surfaces using finite element simulations and found consistently reduced contact areas when the wavelength was smaller than half the radius of the indentation probe in contrast to an increased variation when the wavelength was larger¹⁸.

These previous investigations suggest the influence of surface roughness is dependent on both the indentation depth relative to the asperity heights and the probe radius relative to the wavelength. However, it remains unclear if rough hydrogel surfaces behave similarly to the previously investigated material types. Steel, bone, and glassy polymers are single-phase, elastic-plastic materials whose indentation response is determined by the amount of material in contact⁵. Hydrogels are biphasic materials, meaning that the material is composed of both a solid network and a fluid that resides in the interstitial spaces of the solid network²⁰. The indentation response of hydrogels depends on both the deformation of the elastic network and the movement of fluid through the network over time^{1,2,4,21}. To our knowledge, the influence of surface roughness on the mechanical properties evaluated via microindentation remains uninvestigated. An understanding of the influence of surface roughness would further our ability to accurately assess the mechanical properties of hydrogel materials. This knowledge would allow researchers engineer biomimetic hydrogel tissue scaffolds with functional gradients found in many soft tissues.

This study seeks to perform a comprehensive analysis of how surface roughness influences microindentation property determination of hydrogel materials. We performed a parametric indentation study using agarose, a biphasic, highly tunable, isotropic, and physically

crosslinked, hydrogel^{6,22}. Biphasic material behaviors of agarose gels with rough and smooth surfaces were evaluated using systematic loading and unloading microindentation tests while varying conospherical probe radii and displacement rate. We aimed to both elucidate how surface roughness of agarose gel samples influences measured apparent indentation and equilibrium moduli and to describe how the influence of surface roughness affects fluid load support.

2.3.0 Methods

2.3.1 Materials

To create agarose materials for this study, 5, 7.5, and 10 wt. % agarose powder (SIGMA A9539) was mixed with 0.01 M phosphate buffered solution (PBS) and heated to 90°C in a water bath with constant stirring (10-15 min). The agarose mixture was then poured into a 50 ml conical vial and centrifuged at 2000 rpm for 5 min to force out trapped gases as the mixture solidified.

2.3.2 Sample preparation

To prepare individual samples with different surface roughness profiles, the vials containing agarose were cut into 3 mm sections using a diamond wafering blade (~300 grit). Two samples were excised from each 3 mm thick section using an 8 mm biopsy punch. One sample was glued to a steel AFM puck using a thin layer of cyanoacrylate to serve as the “rough” sample. The other sample was further sectioned using a vibratome to produce a “smooth” surface (Fig. 2.1). Samples were stored at 3 °C in a hydrated state to limit degradation.

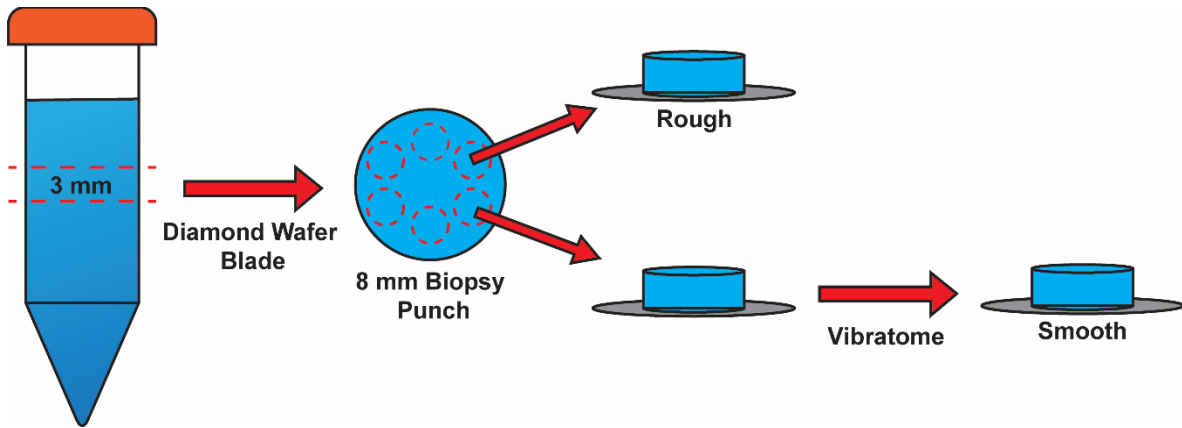


Figure 2. 1 Sample Preparation: Workflow to Produce Rough & Smooth surfaces. 1. Agarose gels were cast in 50 ml conical vials. 2. Vials were cut into 3 mm thick sections using a diamond wafer blade. 3. An 8 mm diameter biopsy punch was used to create two cylindrical samples 4. One sample was set aside to serve as the "rough" surface, the other was further sectioned using a vibratome to produce a "smooth" surface.

2.3.3 Surface roughness measurements

To verify that the methods of sample preparation produced the desired surface roughness profiles, Rough and Smooth samples were evaluated using a Keyence VK-X1000 confocal laser scanning microscope with a 50× objective (Keyence Corporation of America, Itasca, IL). For each sample, three representative areas were profiled. Surface roughness parameters vary with the size of the area evaluated¹⁶. As surface roughness parameters are most representative when evaluated over an area equal to the size of contact, the RMS surface roughness, S_q , was evaluated for 9 sub-regions with lateral dimensions equal to dimensions of contact. This analysis was repeated for each probe radius used during testing.

In addition to the RMS roughness, the height difference between the highest peak and lowest valley under contact was evaluated using a custom Matlab (MathWorks, USA) script. First, the surface heights for each representative area were exported from the Keyence analysis software and imported into Matlab. Then, for each probe radius used during testing, the maximum peak to valley distance, S_z , was evaluated using a moving area with dimensions equal

to the size of contact. Peak to valley measurements estimate how far the probe needs to be displaced into the sample before the asperities under contact are flattened.

Lastly, the average RMS peak spacing, $R_{\lambda q}$, was evaluated in the horizontal and vertical directions for each of the representative areas. The horizontal and vertical peak spacings were then averaged to define a global average peak spacing.

2.3.4 Cryogenic SEM and FIB measurements

To evaluate near-surface sample morphology of the 10 wt% agarose hydrogels, scanning electron microscopy (SEM) and focused ion beam (FIB) experiments were performed on a Scios 2 Dual Beam SEM/FIB equipped with a Leica VCT cryogenic stage cooled to $-150\text{ }^{\circ}\text{C}$. Hydrated samples were plunge frozen in liquid nitrogen (LN_2), coated with 7 nm of Pt using a cryo-sputter coater (ACE 600), and transferred to the cryo-SEM/FIB cold and under vacuum using the Leica VCT500 shuttle. An additional protective layer of Pt ($\sim 0.25\text{ }\mu\text{m}$) was applied to the area of interest prior to milling. To protect the beam sensitive samples secondary electron imaging was performed at $5\text{ keV}/50\text{ pA}$ and Ga^+ ion FIB milling performed with an accelerating voltage of 16 keV .

Image J (Rasband, W.S., ImageJ, U. S. National Institutes of Health, Bethesda, Maryland, USA, 1997-2018.) was used subsequently to estimate asperity heights from a subset of the collected SEM images.

2.3.5 Microindentation measurements

Depth-sensing indentation measurements were performed using a TI-950 Triboindenter (Bruker, Eden Prairie, MN) with an XZ500 extended displacement stage in displacement control.

For 10 wt. % agarose, three probe radii ($R_i = 50, 105, \text{ and } 250 \mu\text{m}$) and four displacement rates ($\dot{\delta} = 1, 5, 10, \text{ and } 50 \mu\text{m/s}$) were used to indent the rough and smooth surfaces (Fig. 2.2). For the 5 and 7.5 wt. % samples, only the largest probe radius was utilized. Prior to testing, samples were allowed to equilibrate while submerged in 0.01 M PBS for 2 hrs. Samples remained submerged in PBS throughout the course of testing to prevent dehydration.

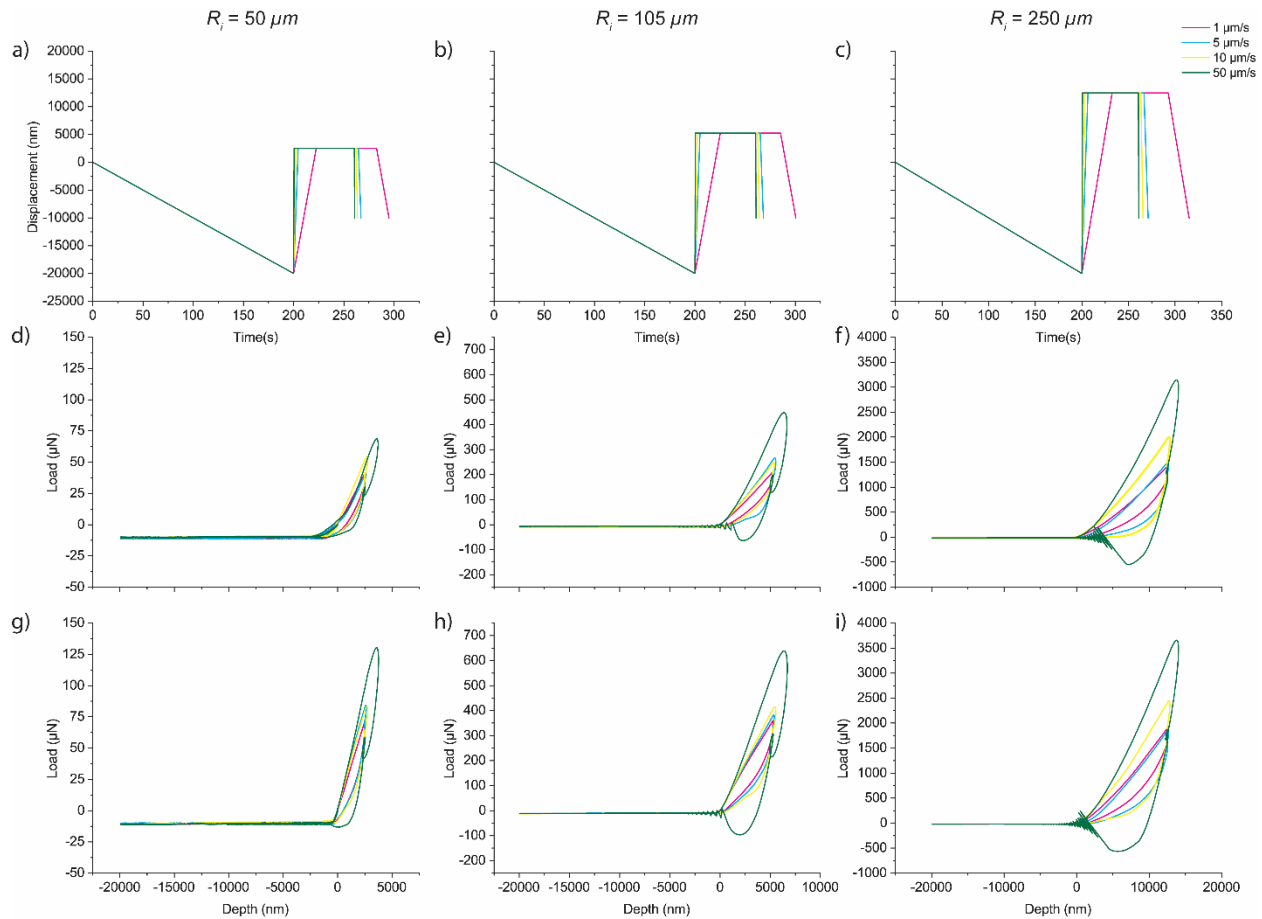


Figure 2. 2 Load Functions and Representative curves for 10 wt% Agarose. a) b) & c) Displacement-controlled load functions showing the different displacement rates used for each probe size (see column labels, legend). d) e) & f) Representative curves for indentations on the rough surface for each displacement rate and probe size. g) h) & i) Representative curves for indentations on the smooth surface for each displacement rate and probe size.

A row of three indents was performed for each combination of probe radius and displacement rate. Each row of indents was repeated at two additional locations on the sample

surface for 9 indents per probe radius/displacement rate combination and a total of 108 indents per sample. Indents were spaced at distances of approximately three times the contact radius, where the contact radius is defined as:

$$a = \sqrt{R_i \delta_{max}} \quad (1)$$

and δ_{max} is the peak displacement specified in the load function.

Each indent followed a displacement-controlled load function. First, the probe was brought into contact with the sample surface using a $20 \mu N$ preload to avoid false surface finds as a result of buoyancy or viscous drag on the probe during approach. The probe was then withdrawn vertically by $20 \mu m$ from the point of contact at $100 nm/s$ to allow time for full recovery of the material surface. Finally, the probe was displaced into the material at a specified displacement rate to a peak displacement, δ_{max} , of 5% of the probe radius relative to the original point of contact. This displacement was held for $t_h = 60 s$ before unloading at the specified displacement rate.

2.3.6 Microindentation analysis

From the load-displacement-time curves, three outcome measurands were determined: effective contact modulus, equilibrium modulus, and fluid load fraction. Taken together, these three measurands describe both the non-equilibrium and equilibrium behavior of a biphasic material^{2,23,24}. The effective contact modulus was determined using a fit of the linearized form of the equation for Hertz elastic contact. Displacement, δ , versus load to the two-thirds power, $P^{2/3}$, was plotted for the data during loading that corresponded to 25% to 75% of the maximum applied load. Isolating this portion of the curve excluded aberrant indentation behavior at

shallow depths (where surface roughness alters the relationship between displacement and contact area) and data at high indentation strains (above 5%). Data were fit using a linear regression:

$$\delta = mP^{2/3} + b \quad (2)$$

to determine the effective contact modulus from the slope, m , via:

$$E_C = \frac{3}{4} * \frac{\left(\frac{1}{m}\right)^{1.5}}{R^{0.5}} \quad (3)$$

as well as an effective displacement offset corresponding to the point of contact for an ideal surface, b .

The equilibrium modulus was determined from the hold portion of the curve. By fitting the load relaxation data (i.e., load vs. time) to a two-term Prony series, $P(t) = P_0 + P_1 \exp(-t/\tau_1) + P_2 \exp(-t/\tau_2)$, an equilibrium load was determined. Using the equilibrium load in the equation for Hertz elastic contact, in conjunction with the equilibrium displacement, δ_{C0} , defined as $\delta_{C0} = \delta_{max} - b$, an equilibrium modulus was determined from:

$$E_{C0} = \frac{\frac{3}{4}P_0}{R_i^{0.5} * \delta_{C0}^{1.5}} \quad (4)$$

Once the effective contact and equilibrium moduli were known, fluid load fraction was determined. Fluid load fraction represents the fraction of the applied load that is supported by interstitial fluid pressurization, and is defined as:

$$F' = \frac{E_C - E_0}{E_C} \quad (5)$$

2.3.7 Unconfined compression

Stress-relaxation testing was performed using a Mechanical Testing System (MTS Insight II; Eden Prairie, MN; 250 N load cell). Single cylindrical agarose samples ($n=3$ samples/concentration) were made to have a swollen 1:1 aspect ratio. Samples of three different diameters ($\phi = 8.66$ mm, 12 mm, and 16 mm) were used to evaluate instantaneous modulus, E_0 , and the equilibrium modulus, E_∞ , for 5, 7.5, and 10 wt. % agarose. Both moduli were obtained from the true stress-true strain curves to account for the change in cross-sectional area with compression. Gels were assumed to be incompressible (Poisson's ratio, $\nu = 0.5$).

Following a 30 mN pre-load, samples were tested in unconfined compression at a constant strain rate of 0.03 mm/s until a global 5% strain was achieved; the strain was held at 5% for $t_h=5$ hr until an equilibrium stress state was reached. Samples were fully submerged in a PBS solution during testing.

2.3.8 Statistical analysis

For 10 wt. % agarose, mixed model linear regression analyses were performed with the dependent variables as the effective contact modulus, equilibrium modulus, and fluid load fraction and independent variables as surface roughness (Rough vs. Smooth), probe radius, and displacement rate. Second and third-degree interactions between the three independent variables were included. To avoid multicollinearity, peak displacement was excluded from the analysis as $\delta_{max} = 0.05 * R_i$. Akaike information criteria (AIC) was used to select model terms. JMP Pro v15 (JMP, Cary, NC) was used for all statistical analyses.

Linear regression analyses of 5 wt. % and 7.5 wt. % agarose were performed nearly identically to 10 wt.% agarose with the exception of the inclusion of probe radius. These lower concentrations were tested using only the largest probe radius; thus probe radius was not included.

2.4.0 Results

2.4.1 Surface Roughness Measurements

Surface roughness measurements indicated two distinct surface profiles for each of the sectioning techniques used during sample preparation (Fig. 2.3) (Table 2.1). S_q of the rough surface was between 3.5 and 5.5 times greater than S_q for the smooth surface and increased with the dimensions of the sub-region used for analysis (Table 1). Similarly, mean peak to valley measurements of the rough surface were 3.3 to 3.6 times larger than peak to valley measurements of the smooth surface. The mean peak to valley distances also increased with the dimensions of the subregion of analysis. Consistent with the other measurands, the measured RMS peak spacing of the rough surface, $R_{\lambda q}$, was 2.5 times wider than $R_{\lambda q}$ of the smooth surface.

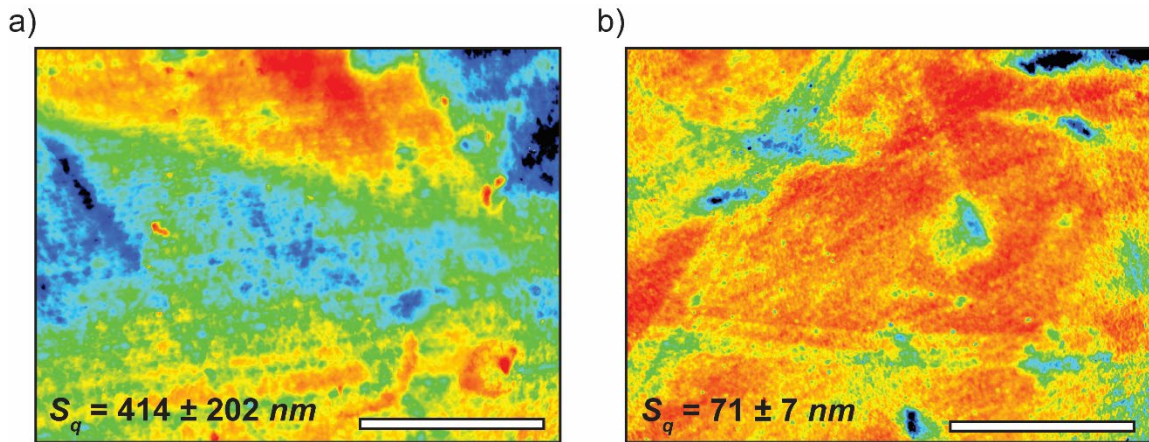


Figure 2.3 10 wt. % Agarose Surface Roughness measurements: a) Representative image of the rough surface b) Representative image of the smooth surface. Reported RMS surface roughness values are mean + standard deviation, evaluated over the full imaged area. Scale bars = 100 μm .

	Rough	Smooth
Analysis Dimensions		
$R_i = 50 \mu\text{m}$	$23 \mu\text{m} \times 23 \mu\text{m}$	$23 \mu\text{m} \times 23 \mu\text{m}$
$R_i = 105 \mu\text{m}$	$47 \mu\text{m} \times 47 \mu\text{m}$	$47 \mu\text{m} \times 47 \mu\text{m}$
$R_i = 250 \mu\text{m}$	$120 \mu\text{m} \times 120 \mu\text{m}$	$120 \mu\text{m} \times 120 \mu\text{m}$
Whole Image	$285.4 \mu\text{m} \times 214 \mu\text{m}$	$285.4 \mu\text{m} \times 214 \mu\text{m}$
RMS Roughness, S_q		
$R_i = 50 \mu\text{m}$	$112 \pm 60 \text{ nm}$	$32 \pm 10 \text{ nm}$
$R_i = 105 \mu\text{m}$	$167 \pm 61 \text{ nm}$	$43 \pm 15 \text{ nm}$
$R_i = 250 \mu\text{m}$	$357 \pm 199 \text{ nm}$	$64 \pm 15 \text{ nm}$
Whole Image	$414 \pm 202 \text{ nm}$	$71 \pm 7 \text{ nm}$
Peak to Valley, S_z		
$R_i = 50 \mu\text{m}$	$795 \pm 481 \text{ nm}$	$240 \pm 121 \text{ nm}$
$R_i = 105 \mu\text{m}$	$1297 \pm 666 \text{ nm}$	$359 \pm 164 \text{ nm}$
$R_i = 250 \mu\text{m}$	$2091 \pm 796 \text{ nm}$	$584 \pm 237 \text{ nm}$
Asperity Spacing, $R_{\lambda q}$		
	$39.122 \pm 18.509 \mu\text{m}$	$15.494 \pm 4.314 \mu\text{m}$

Table 2.1 Measured Surface Roughness Parameters of 10 wt. % agarose samples. All values reported as Mean \pm Standard Deviation

Surface roughness of the 5 wt. % and 7.5 wt. % agarose samples was assessed using the largest sub-region dimensions, in line with indentation testing, but demonstrated the same trends. For 5 wt. % agarose, S_q and $R_{\lambda q}$ of the rough surface ($S_q = 456 \text{ nm}$, $R_{\lambda q} = 51.244 \mu\text{m}$) were 2.67 times and 1.56 times larger than those measured on the smooth surface ($S_q = 171 \text{ nm}$, $R_{\lambda q}$

= 32.713 μm), respectively. The mean of the maximum peak to valley distances, S_z , of the rough surface was 1.65 times larger than the smooth surface ($S_z = 2471 \text{ nm}$ vs. $S_z = 1500 \text{ nm}$). For the 7.5 wt. % agarose, S_q and $R_{\lambda q}$ of the rough surface ($S_q = 281 \text{ nm}$, $R_{\lambda q} = 41.790 \mu\text{m}$) were 3.55 times and 2.16 times larger than those of the smooth surface ($S_q = 79 \text{ nm}$, $R_{\lambda q} = 19.303 \mu\text{m}$), respectively. The mean of the maximum peak to valley distances, S_z , of the rough surface was 2.36 times larger than the smooth surface ($S_z = 1490 \text{ nm}$ vs. $S_z = 631 \text{ nm}$).

2.4.2 Cryogenic FIB and SEM

Cryo-FIB/SEM measurements revealed distinctly different near-surface (0 - 5 μm in depth) morphologies for the rough and smooth 10 wt. % agarose surfaces. The near-surface region of the smooth surface was relatively flat, and asperities were well connected to the underlying network with small amplitudes (61 to 123 nm , peak to valley). In contrast, the near-surface region of the rough sample consisted of larger asperities with larger amplitudes (210 nm to 1.22 μm) and reduced connectivity to the underlying bulk material (Fig. 2.4). The observed amplitudes were consistent with surface roughness measurements performed using the laser confocal scanning microscope, but the connectivity of the asperities to the underlying network was only visible using cryo-FIB/SEM.

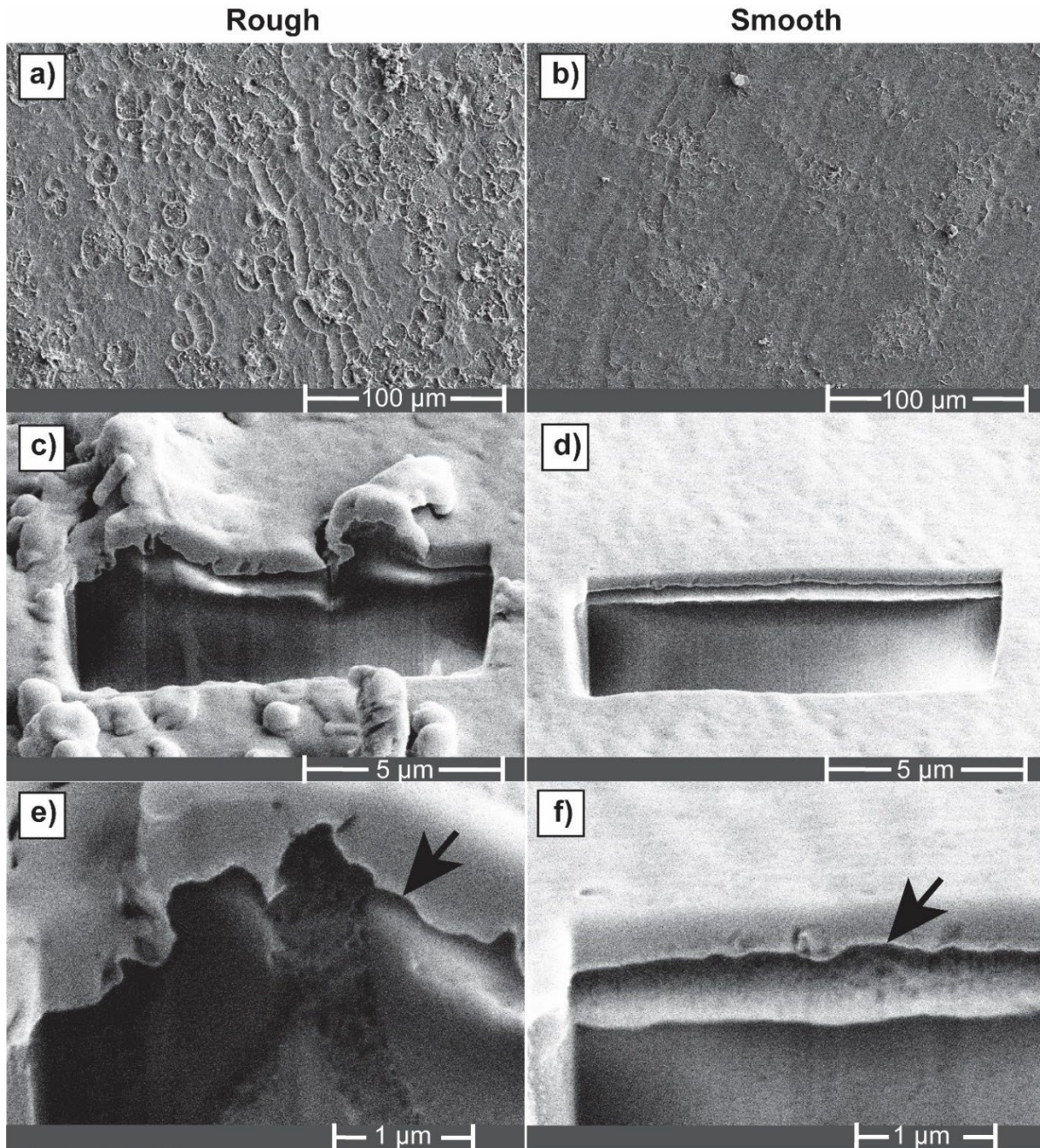


Figure 2. 4 Images from Cyro FIB & SEM of 10 wt. % agarose. a) & b) SEM Images of rough and smooth surfaces with Pt coating (Magnification: 500x). c) & d) SEM images showing FIB milling into rough and smooth surfaces (Magnification: 10000x) e) & f) Close up SEM cross-sectional images of asperities on Rough and Smooth surfaces. Black arrows indicate interface between Pt coating and underlying Agarose.

2.4.3 Unconfined compression testing

Unconfined compression under uniaxial loading was performed to determine an instantaneous and equilibrium modulus for each concentration utilized in this study. The

instantaneous modulus, E_0 , represents agarose's response to step-loading and increased with agarose concentration. The instantaneous measured moduli of 5 wt. %, 7.5 wt. %, and 10 wt. % agarose were 0.971 ± 0.037 MPa, 1.82 ± 0.075 MPa, and 2.41 ± 0.147 MPa, respectively. The measured equilibrium moduli of 5 wt. %, 7.5 wt. %, and 10 wt. % agarose were 0.383 ± 0.023 MPa, 0.726 ± 0.068 MPa, and 0.962 ± 0.141 MPa, respectively.

2.4.4 Microindentation testing

The effective contact moduli, E_c , and equilibrium moduli, E_{c0} , from microindentation tests on the rough 10 wt. % agarose surface were consistently less than the E_c and E_{c0} for tests on the smooth surface (Fig 2.5). Tests on the rough surface resulted in a mean effective contact modulus that was 51% lower than the smooth surface when using small probe radii and slow displacement rates (0.76 MPa vs. 1.55 MPa, averaged across all displacement rates) and 18% lower when using large probe radii and fast displacement rates (1.64 MPa vs. 2.00 MPa). Similarly, the mean equilibrium modulus of the rough surface was 47% lower than the smooth surface (0.62 MPa vs. 1.16 MPa) using small probe radii and 22% lower (1.17 MPa vs. 1.50 MPa) using large probe radii. In contrast to the measured moduli, fluid load fractions, F' , were comparable for the rough and smooth surfaces. F' of both surfaces increased consistently with probe radius and displacement rate. The fluid load fraction evaluated from tests performed on the rough and smooth surfaces ranged from 13.2% to 59.8% and from 14.3% to 54.7%, respectively (Fig. 2.5).

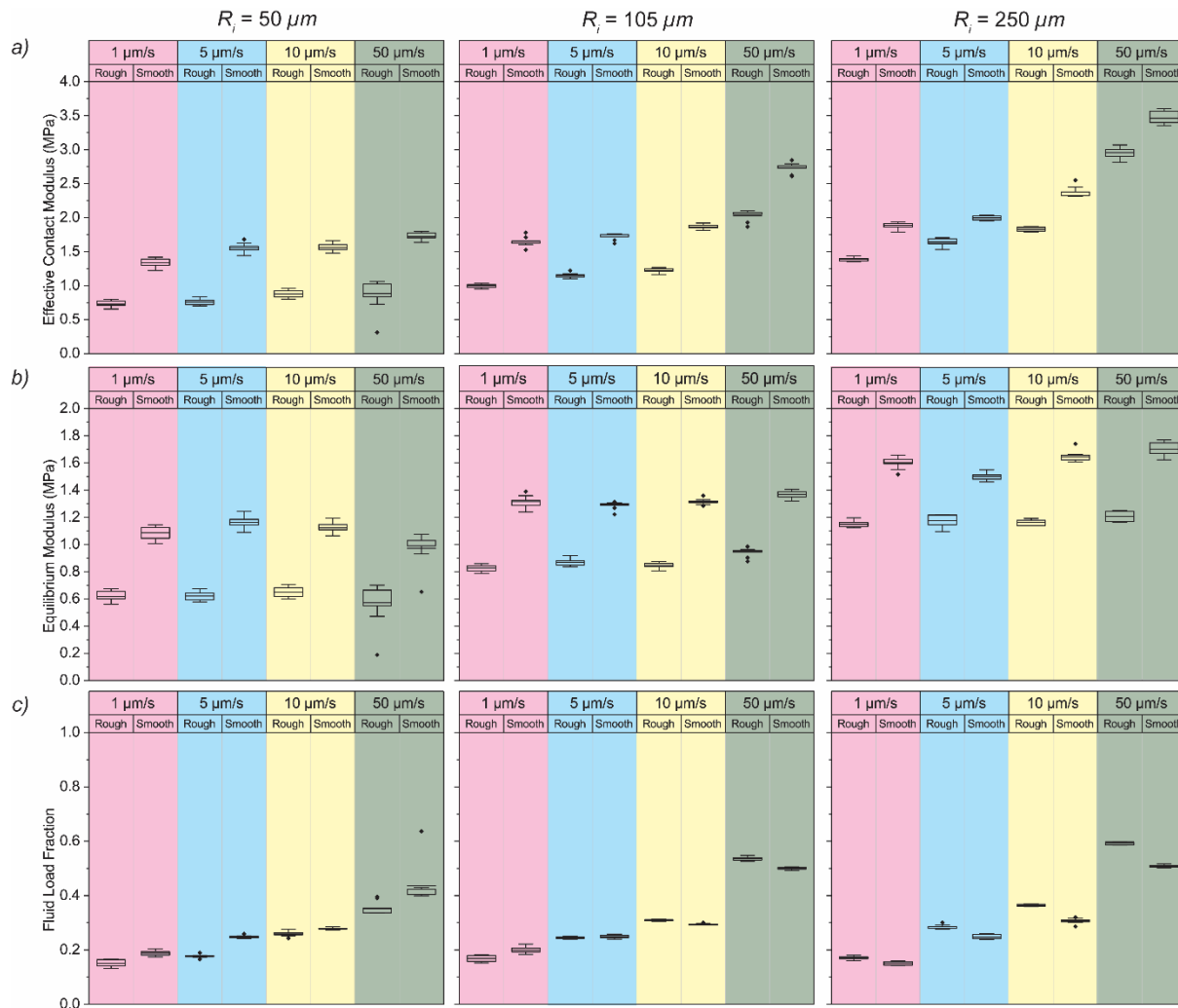


Figure 2.5 Measurands from Indentation testing of 10 wt% Agarose. Row a) Effective Contact modulus from indentation tests on Rough and Smooth surfaces. Row b) Equilibrium modulus from indentation tests on Rough and Smooth surfaces. Row c) Fluid Load Fraction from indentation tests on Rough and Smooth surfaces. Boxes represent lower and upper quartiles. Horizontal lines indicate means. Error bars indicate standard deviation. Individual points indicate outliers.

The effective contact moduli and equilibrium moduli of 5 and 7.5 wt. % agarose samples were substantially noisier than 10 wt. % agarose but showed similar trends. For 5 wt. % agarose, the mean effective contact moduli of the rough surface were 42.3% to 77.0% lower than the smooth surface (135 to 350 kPa vs. 550 to 800 kPa). Similarly, the mean equilibrium moduli of the rough surface were 41.5% to 76.7% lower than the smooth surface (117 to 273

kPa vs. 467 to 506 *kPa*). For 7.5 wt. % agarose, the mean effective contact moduli of the rough surface were 14.7% to 28.2% lower than the smooth surface (748 to 1311 *kPa* vs. 998 to 1562 *kPa*) and the mean equilibrium moduli of the rough surface were 11.8% to 24.2% lower than the smooth surface (673 to 802 *kPa* vs. 854 to 933 *kPa*). Fluid load fractions were similar for the rough and smooth samples of both 5 wt. % and 7.5 wt. % agarose (10.9 to 35.2% vs. 15.7 to 36.8% & 9.9 to 38.9% vs. 14.4 to 41.8%).

2.4.5 Statistical Analysis

For 10 wt. % agarose, linear regression analyses revealed a significant influence of surface roughness, probe radius, displacement rate on the effective contact modulus ($p < 0.05$). The presence of a rough surface reduced the effective contact modulus by a mean value of 301 *kPa* compared to a smooth surface. Similarly, the equilibrium modulus was significantly influenced by surface roughness and the probe radius ($p < 0.05$). However, the displacement rate had no effect. The presence of a rough surface led to a mean reduction in the equilibrium modulus of 222 *kPa* as compared to a smooth surface. Fluid load fraction was dependent on the probe radius and displacement rate ($p < .05$) but was not significantly influenced by surface roughness.

Linear regression analyses of 5 wt. % and 7.5 wt. % agarose were comparable to 10 wt. % agarose. Effective contact modulus was significantly influenced by surface roughness and displacement rate ($p < 0.05$), and the rough surface decreased the effective contact moduli of the 5 wt. % and 7.5 wt. % agarose by 205 *kPa* and 125 *kPa*, respectively. Equilibrium modulus was influenced by only the surface roughness ($p < 0.05$). The rough surface decreased the equilibrium modulus of the 5 wt. % and 7.5 wt. % agarose by 152.5 *kPa* and 81.5 *kPa*,

respectively. In contrast to 10 wt. % agarose, the fluid load fraction of the 5 wt. % and 7.5 wt. % were found to be significantly influenced by the surface roughness ($p < 0.05$).

2.5.0 Discussion

In the present study, we aimed to both elucidate how surface roughness of agarose gel samples influenced measured apparent indentation and equilibrium moduli and to describe how the influence of surface roughness affected fluid load support. Our results demonstrate that surface roughness significantly influences both the measured effective contact modulus (i.e., apparent indentation modulus) and equilibrium modulus. For every combination of agarose concentration, probe radius, and displacement rate used, the rougher surface resulted in reduced effective contact and equilibrium moduli. Furthermore, our results indicate that fluid load support remains relatively unaffected by surface roughness.

When evaluating the mechanical properties of hydrogel materials, a decrease in equilibrium modulus normally suggests that the solid matrix of one hydrogel is more compliant than the other. However, in the present study, both the rough and smooth sample of each agarose concentration were from the same batch of material, had the same sample radii, and nearly identical sample thicknesses. The only major difference between the evaluated samples was the surface roughness profile. Thus, the increased surface roughness must be solely responsible for the 22-47% reduction in measured equilibrium moduli of the rough 10 wt. % agarose sample.

Surface roughness leads to a decreased apparent stiffness when the mean asperity spacing is smaller than one half of the probe radius¹⁸. The mean asperity spacing is quantified

by measuring the mean wavelength, $R_{\lambda q}$, from a line profile of the surface roughness. The average wavelength of the 10 wt. % agarose rough surface is $39.12 \pm 18.51 \mu m$ as compared to $15.49 \pm 4.39 \mu m$ for the smooth surface. The probe radii used in the present study were $R_i = 50 \mu m$, $105 \mu m$, and $250 \mu m$. While the mean asperity spacing of the rough surface is above the limit identified by Chen and Diebels with respect to the $50 \mu m$ radius probe, we note that this limit was determined using finite element simulations of a simple surface roughness profile with regularly repeating asperities of identical height. Real surfaces are rarely periodic and typically consist of randomly distributed asperities of different shapes and sizes encountered on real surfaces.

In addition to the asperity spacing, the influence of surface depends on the indentation depth relative to measured surface roughness parameters. Some studies suggest that indents greater than 3 times the measured RMS surface roughness are sufficient^{17,18} while others indicate that the maximum indentation depth must be larger than the difference in height from the highest peak to the lowest valley encountered under contact¹⁶. The measured RMS roughness and peak to valley distance varied with the dimensions of the region of analysis. For this reason, the RMS surface roughness and peak to valley distances were evaluated using three different analysis region sizes, each corresponding to the contact diameter of the three probe radii at the prescribed maximum indentation depth. For the rough 10 wt. % agarose surface, the RMS surface roughness corresponding to $R_i = 50 \mu m$, $105 \mu m$, and $250 \mu m$ was $S_q = 112 \pm 60 nm$, $167 \pm 61 nm$, and $357 \pm 199 nm$, respectively. The mean peak to valley distances, S_z , corresponding to the same analysis region sizes were $795 \pm 481 nm$, $1297 \pm 666 nm$, and $2091 \pm 796 nm$. The maximum indentation depths in this study were $\delta_{max} = 2.5 \mu m$, $5.25 \mu m$, and 12.5

μm for $R_i = 50 \mu\text{m}$, $105 \mu\text{m}$, and $250 \mu\text{m}$, corresponding to 5% of the probe radius. In every case, the maximum indentation depth was more than 3 times the RMS surface roughness ($\delta_{\text{max}}/S_q = 22.3, 31.4, \& 35.0$ for $R_i = 50 \mu\text{m}, 105 \mu\text{m},$ and $250 \mu\text{m}$) and larger than the maximum peak to valley distance, yet the measured moduli of the rough surface were always smaller than the smooth surface. However, we found that δ_{max}/S_q increases with probe radius while the relative differences between the measured moduli of the rough and smooth surface decrease. The observed influence of surface roughness at depths far beyond the scale of the roughness profile of 10 wt. % agarose samples suggests the rough surface affects more than the relationship between probe displacement and contact area. We hypothesize that the local disruption of the agarose network acts as a near-surface region of decreased stiffness.

The influence of a near-surface region of decreased stiffness on properties measured via microindentation has recently been described using chemically cross-linked hydrogels with varying cross-link densities. Meier *et al.* prepared polyacrylamide (PAAm) gels in molds of different surface energies and roughness profiles, which resulted in gels with varying near-surface cross-link concentrations¹¹. Subsequent indentation of these gels revealed a variation of over 10-fold in the elastic modulus, corresponding to the different near-surface cross-link concentrations. Furthermore, the gels displayed distinctly different indentation behaviors, even when indented to several micrometers in depth. Similarly, Gombert *et al.* prepared PAAm gels using glass and PDMS molds, resulting in different near-surface cross-link concentrations¹². Indentation of the two different gels resulted in elastic moduli that varied by greater than 10-fold at indentation depths up to $6 \mu\text{m}$. In fact, the moduli of the two gels did not converge until approximately 20 micrometers of indentation depth. It is evident from these studies that the

near-surface cross-link concentration has a significant influence on the mechanical properties measured via indentation. While surface roughness is not equivalent to a near-surface variation in cross-link density, cryo-FIB/SEM measurements of the rough 10 wt. % agarose surface revealed a disrupted hydrogel network local to the surface of the rough sample.

To compare the results of the present study to the above referenced studies, we need to quantify the thickness of the region of reduced cross-link density. No prior studies, evaluated herein, of PAAAm gels with decreased cross-link density directly measured the thickness of the near-surface region. However, the thickness of this region on PAAm gels was evaluated in a separate study using indentation¹³. It was assumed that the layer thickness corresponded to the depth at which the modulus of the sample with decreased crosslink density converged with the modulus of the control sample. While indentation would appear to be a valid method of determining the layer thickness, we note that if the same analysis was performed here, our indentation data would suggest that the rough agarose surface extends beyond 12.5 μm into the agarose surface. The moduli of the rough and smooth agarose surfaces tested in this study never converged, even when indented using the largest probe size and indentation depth. If the thickness of the region of decreased cross-link density in the PAAm gels evaluated in these other studies was directly measured and found to be less than the thickness determined through indentation, it would support our hypothesis that the local disruption of the agarose network acts as a near-surface region of decreased stiffness. The combination of the altered relationship between probe displacement and contact area and a near-surface region of decreased stiffness may explain the persistence of the reduced modulus at depths far greater than the scale of surface roughness.

Our results motivate the use of finite element modeling to evaluate how surface roughness is influencing the apparent properties of biphasic materials. A finite element model, capable of simulating indentation of a rough biphasic surface with varying probe radii and indentation depths, would permit the decoupling of the effect of an altered contact area from other factors contributing to the observed indentation behavior (e.g., increased permeability, decreased stiffness local to the surface). Using this model, we could test the hypothesis that the altered contact area alone is insufficient to explain the apparent reduction in material properties at indentation depths beyond the scale of the surface roughness profile. Furthermore, such a model could be modified to understand how a near-surface region of decreased stiffness contributes to the indentation behavior of biphasic materials. Thus, expanding the impact of this work from surface roughness created through different sectioning techniques to other methods of modifying the surface characteristics of biphasic materials (e.g., varying cross-link density using different mold materials).

2.6.0 Conclusions

The goal of this study was to elucidate the influence of surface roughness on the moduli and fluid load support of hydrogel materials measured via microindentation. Indentation of rough and smooth agarose surfaces with varying probe radii and displacement rates demonstrated a considerable influence of surface roughness on the measured moduli and that decreases with increasing probe radius and indentation depth. This effect was particularly evident when comparing the equilibrium moduli of the rough and smooth surfaces. Using the smallest probe size and indentation depth, the equilibrium modulus of the rough 10 wt. %

agarose sample was reduced by 47% as compared to the smooth sample, whereas indentation using the largest probe radius and indentation depth reduced the equilibrium modulus of the rough surface by 22%. Our results differ from previous investigations into the influence of surface roughness of elastic materials, as the influence of surface roughness persists at indentation depths beyond the scale of the roughness profile. We hypothesize that this is due to the disruption of the agarose network observed in cryo-FIB/SEM measurements. These findings establish an improved understanding of the influence of surface roughness on the indentation behavior of soft, hydrated materials. The results of this work will aid in the design and optimization of novel hydrogels, including those used in tissue engineering applications.

2.7.0 Conflicts of Interest

The authors have no conflicts of interest to report

2.8.0 Author Contributions

Andrew A. Tomaschke - Conceptualization, Data curation, Formal analysis, Investigation, Methodology, Visualization, Writing -original draft, Writing – review & editing.

Victor Crespo-Cuevas - Data Curation, Formal analysis, Investigation, Writing – review and editing.

John Watt - Data Curation, Investigation, Methodology.

Frank DelRio - Conceptualization, Funding acquisition, Supervision, Writing – review & editing.

Virginia Ferguson – Conceptualization, Funding acquisition, Resources, Project administration, Supervision, Writing – review & editing.

2.9.0 References

- (1) Galli, M.; Comley, K. S. C.; Shean, T. A. V.; Oyen, M. L. Viscoelastic and Poroelastic Mechanical Characterization of Hydrated Gels. *Journal of Materials Research* **2009**, *24* (03), 973–979.
- (2) Moore, A. C.; Zimmerman, B. K.; Chen, X.; Lu, X. L.; Burris, D. L. Experimental Characterization of Biphasic Materials Using Rate-Controlled Hertzian Indentation. *Tribology International* **2015**, *89*, 2–8.
- (3) Mow, V. C.; Gibbs, M. C.; Lai, W. M.; Zhu, W. B.; Athanasiou, K. A. Biphasic Indentation of Articular Cartilage—II. A Numerical Algorithm and an Experimental Study. *Journal of Biomechanics* **1989**, *22* (8), 853–861.
- (4) Hu, Y.; Zhao, X.; Vlassak, J. J.; Suo, Z. Using Indentation to Characterize the Poroelasticity of Gels. *Applied Physics Letters* **2010**, *96* (12), 121904.
- (5) Oliver, W. C.; Pharr, G. M. Measurement of Hardness and Elastic Modulus by Instrumented Indentation: Advances in Understanding and Refinements to Methodology. *Journal of Materials Research* **2004**, *19* (1), 3–20.
- (6) Wahlquist, J. A.; DelRio, F. W.; Randolph, M. A.; Aziz, A. H.; Heveran, C. M.; Bryant, S. J.; Neu, C. P.; Ferguson, V. L. Indentation Mapping Revealed Poroelastic, but Not Viscoelastic, Properties Spanning Native Zonal Articular Cartilage. *Acta Biomaterialia* **2017**, *64*, 41–49.
- (7) Fischenich, K. M.; Wahlquist, J. A.; Wilmoth, R. L.; Cai, L.; Neu, C. P.; Ferguson, V. L. Human Articular Cartilage Is Orthotropic Where Microstructure, Micromechanics, and Chemistry Vary with Depth and Split-Line Orientation. *Osteoarthritis and Cartilage* **2020**, *28* (10), 1362–1372.
- (8) Bush, B. G.; Shapiro, J. M.; DelRio, F. W.; Cook, R. F.; Oyen, M. L. Mechanical Measurements of Heterogeneity and Length Scale Effects in PEG-Based Hydrogels. *Soft Matter* **2015**, *11* (36), 7191–7200.
- (9) Aisenbrey, E. A.; Tomaschke, A.; Kleinjan, E.; Muralidharan, A.; Pascual-Garrido, C.; McLeod, R. R.; Ferguson, V. L.; Bryant, S. J. A Stereolithography-Based 3D Printed Hybrid Scaffold for In Situ Cartilage Defect Repair. *Macromolecular Bioscience* **2018**, *18* (2), 1700267.
- (10) Schoonraad, S. A.; Fischenich, K. M.; Eckstein, K. N.; Crespo-Cuevas, V.; Savard, L. M.; Muralidharan, A.; Tomaschke, A. A.; Uzcategui, A. C.; Randolph, M. A.; McLeod, R. R.; Ferguson, V. L.; Bryant, S. J. Biomimetic and Mechanically Supportive 3D Printed Scaffolds for Cartilage and Osteochondral Tissue Engineering Using Photopolymers and Digital Light Processing. *Biofabrication* **2021**, *13* (4), 044106.

- (11) Meier, Y. A.; Zhang, K.; Spencer, N. D.; Simic, R. Linking Friction and Surface Properties of Hydrogels Molded Against Materials of Different Surface Energies. *Langmuir* **2019**, *35* (48), 15805–15812.
- (12) Gombert, Y.; Simič, R.; Roncoroni, F.; Dübner, M.; Geue, T.; Spencer, N. D. Structuring Hydrogel Surfaces for Tribology. *Advanced Materials Interfaces* **2019**, *6* (22), 1901320.
- (13) Johnson, C. L.; Dunn, A. C. Tribological Characterization of Gradient-Density Polyacrylamide Hydrogel Surfaces. *Exp Mech* **2021**, *61* (5), 829–842.
- (14) Ebenstein, D. M. Nano-JKR Force Curve Method Overcomes Challenges of Surface Detection and Adhesion for Nanoindentation of a Compliant Polymer in Air and Water. *Journal of Materials Research* **2011**, *26* (08), 1026–1035.
- (15) Greenwood, J. A.; Johnson, K. L.; Matsubara, E. A Surface Roughness Parameter in Hertz Contact. *Wear* **1984**, *100* (1), 47–57.
- (16) Wai, S. W.; Spinks, G. M.; Brown, H. R.; Swain, M. Surface Roughness: Its Implications and Inference with Regards to Ultra Microindentation Measurements of Polymer Mechanical Properties. *Polymer Testing* **2004**, *23* (5), 501–507.
- (17) Donnelly, E.; Baker, S. P.; Boskey, A. L.; van der Meulen, M. C. H. Effects of Surface Roughness and Maximum Load on the Mechanical Properties of Cancellous Bone Measured by Nanoindentation. *J Biomed Mater Res A* **2006**, *77* (2), 426–435.
- (18) Chen, Z.; Diebels, S. Modelling and Parameter Re-Identification of Nanoindentation of Soft Polymers Taking into Account Effects of Surface Roughness. *Computers & Mathematics with Applications* **2012**, *64* (9), 2775–2786.
- (19) Miller, M.; Bobko, C.; Vandamme, M.; Ulm, F.-J. Surface Roughness Criteria for Cement Paste Nanoindentation. *Cement and Concrete Research* **2008**, *38* (4), 467–476.
- (20) Oyen, M. L. Mechanical Characterisation of Hydrogel Materials. *International Materials Reviews* **2014**, *59* (1), 44–59.
- (21) Oyen, M. L.; Shean, T. A. V.; Strange, D. G. T.; Galli, M. Size Effects in Indentation of Hydrated Biological Tissues. *Journal of Materials Research* **2012**, *27* (1), 245–255.
- (22) Normand, V.; Lootens, D. L.; Amici, E.; Plucknett, K. P.; Aymard, P. New Insight into Agarose Gel Mechanical Properties. *Biomacromolecules* **2000**, *1* (4), 730–738.
- (23) Bonnevie, E. D.; Baro, V. J.; Wang, L.; Burriss, D. L. Fluid Load Support during Localized Indentation of Cartilage with a Spherical Probe. *Journal of Biomechanics* **2012**, *45* (6), 1036–1041.

- (24) Moore, A. C.; Burris, D. L. Tribological and Material Properties for Cartilage of and throughout the Bovine Stifle: Support for the Altered Joint Kinematics Hypothesis of Osteoarthritis. *Osteoarthritis and Cartilage* **2015**, *23* (1), 161–169.

CHAPTER 3

The Influence of Surface Roughness on the Microscale Indentation Behavior of Porcine Articular Cartilage

3.1.0 Abstract

Surface roughness is known to affect the resulting properties from small-scale indentation testing. In the present study, the influence of surface roughness on microindentation property assessments was evaluated via depth-sensing and AFM-based indentation of rough and smooth porcine articular cartilage surfaces. A wide range of probe sizes and displacement rates was used to evaluate the influence of surface roughness on both the equilibrium and non-equilibrium properties of the tissue. Rough and smooth surfaces were generated using two different cutting techniques which produced two distinctly different surface profiles ($S_q = 1885 \pm 361 \text{ nm}$ versus $571 \pm 200 \text{ nm}$). Surface roughness affected both the equilibrium and non-equilibrium behavior, reducing the effective contact and equilibrium moduli from indentation tests on the rough surface by more than ~70% as compared to the smooth surface. Additionally, the influence of surface roughness decreased with increasing probe size and indentation depth, suggesting surface roughness acts as a near-surface region of decreased stiffness. While AFM-based indentation tests were able to resolve differences between the effective contact moduli of the rough and smooth surfaces using larger probes,

the properties of the two surfaces were nearly indistinguishable using the smallest probe size. The results suggest that the shallow indentation depths used in AFM-based microindentation are evaluating the properties of the near-surface region of decreased stiffness, not the bulk properties of the tissue.

3.2.0 Introduction

Microindentation has become an essential technique in the evaluation of the biomechanical properties of articular cartilage. This technique is non-destructive in nature¹, allows assessment across various length scales using different probe sizes¹⁻³, and is capable of characterizing the non-linear biphasic mechanical behavior of articular cartilage with minimal sample preparation^{4,5}. Microindentation tests performed on intact cartilage tissue are used to assess the health of the tissue and understand how osteoarthritis influences mechanical behavior^{6,7}. Alternatively, tissue can be excised to permit the assessment of property variation as a function of depth^{8,9}. While the utility of this technique is evident, indentation is highly surface sensitive and requires an assumption of a well-defined relationship between the measured probe displacement and the area of the probe in contact with the material^{10,11}. Surface characteristics affecting this relationship thus result in the underestimation or overestimation of mechanical properties.

Surface roughness alters the actual area of the probe in contact during initial contact^{12,13} which violates the assumption of a well-defined relationship between probe displacement and contact area. When the spacing of peaks and valleys on a rough surface exceeds the size of the indentation probe, the measured properties depend on the testing location relative to the

topography of the surface^{13,14}. Contact between the probe and a peak (typically referred to as an asperity) leads to an overestimation of the area in contact and an underestimation of material properties, whereas contact inside a valley (the space between asperities) leads to an underestimation of the area in contact and an overestimation of material properties. When the asperity spacing is small relative to the probe size, the actual area in contact is overestimated leading to a consistent underestimation of the measured material properties^{12,13,15}. Surface roughness is always present during the indentation testing of articular cartilage. In the case of intact specimens, surface roughness takes the form of the intrinsic roughness of healthy tissue or a fibrillated surface as a result of wear and tear and the progression of osteoarthritis¹⁶⁻¹⁸. In excised samples, surface roughness is created by the technique used to section the tissue for testing^{19,20}. Yet, the influence of surface roughness is routinely ignored during microindentation testing of articular cartilage. It remains unclear whether the indentation of articular cartilage, a non-linear biphasic, soft, hydrated tissue is influenced by surface roughness to the same extent as the stiff, elastic-plastic materials used in other investigations.

The primary objective of this study is to determine whether surface roughness has a significant influence on the measurands being assessed via indentation. The secondary objective is to examine how the influence of surface roughness varies with controllable experimental parameters, namely probe size and displacement rate. These objectives are achieved through AFM and depth-sensing microindentation of rough and smooth articular cartilage samples. With the knowledge gained through the experiments in this study, we will: 1) enhance our understanding of the influence of surface roughness on the indentation of soft, hydrated materials, 2) critically evaluate AFM as a tool for evaluating the mechanical properties

of soft, hydrated materials in the presence of surface roughness, and 3) provide context to the measured properties across previous indentation-based investigations of articular cartilage.

3.3.0 Materials and Methods

3.3.1 Sample preparation

Full thickness osteochondral samples were harvested from the posterior region of the lateral femoral condyle of a Yorkshire pig (age: 3 months, sex: female). During the harvesting process, 3 *mm* wide, longitudinal sections of the lateral femoral condyle were obtained using a diamond wafering blade. A razor blade was then used to harvest two full-thickness osteochondral samples from adjacent locations in the posterior region where the cartilage was thickest.

3.3.2 Preparation of rough and smooth surfaces

Samples were oriented such that the full osteochondral thickness was the testing surface for indentation. One of the samples cut with the diamond wafering blade, was set aside to serve as the rough sample. The other sample was further sectioned using a vibratome. The vibratome stage was stepped downwards in 100 μm increments until a full thickness slice was obtained. Then, 5 additional cuts were made in 20 μm increments, leaving the remaining ~ 2.8 *mm* thick section to serve as the smooth sample (Fig. 3.1). Samples were loosely wrapped in gauze, dampened with phosphate-buffered saline (PBS, pH 7.4), and stored at -70 °C in separate sealed containers until analysis.

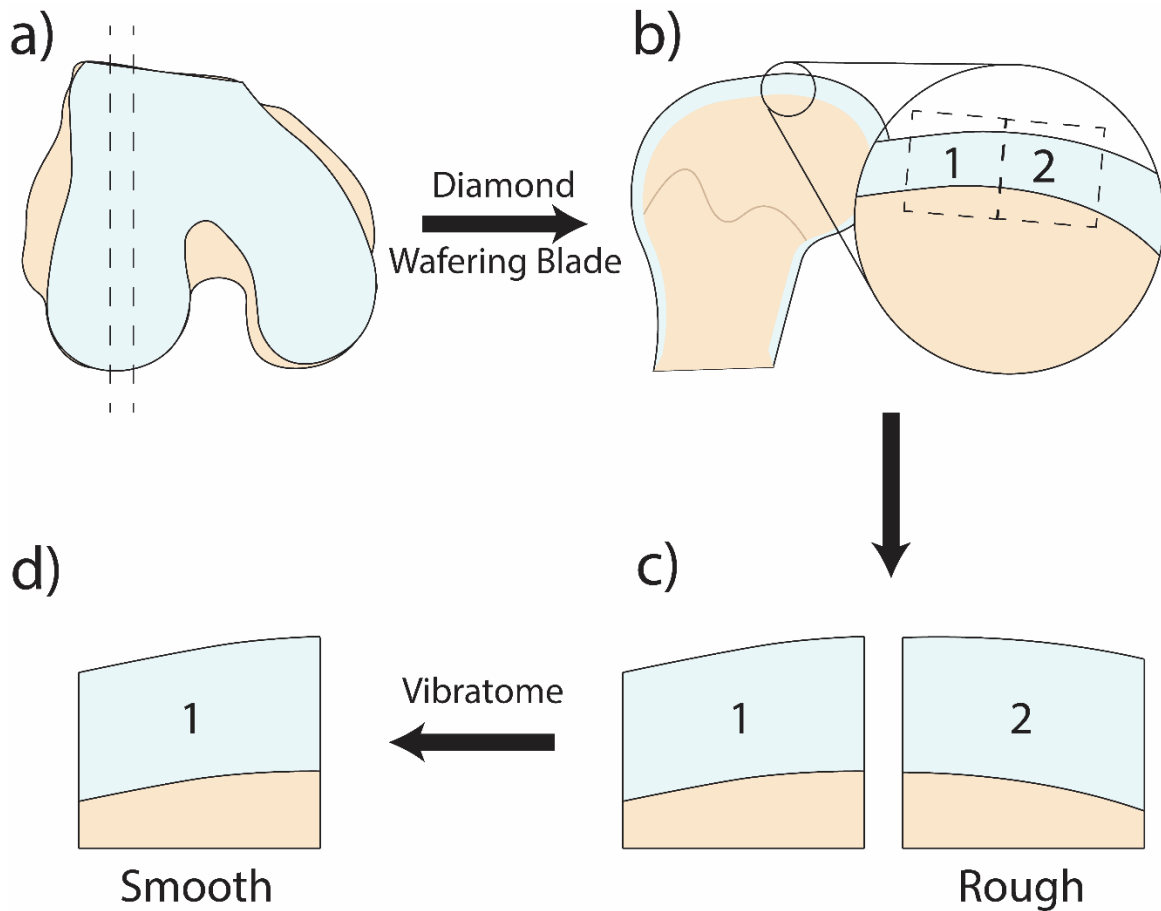


Figure 3. 1 Sample harvesting and preparation of rough and smooth surfaces. **a)** A 3mm section was excised from the lateral femoral condyle using a diamond wafering blade **b)** Two cross-sectional cartilage samples were collected from the posterior region **c)** One sample set aside to serve as the rough sample **d)** The other sample was further sectioned on a vibratome to produce the smooth surface

3.3.3 Surface Roughness Measurements

To verify that the methods of sample preparation produced the desired surface roughness profiles, rough and smooth samples were evaluated using a Keyence VK-X1000 confocal laser scanning microscope with a 50× objective (Keyence Corporation of America, Itasca, IL). For each sample, three representative areas were profiled. Surface roughness parameters vary with the size of the area evaluated. Care was taken to image the three locations in quick succession to avoid dehydration of the material surface. The surface roughness profile of each sample was characterized using three different parameters: the root

mean square height, S_q , the height difference between the highest peak and deepest valley under contact, referred to here as peak to valley, and the mean asperity spacing, $R_{\lambda q}$. S_q was evaluated over five different sized sub-regions corresponding to the dimensions of contact for the different probes used during testing, repeated at nine locations inside of each representative area. Peak to valley was similarly evaluated using five different sized sub-regions. A custom Matlab (MathWorks, USA.) script was used to slide the location of the sub-region around within each representative area, which allowed assessment of the full area. Lastly, the mean asperity spacing of each representative area was assessed from line profiles oriented both horizontally and vertically to the image. The asperity spacing in each direction was averaged to determine a mean asperity spacing for each representative area.

3.3.4 Depth-sensing microindentation measurements

Depth-sensing indentation measurements were performed using a TI-950 Triboindenter (Bruker, Eden Prairie, MN) with an XZ500 extended displacement stage in displacement control. Three probe radii ($R_i = 50, 105, \text{ and } 250 \mu\text{m}$) and four displacement rates ($\dot{\delta} = 1, 5, 10, \text{ and } 50 \mu\text{m/s}$) were used to indent the Rough and Smooth samples. Prior to testing, samples were allowed to equilibrate while submerged in a solution of 99 wt% 0.01 M PBS and 1 wt% protease inhibitor for 2 hrs. Samples remained submerged in the solution throughout the course of testing to prevent dehydration and limit tissue degradation.

A row of four indents was performed for each combination of probe radius and displacement rate. Each row of indents was repeated at two additional locations on the sample surface for 12 indents per probe radius/displacement rate combination. Indents were spaced at

distances of approximately three times the contact radius, where the contact radius is defined as:

$$a = \sqrt{R_i \delta_{max}} \quad (1)$$

and δ_{max} is the peak displacement specified in the load function.

Each indent followed a displacement-controlled load function. First, the probe was brought into contact with the sample surface using a 20 μN preload to avoid false surface finds as a result of buoyancy or viscous drag on the probe during approach. The probe was then withdrawn vertically from the point of contact at 100 nm/s to a height sufficient to bring the probe out of contact (20 to 40 μm) and allow time for full recovery of the material surface. Finally, the probe was displaced into the material at a specified displacement rate to a peak displacement, δ_{max} , of 5% of the probe radius relative to the original point of contact. This displacement was held for 120 seconds before unloading at the specified displacement rate (Fig. 3.2).

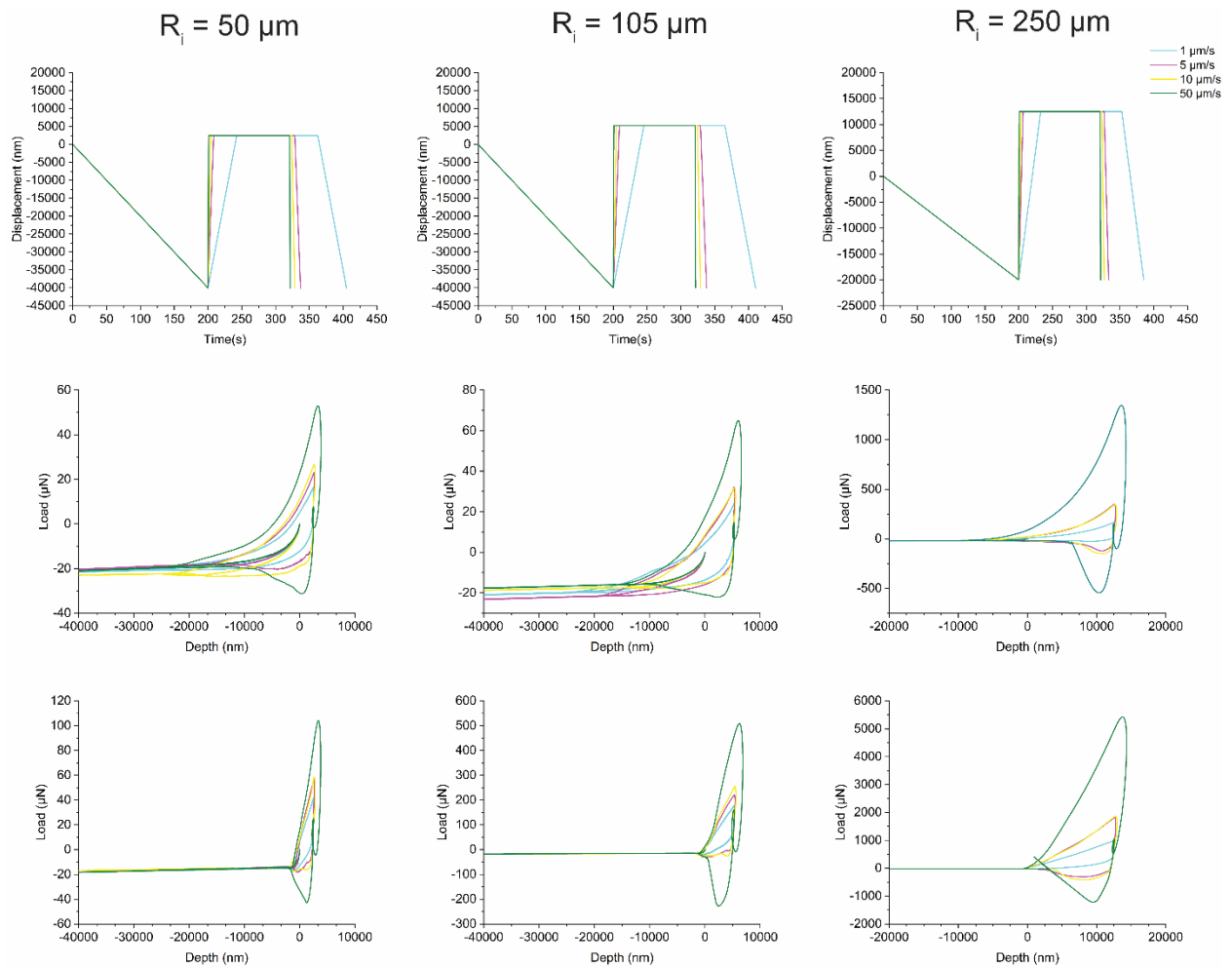


Figure 3. 2 Depth-sensing Microindentation Load Functions and Representative Curves. Top Row: Load Functions Middle Row: Representative Curves from the Rough Surface Bottom Row: Representative Curves from the Smooth Surface

3.3.5 AFM-based microindentation measurements

AFM indentation measurements were performed with a Keysight 5500 AFM system (Keysight Technologies). A cantilever with a spherical tip ($2 \mu\text{m}$ diameter borosilicate sphere, NovaScan, pre-calibrated $k_c = 0.36 \text{ N/m}$) and a tipless cantilever (MikroMasch, nominal spring constant $k_c = 16 \text{ N/m}$) were used, respectively. Tipless cantilevers were modified by gluing a $25 \mu\text{m}$ diameter borosilicate glass bead (microParticles GmbH, Germany) to the tip of the cantilever via ultraviolet curing glue (ultraviolet curing, Loctite). A cantilever spring constant was then determined using the thermal fluctuation method implemented in the AFM software

(PicoView v1.14)²¹. The deflection sensitivity of the cantilever, D_{sens} , was determined by indentation of a glass substrate and held constant to perform all measurements with each single probe in the same day. A needle was mounted adjacent to the cartilage sample with paraffin wax to indicate the middle zone axis for mechanical testing. A CCD camera within the AFM system was used to align and monitor the position of the cantilever over defined regions of the articular cartilage surface. Raster scans of force-distance curves were performed on each sample across four $80 \times 80 \mu m$ regions, spaced at least $1 mm$ apart, spanning the middle zone. At each of the four regions, indentation speeds were randomly varied between 1, 5, 10, and $23.333 \mu m/s$, spanning much of the range of our hardware capabilities (Fig. 3.3). Taking the relative size of the spherical indenter into account, the applied maximum force voltage was chosen to probe the tissue stiffness on a cellular length-scale while also adhering to small strain conditions²².

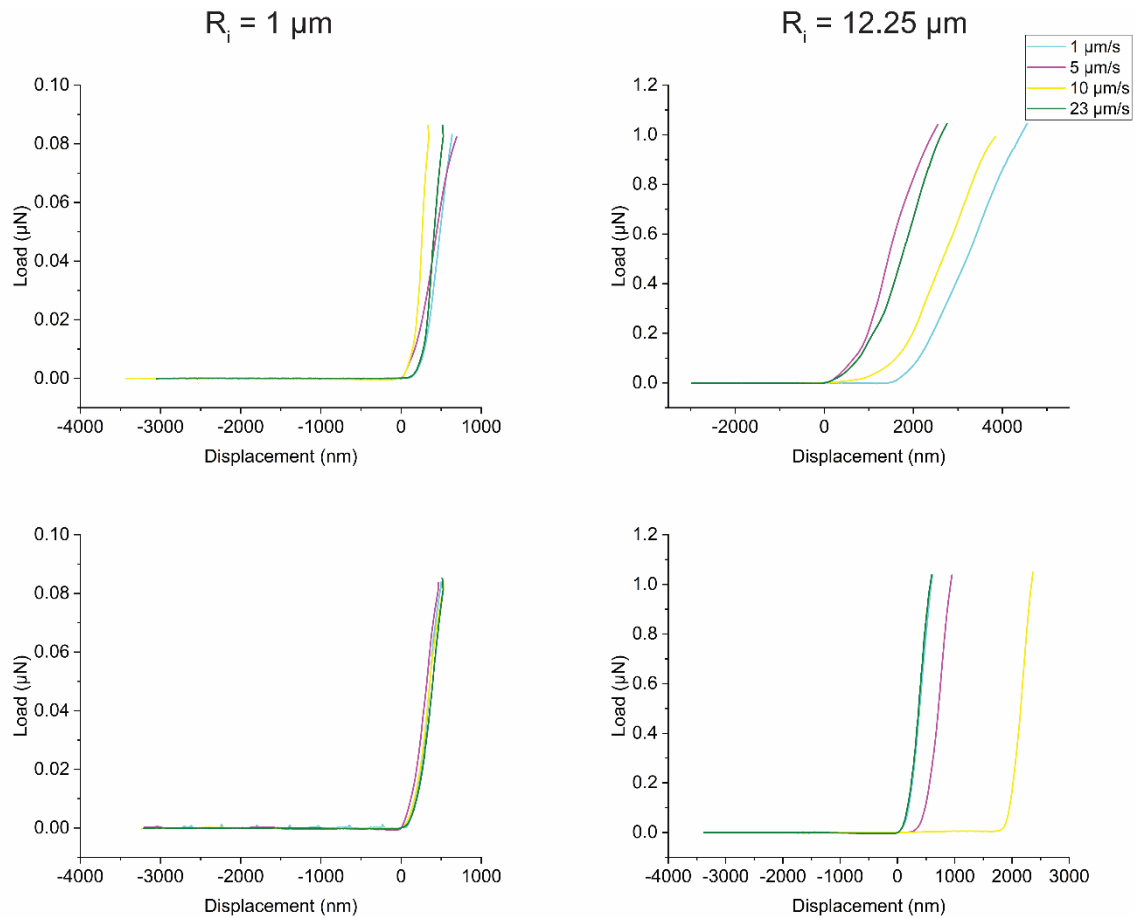


Figure 3.3 Representative Curves from AFM-based microindentation Top Row: Rough Surfaces Bottom Row: Smooth Surfaces

3.3.6 Depth-sensing Microindentation Analysis

From the load-displacement-time indentation curves, three outcome measurands were determined: effective contact modulus, equilibrium modulus, and fluid load fraction. The effective contact modulus was determined using a fit of the linearized form of the equation for Hertz elastic contact. Displacement, δ , versus load to the two-thirds power, $P^{2/3}$, was plotted for the data during loading that corresponded to 25% to 75% of the maximum applied load. Isolating this portion of the curve excluded aberrant indentation behavior at shallow depths (where surface roughness alters the relationship between displacement and contact area) and data at high indentation strains (above 5%). Data were fit using a linear regression:

$$\delta = mP^{2/3} + b \quad (1)$$

to determine the effective contact modulus from the slope (m) via:

$$E_C = \frac{3}{4} * \frac{\left(\frac{1}{m}\right)^{1.5}}{R^{0.5}} \quad (2)$$

as well as an effective displacement offset corresponding to the point of contact for an ideal surface, (b).

The equilibrium modulus was determined from the hold portion of the curve. By fitting the load relaxation data (i.e., load vs. time) to a two-term Prony series ($P(t) = P_0 + P_1 \exp(-t/\tau_1) + P_2 \exp(-t/\tau_2)$), an equilibrium load was determined²³. Using the equilibrium load in the equation for Hertz elastic contact, in conjunction with the equilibrium displacement, δ_{C0} , defined as $\delta_{C0} = \delta_{max} - b$, an equilibrium modulus was determined from:

$$E_{C0} = \frac{\frac{3}{4}P_0}{R_i^{0.5} * \delta_{C0}^{1.5}} \quad (4)$$

Once the effective contact and equilibrium moduli were known, fluid load fraction was determined. Fluid load fraction represents the fraction of the applied load that is supported by interstitial fluid pressurization, and is defined as:

$$F' = \frac{E_C - E_0}{E_C} \quad (5)$$

3.3.7 AFM-based Microindentation Analysis

Load voltage, V_L , and Piezo Displacement, δ_{piezo} data from the AFM-based microindentation measurements were converted to Load, P , and Probe Displacement, δ , using:

$$P = V_L * D_{sens} * k_c \quad (6)$$

and:

$$\delta = \delta_{piezo} - P/k_c \quad (7)$$

Once the data was in the proper format, effective contact modulus was evaluated using the same procedure as for the depth-sensing microindentation measurements.

3.3.8 Statistical Analysis

Statistical Analysis for the depth-sensing microindentation and AFM-based indentation outcomes were evaluated separately. Mixed model linear regression analyses were performed with the dependent variables as the effective contact modulus, equilibrium modulus, and fluid load fraction and independent variables as surface roughness (rough vs. smooth), probe radius, and displacement rate. To avoid multicollinearity, peak displacement was excluded from the analysis as $\delta_{max} = 0.05 * R_i$. JMP Pro v15 was used for all statistical analyses. Akaike information criteria (AIC) was used to select model terms.

3.4.0 Results

3.4.1 Surface Roughness Measurements

The root mean square height, S_q , of the rough cartilage surface ($S_q = 288 \pm 236$ nm to 1874 ± 406 nm) was 2.7 to 3.5-fold larger than the smooth surface ($S_q = 108 \pm 145$ nm to 530 ± 188 nm) and the measured roughness of both surfaces increased with the dimensions of the sub-region (Fig. 3.4, Table 3.1). Peak to valley, S_z , measurements followed a similar pattern, the mean peak to valley distance of the rough surface ($S_z = 1079 \pm 691$ nm to 10376 ± 2300 nm) was 2.4 to 2.8-fold larger than the smooth surface ($S_z = 446 \pm 508$ nm to 3667 ± 953 nm) and

increased with the dimensions of the sub-region. Lastly, the mean asperity spacing of the rough surface ($R_{\lambda q} = 63.0 \pm 17.4 \mu\text{m}$) was 1.9-fold larger than the smooth surface ($R_{\lambda q} = 33.6 \pm 9.4 \mu\text{m}$).

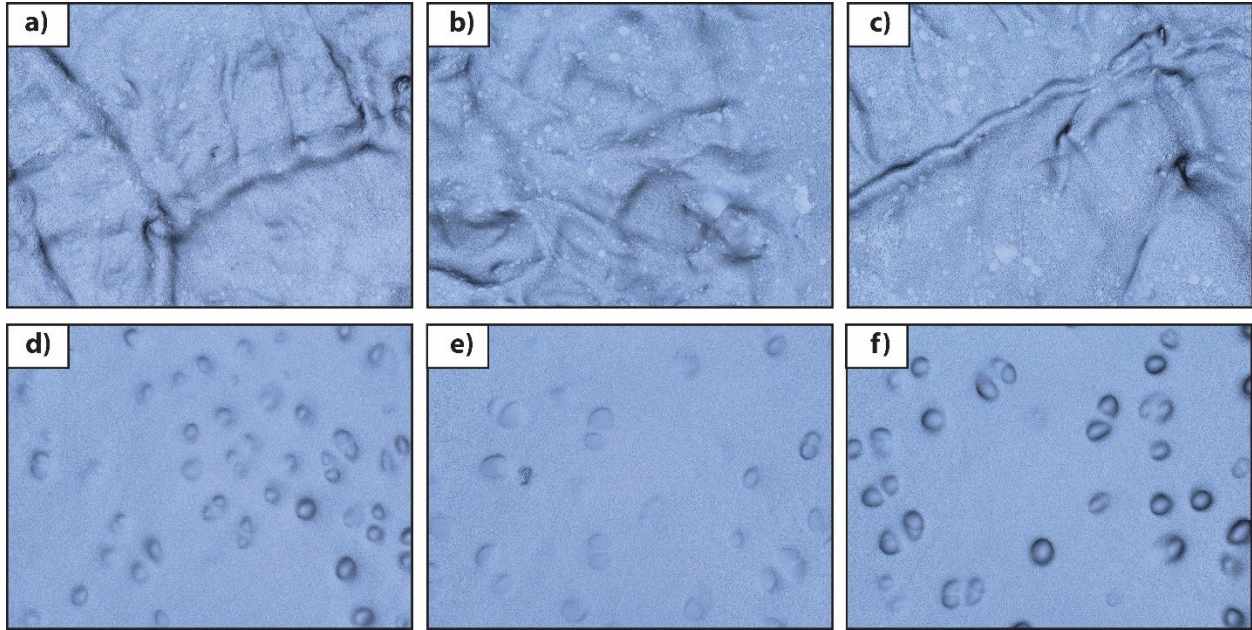


Figure 3. 4 Representative Areas Used in Surface Roughness Measurements a-c: Rough Surfaces d-f: Smooth Surfaces

Notably, S_q and S_z were not measured for sub-regions corresponding to the dimensions of contact for the $1 \mu\text{m}$ radius probe. The dimensions of contact for this probe size ($0.447 \mu\text{m}$) were comparable to the lateral resolution of the confocal laser scanning microscope ($0.279 \mu\text{m}$). Evaluations of surface roughness parameters using such small sub-regions would likely not be representative of the surface in contact and were therefore omitted.

	Rough	Smooth
Analysis Area		
$R_i = 12.25 \mu m$	$6 \mu m \times 6 \mu m$	$6 \mu m \times 6 \mu m$
$R_i = 50 \mu m$	$23 \mu m \times 23 \mu m$	$23 \mu m \times 23 \mu m$
$R_i = 105 \mu m$	$47 \mu m \times 47 \mu m$	$47 \mu m \times 47 \mu m$
$R_i = 250 \mu m$	$120 \mu m \times 120 \mu m$	$120 \mu m \times 120 \mu m$
<i>Whole Area</i>	$285.4 \mu m \times 214 \mu m$	$285.4 \mu m \times 214 \mu m$
RMS Roughness, S_q		
$R_i = 12.25 \mu m$	$288 \pm 236 \text{ nm}$	$108 \pm 145 \text{ nm}$
$R_i = 50 \mu m$	$882 \pm 456 \text{ nm}$	$329 \pm 350 \text{ nm}$
$R_i = 105 \mu m$	$1452 \pm 625 \text{ nm}$	$446 \pm 258 \text{ nm}$
$R_i = 250 \mu m$	$1874 \pm 406 \text{ nm}$	$530 \pm 188 \text{ nm}$
<i>Whole Area</i>	$1885 \pm 361 \text{ nm}$	$571 \pm 200 \text{ nm}$
Peak to Valley, S_z		
$R_i = 12.25 \mu m$	$1079 \pm 691 \text{ nm}$	$446 \pm 508 \text{ nm}$
$R_i = 50 \mu m$	$3832 \pm 1885 \text{ nm}$	$1491 \pm 1056 \text{ nm}$
$R_i = 105 \mu m$	$6529 \pm 2421 \text{ nm}$	$2527 \pm 1128 \text{ nm}$
$R_i = 250 \mu m$	$10376 \pm 2300 \text{ nm}$	$3667 \pm 953 \text{ nm}$
Asperity Spacing, $R_{\lambda q}$	$62.973 \pm 17.449 \mu m$	$33.644 \pm 9.384 \mu m$

Table 3. 1 Measured Surface Roughness Parameters. All values reported as Mean \pm Standard Deviation

3.4.2 Depth-sensing Microindentation

Depth-sensing microindentation measurements on the rough surface resulted in reduced effective contact moduli when compared to measurements made on the smooth surface across all combinations of probe radius and displacement rate (Fig. 3.5). Measurements made on the rough surface with the $50 \mu m$ radius probe reduced effective contact moduli by a mean of 80% when compared to measurements made on the smooth surface. The effective contact modulus was reduced by 95% for measurements on the rough surface as compared to the smooth surface when using the $105 \mu m$ radius probe. Lastly, measurements performed on the rough surface with the $250 \mu m$ radius probe reduced the effective contact modulus by 75% as compared to measurements made on the smooth surface.

Similar to the results for the effective contact modulus, measurements made on the rough surface resulted in reduced equilibrium moduli across all combinations of probe radius and displacement rate (Fig. 3.5). Measurements made on the rough surface reduced the equilibrium modulus as compared to measurements made on the smooth surface by 80%, 94%, and 82% for probe radii of 50 μm , 105 μm , and 250 μm , respectively.

Measurements made on the rough surface did not consistently increase or reduce the fluid load fraction as compared to measurements made on the smooth surface (Fig. 3.5). For the 50 μm radius probe, tests on the rough surface resulted in a mean reduction of the fluid load fraction of 0.34%. For the 105 μm radius probe, the rough surface was associated with a 17% reduction in the fluid load fraction. Lastly, tests made on the rough surface with the 250 μm radius probe resulted in a 11% increase in fluid load fraction as compared to tests made on the smooth surface.

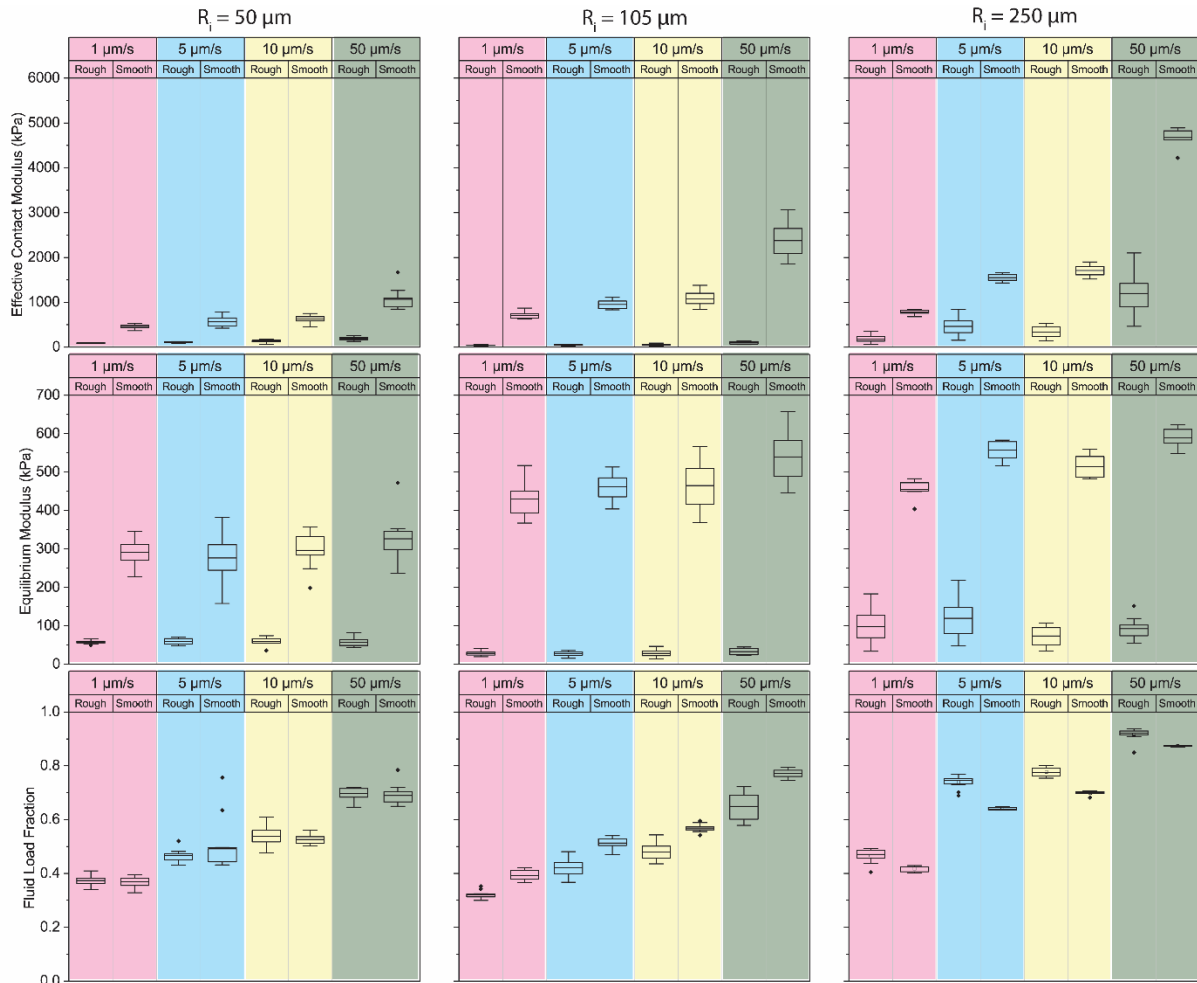


Figure 3. 5 Depth-Sensing Microindentation Results Top Row: Effective Contact Modulus Middle Row: Equilibrium Modulus Bottom Row: Fluid Load Fraction

3.4.3 AFM-based Microindentation

AFM-based indentation measurements performed on the rough surface resulted in a mean reduction of the effective contact modulus across both probe sizes and all four displacement rates. Measurements made on the rough surface reduced the effective contact modulus as compared to measurements on the smooth surface by 21% and 91% for the 1 μm and 12 μm radius probes, respectively (Fig. 3.6).

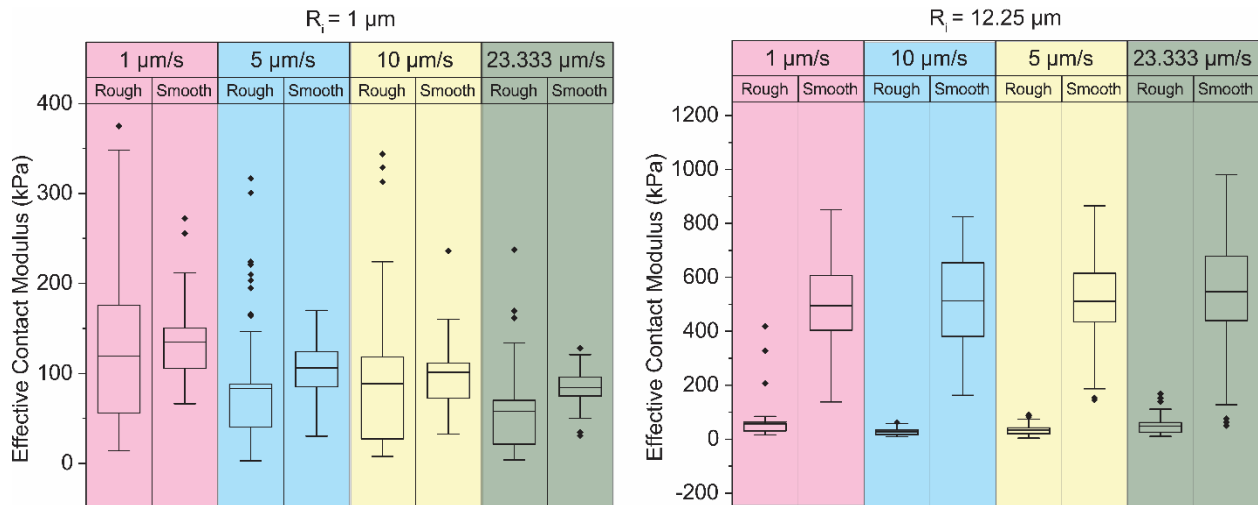


Figure 3. 6 AFM-Based Microindentation Results Left: 1 μm Radius Probe Right: 12.25 μm Radius Probe

3.4.4 Statistical Analyses

For the depth-sensing microindentation measurements, mixed model linear regression analyses revealed a significant influence of surface roughness, probe radius, and displacement rate on the effective contact modulus ($p < 0.05$). The rough surface reduced the effective contact modulus by a mean value of 552 kPa . Similarly, surface roughness, probe radius, and displacement rate significantly influenced the measured equilibrium modulus ($p < 0.05$). The rough surface reduced the equilibrium modulus by a mean value of 185 kPa . The measured fluid load fraction was significantly influenced by probe radius and displacement rate ($p < 0.05$) whereas the influence of surface roughness was found to be statistically insignificant ($p > 0.05$).

For the AFM-based microindentation measurements, linear regression analyses revealed a significant influence of surface roughness and probe radius on the effective contact modulus ($p < 0.05$). The rough surface was associated with a 130 kPa mean reduction in the effective contact modulus.

3.5.0 Discussion

Depth-sensing and AFM-based microindentation assessments of rough and smooth porcine articular cartilage surfaces demonstrate that surface roughness directly influences the measured mechanical properties. We found that a 2-3 fold increase in surface roughness reduced the measured effective contact modulus and equilibrium modulus by more than 70% when compared to a smoother surface. Furthermore, we determined that the influence of surface roughness on the measured properties increases with decreasing probe size but is not affected by the rate of indentation. Increasing probe size from a 1 μm radius to a 250 μm radius increases the mean effective contact modulus of the rough and smooth surfaces from 87 to 543 kPa and 103 to 2178 kPa, respectively. Similarly, the equilibrium moduli of the rough and smooth surfaces increase from 58 kPa to 95 kPa and from 298 kPa to 529 kPa, respectively, when probe size increases from a 50 μm radius to a 250 μm radius. In contrast, increasing the displacement rate for indentations made with the 250 μm radius probe from 1 $\mu\text{m/s}$ to 50 $\mu\text{m/s}$ has no effect on the relative difference in effective contact modulus between the rough and smooth surfaces (76.5 % and 74.4%, respectively).

While the influence of surface roughness on the indentation of articular cartilage was evident, the drastic reduction in measured moduli was not predicted by past investigations using linear-elastic materials. Finite element modeling of contact between a conospherical probe and rough PDMS and silicone rubber surfaces by Chen and Diebels revealed that the measured properties are consistently reduced when the asperity spacing, $R_{\lambda q}$, is less than half of the probe radius¹³. When the asperity spacing was larger than this limit, surface roughness affects the variation but did not affect the mean of the measured properties. The average

asperity spacing of the rough cartilage surface used in the current study was found to be $R_{\lambda q} = 63.0 \pm 17.4 \mu\text{m}$, which is greater than $50 \mu\text{m}$ radius probe and greater than half the radius of the $105 \mu\text{m}$ radius probe used in depth-sensing indentation. Yet, the equilibrium modulus of the rough surface, measured using the $50 \mu\text{m}$ radius and $105 \mu\text{m}$ radius probes, was reduced by 80% and 94%, respectively. A separate, experimental investigation of the influence of surface roughness on the microindentation behavior of glassy polymers by Wai *et al.* demonstrated that the surface roughness influences the measured moduli at indentation depths less than the measured peak to valley distance, S_z , under contact¹⁵. Indentation depths in this study were related to the probe radius by $\delta_{max} = 0.05R_i$, giving maximum indentation depths of $0.05 \mu\text{m}$, $0.625 \mu\text{m}$, $2.5 \mu\text{m}$, $5.25 \mu\text{m}$, and $12.5 \mu\text{m}$ for the $1 \mu\text{m}$, $12.25 \mu\text{m}$, $50 \mu\text{m}$, $105 \mu\text{m}$, and $250 \mu\text{m}$ radius probes, respectively. Measured peak to valley distances corresponding to each probe radius exceeded the maximum indentation depth for all probe sizes except for $R_i = 250 \mu\text{m}$. The moduli of the rough and smooth surfaces measured using the $250 \mu\text{m}$ radius probe should be equal, but this was not the case for the porcine articular cartilage surfaces. The mean equilibrium modulus of the rough surface was 75% smaller than the mean equilibrium modulus of the smooth surface. Furthermore, the maximum indentation depth was always larger than S_z for indents on the smooth surface. Yet, the effective contact modulus and equilibrium modulus increased consistently with indentation depth. Taken together, the departure from previous findings suggests that the increased surface roughness affects more than the assumed well-defined relationship between probe displacement and the area of the probe in contact.

One possible explanation for the enhanced influence of surface roughness is the disruption of the collagen network during sectioning. It has been proposed that an intact

collagen network is highly important to the indentation behavior of articular cartilage^{24–26}. Fibers oriented transverse to the testing surface resist compression due to concentrated loads, such as those imposed during indentation. While previous investigations specifically reference this effect in the context of the superficial zone, it is possible that indentation in the middle zone of a full-thickness cross-section reproduces the same effect. The influence of fiber reinforcement, coupled with the altered relationship between probe displacement and the area in contact, may explain the considerable reduction in equilibrium modulus for the rough surface, as well as the persistence of reduced moduli at indentation depths larger than the measured peak to valley distance under contact. Furthermore, fiber-reinforcement has been shown to be important in fluid load support²⁵, with reinforcement resulting in larger interstitial fluid pressure during compression. This conclusion may explain why the effective contact modulus of the rough surface is reduced by relatively the same percentage as the equilibrium modulus when compared to the smooth surface.

Finally, there are several limitations of the present study that should be addressed in future investigations. Perhaps the most obvious limitation is that only one sample per group was used during indentation testing. Cartilage mechanical properties vary with anatomical location, between animals, and between species. Care was taken in the sample preparation during this study. Samples were from the same animal, joint, and anatomical location within the joint to ensure that, to the best of our ability, the only difference between the samples was the surface roughness. Second, only a single indentation depth was used for each probe radius, limiting our ability to decouple indentation from probe radius. Additional indentation depths may help elucidate the influence of surface roughness on contact area separately from the

disruption of the collagen network. Lastly, while it has been demonstrated in other studies that sectioning leads to fibrillation of the collagen network, complementary imaging of the near surface collagen structure would explicitly address whether the enhanced influence of surface roughness is associated with the effect of fiber reinforcement.

3.6.0 Conclusions

In summary, microindentation of rough and smooth porcine articular cartilage surfaces demonstrate a significant influence of surface roughness on the measured effective contact and equilibrium moduli. The influence of surface roughness decreased with increasing probe size and indentation depth and persisted even when indentation depths exceeded the maximum peak to valley distance under contact. We hypothesize that the increased influence of surface roughness in the present study, compared to previous investigations, results from local disruption of the collagen network during sectioning. Our results also indicate that AFM-based microindentation may be unsuitable for evaluating sectioned cartilage surfaces. Tests with the smallest probe radius resulted in effective contact moduli that were practically indistinguishable between the rough and smooth surfaces. Finally, given the pronounced influence of surface roughness, we recommend that surface roughness be evaluated for all samples used in comparative studies to distinguish surface roughness from other effects that may influence articular cartilage's mechanical properties.

3.7.0 Conflicts of Interest

The authors have no conflicts of interest to report.

3.8.0 Author Contributions

Andrew Tomaschke: Study Design, Sample preparation, Depth-sensing microindentation, Analysis of AFM-based and depth-sensing microindentation data, Interpretation of results, Writing, and Editing.

Kaitlin McCreery: AFM-based Microindentation testing, Interpretation of results, Methods Writing, Editing

Virginia Ferguson: Interpretation of results, Editing.

3.9.0 References

- (1) Stolz, M.; Raiteri, R.; Daniels, A. U.; VanLandingham, M. R.; Baschong, W.; Aebi, U. Dynamic Elastic Modulus of Porcine Articular Cartilage Determined at Two Different Levels of Tissue Organization by Indentation-Type Atomic Force Microscopy. *Biophysical Journal* **2004**, *86* (5), 3269–3283.
- (2) Loparic, M.; Wirz, D.; Daniels, A. U.; Raiteri, R.; VanLandingham, M. R.; Guex, G.; Martin, I.; Aebi, U.; Stolz, M. Micro- and Nanomechanical Analysis of Articular Cartilage by Indentation-Type Atomic Force Microscopy: Validation with a Gel-Microfiber Composite. *Biophysical Journal* **2010**, *98* (11), 2731–2740.
- (3) Paietta, R. C.; Campbell, S. E.; Ferguson, V. L. Influences of Spherical Tip Radius, Contact Depth, and Contact Area on Nanoindentation Properties of Bone. *Journal of Biomechanics* **2011**, *44* (2), 285–290.
- (4) Bonnevie, E. D.; Baro, V. J.; Wang, L.; Burris, D. L. Fluid Load Support during Localized Indentation of Cartilage with a Spherical Probe. *Journal of Biomechanics* **2012**, *45* (6), 1036–1041.
- (5) Moore, A. C.; Burris, D. L. Tribological and Material Properties for Cartilage of and throughout the Bovine Stifle: Support for the Altered Joint Kinematics Hypothesis of Osteoarthritis. *Osteoarthritis and Cartilage* **2015**, *23* (1), 161–169.
- (6) Richard, F.; Villars, M.; Thibaud, S. Viscoelastic Modeling and Quantitative Experimental Characterization of Normal and Osteoarthritic Human Articular Cartilage Using Indentation. *Journal of the Mechanical Behavior of Biomedical Materials* **2013**, *24*, 41–52.

- (7) Stolz, M.; Gottardi, R.; Raiteri, R.; Miot, S.; Martin, I.; Imer, R.; Staufer, U.; Raducanu, A.; Düggelin, M.; Baschong, W.; Daniels, A. U.; Friederich, N. F.; Aszodi, A.; Aebi, U. Early Detection of Aging Cartilage and Osteoarthritis in Mice and Patient Samples Using Atomic Force Microscopy. *Nature Nanotechnology* **2009**, *4* (3), 186–192.
- (8) Wahlquist, J. A.; DelRio, F. W.; Randolph, M. A.; Aziz, A. H.; Heveran, C. M.; Bryant, S. J.; Neu, C. P.; Ferguson, V. L. Indentation Mapping Revealed Poroelastic, but Not Viscoelastic, Properties Spanning Native Zonal Articular Cartilage. *Acta Biomaterialia* **2017**, *64*, 41–49.
- (9) Fischenich, K. M.; Wahlquist, J. A.; Wilmoth, R. L.; Cai, L.; Neu, C. P.; Ferguson, V. L. Human Articular Cartilage Is Orthotropic Where Microstructure, Micromechanics, and Chemistry Vary with Depth and Split-Line Orientation. *Osteoarthritis and Cartilage* **2020**, *28* (10), 1362–1372.
- (10) HERTZ, H. On the Contact of Elastic Solids. *Z. Reine Angew. Mathematik* **1881**, *92*, 156–171.
- (11) Oliver, W. C.; Pharr, G. M. Measurement of Hardness and Elastic Modulus by Instrumented Indentation: Advances in Understanding and Refinements to Methodology. *Journal of Materials Research* **2004**, *19* (1), 3–20.
- (12) Greenwood, J. A.; Johnson, K. L.; Matsubara, E. A Surface Roughness Parameter in Hertz Contact. *Wear* **1984**, *100* (1), 47–57.
- (13) Chen, Z.; Diebels, S. Modelling and Parameter Re-Identification of Nanoindentation of Soft Polymers Taking into Account Effects of Surface Roughness. *Computers & Mathematics with Applications* **2012**, *64* (9), 2775–2786.
- (14) Donnelly, E.; Baker, S. P.; Boskey, A. L.; van der Meulen, M. C. H. Effects of Surface Roughness and Maximum Load on the Mechanical Properties of Cancellous Bone Measured by Nanoindentation. *J Biomed Mater Res A* **2006**, *77* (2), 426–435.
- (15) Wai, S. W.; Spinks, G. M.; Brown, H. R.; Swain, M. Surface Roughness: Its Implications and Inference with Regards to Ultra Microindentation Measurements of Polymer Mechanical Properties. *Polymer Testing* **2004**, *23* (5), 501–507.
<https://doi.org/10.1016/j.polymertesting.2004.01.001>.
- (16) Yoshioka, M.; Coutts, R. D.; Amiel, D.; Hacker, S. A. Characterization of a Model of Osteoarthritis in the Rabbit Knee. *Osteoarthritis and Cartilage* **1996**, *4* (2), 87–98.
- (17) Desrochers, J.; Amrein, M. A.; Matyas, J. R. Structural and Functional Changes of the Articular Surface in a Post-Traumatic Model of Early Osteoarthritis Measured by Atomic Force Microscopy. *Journal of Biomechanics* **2010**, *43* (16), 3091–3098.

- (18) Cooke, M. E.; Lawless, B. M.; Jones, S. W.; Grover, L. M. Matrix Degradation in Osteoarthritis Primes the Superficial Region of Cartilage for Mechanical Damage. *Acta Biomaterialia* **2018**, *78*, 320–328.
- (19) Krishnan, R.; Caligaris, M.; Mauck, R. L.; Hung, C. T.; Costa, K. D.; Ateshian, G. A. Removal of the Superficial Zone of Bovine Articular Cartilage Does Not Increase Its Frictional Coefficient. *Osteoarthritis and Cartilage* **2004**, *12* (12), 947–955.
- (20) Chandran, P. L.; Dimitriadis, E. K.; Mertz, E. L.; Horkay, F. Microscale Mapping of Extracellular Matrix Elasticity of Mouse Joint Cartilage: An Approach to Extracting Bulk Elasticity of Soft Matter with Surface Roughness. *Soft Matter* **2018**, *14* (15), 2879–2892.
- (21) Hutter, J. L.; Bechhoefer, J. Calibration of Atomic-force Microscope Tips. *Review of Scientific Instruments* **1993**, *64* (7), 1868–1873.
- (22) Long, R.; Hall, M. S.; Wu, M.; Hui, C.-Y. Effects of Gel Thickness on Microscopic Indentation Measurements of Gel Modulus. *Biophysical Journal* **2011**, *101* (3), 643–650.
- (23) Mattice, J. M.; Lau, A. G.; Oyen, M. L.; Kent, R. W. Spherical Indentation Load-Relaxation of Soft Biological Tissues. *Journal of Materials Research* **2006**, *21* (8), 2003–2010.
- (24) Korhonen, R. K.; Wong, M.; Arokoski, J.; Lindgren, R.; Helminen, H. J.; Hunziker, E. B.; Jurvelin, J. S. Importance of the Superficial Tissue Layer for the Indentation Stiffness of Articular Cartilage. *Medical Engineering & Physics* **2002**, *24* (2), 99–108.
- (25) Li, L. P.; Soulhat, J.; Buschmann, M. D.; Shirazi-Adl, A. Nonlinear Analysis of Cartilage in Unconfined Ramp Compression Using a Fibril Reinforced Poroelastic Model. *Clinical Biomechanics* **1999**, *14* (9), 673–682.
- (26) Soulhat, J.; Buschmann, M. D.; Shirazi-Adl, A. A Fibril-Network-Reinforced Biphasic Model of Cartilage in Unconfined Compression. *Journal of Biomechanical Engineering* **1999**, *121* (3), 340–347.

CHAPTER 4

Fracture Toughness of Functionally Graded Interfaces Between Polymeric Materials with Divergent Mechanical Properties

4.1.0 Abstract

Composite hydrogel tissue engineering scaffolds offer a unique combination of mechanical stiffness and biocompatibility that cannot be met using a single material. Yet, combining hydrogel materials with divergent mechanical properties and differential swelling ratios can lead to unstable interfaces that fail under physiological loading. Functionally graded interfaces may reduce stress concentrations at interfaces, but the fracture toughness behavior of a graded interface between hydrogel materials has not been thoroughly characterized. The work presented here represents the first step towards creating robust functionally graded hydrogel interfaces. Preliminary notch fracture testing was performed on functionally graded polymer interfaces with a three order of magnitude difference in elastic modulus between constituents. Our results thus far indicate that functionally graded interfaces may offer a considerable improvement in fracture toughness over sharp bi-material interfaces as evidenced by the shift in failure point from an existing pre-crack at the interface to the pure, soft constituent. Testing of additional functional gradients (e.g., property gradient vs. material

gradient), and an updated notching protocol are recommended for thorough characterization of the functionally graded interfaces.

4.2.0 Introduction

Composite hydrogel tissue engineering scaffolds offer an alternative approach to the repair of focal defects in articular cartilage^{1,2}. This approach combines a stiff, mechanically robust hydrogel with a soft cell-laden hydrogel to create a scaffold with properties that cannot be achieved using a single material. The stiff, mechanically robust hydrogel is used to create a hollow structure that supports the tissue surrounding a defect, preventing further degradation under physiological loading³. The soft, cell-laden hydrogel provides the ideal environment for cells to synthesize new ECM and quickly degrades to allow formation of macroscopic neotissue⁴⁻⁶. While promising, it is well understood that the interface between materials with dissimilar mechanical properties creates a stress concentration under loading, increasing the likelihood of interfacial failure^{7,8}. This problem is exacerbated using hydrogels, as differential swelling leads to additional stresses at the interface^{9,10}.

Functionally graded interfaces (FGIs) offer a potential solution to the problem of dissimilar interfaces by extending the dimension over which the change in properties occurs. The more gradual change in mechanical properties theoretically increases the bonding strength between dissimilar materials¹¹. The relative improvement in fracture toughness depends on the ratio of the elastic moduli (E_{hard}/E_{soft}), the location of crack initiation, and the shape of the property gradient between the two materials^{8,12,13}. Yet, it still remains unclear if these numerical simulations between stiff elastic-plastic materials with relatively similar moduli

($E_{hard}/E_{soft} < 10$), translate to hydrogel interfaces with divergent mechanical properties ($E_{hard}/E_{soft} > 1000$). As far as the authors are aware, a comprehensive characterization of FGIs between dissimilar hydrogels does not exist. This paucity of information likely follows the manufacturing challenges associated with hydrogel materials. Multi-material printing using hydrogel materials is still relatively new and not yet capable of producing continuous material gradients^{14,15}.

A first step towards characterizing FGIs between hydrogel materials could be taken through an investigation of the fracture behavior of FGIs between polymers with a similar ratio of elastic moduli. Multi-material printing is well established for polymer materials and the printing of continuous functional gradients between dissimilar polymers with $E_{hard}/E_{soft} > 1000$ has already been demonstrated^{16–18}. Using these materials, Mirzaali et al. showed that abrupt transitions and smaller interfacial widths increase fracture resistance when the crack is oriented parallel to the material gradient¹⁶. It was also found that for cracks in the soft phase (oriented normal to the material gradient), continuous, linear material gradients improved fractured toughness compared to stepwise gradients¹⁷. However, the researchers left two questions unanswered. First, how does the fracture behavior of a functional property gradient compare to a functional material gradient? Second, how does the interfacial width influence fracture toughness for cracks initiating at the center of the interfacial region? Answering these questions will refine our understanding of fracture behavior of FGIs between polymers with divergent mechanical properties and allow the prediction of fracture behavior of FGIs between hydrogels once multi-material hydrogel printing becomes more accessible.

The objective of the present study is to investigate the role of interfacial width on the fracture toughness of FGIs between dissimilar polymer materials for cracks initiating in the interfacial region. This objective is achieved via single edge notch fracture testing of FGIs of varying interfacial width between polymers with an elastic modulus difference of approximately three orders of magnitude. The results of fracture testing will: 1) evaluate the relative improvement in fracture toughness of FGIs over a bi-material interface between dissimilar polymer materials 2) guide future investigations into the fracture behavior of FGIs between hydrogel materials 3) aid researchers in the design of polymer composites with dissimilar mechanical properties.

4.3.0 Materials and Methods

4.3.1.A Materials for Study A

Two commercially available polymers with dissimilar material properties were chosen for the current study. The stiff phase consisted of VeroYellow™ ($E = 2-3 \text{ GPa}$). The soft phase consisted of Agilus30Clear™ ($E = \sim 0.6 \text{ MPa}$). Both materials are compatible with the multi-material Objet350 Connex3™ 3D printer (Stratasys® Ltd.). The printer uses inkjet technology to deposit individual droplets which are subsequently cured using UV light.

4.3.1.B Materials for Study B

Two commercially available polymers with dissimilar material properties were chosen for the current study. The stiff phase consisted of VeroYellow™ ($E = 2-3 \text{ GPa}$). The soft phase consisted of TangoBlack™, which has a modulus similar to Agilus30Clear™. Both materials are compatible with the multi-material Objet350 Connex3™ 3D printer (Stratasys® Ltd.). The printer

uses inkjet technology to deposit individual droplets which are subsequently cured using UV light.

4.3.2.A Samples for Notch Fracture Testing – Study A

To evaluate the influence of interfacial width and provide context for the fracture testing results, seven different groups of samples were designed and additively manufactured for fracture testing (n=5 samples per group). Groups VA & AA consisted of the pure stiff or soft materials, respectively. Additionally, four types of samples with interfaces formed between the VeroYellow™ and Agilus30Clear™ materials produced groups G0A, G5A, G10A, G20A, & G40A with a sharp, bi-material interface (G0) and functionally graded interfaces of interfacial widths of 5 mm, 10 mm, and 20 mm, and 40 mm, respectively. Samples were manufactured using the Objet350 Connex3™ 3D printer by creating binary images (Fig. 4.1) that communicate to the printer which material to deposit at specified locations. The overall dimensions of each sample were kept consistent ($L = 40\text{ mm}$, $W = 10\text{ mm}$, $T = 5\text{ mm}$).

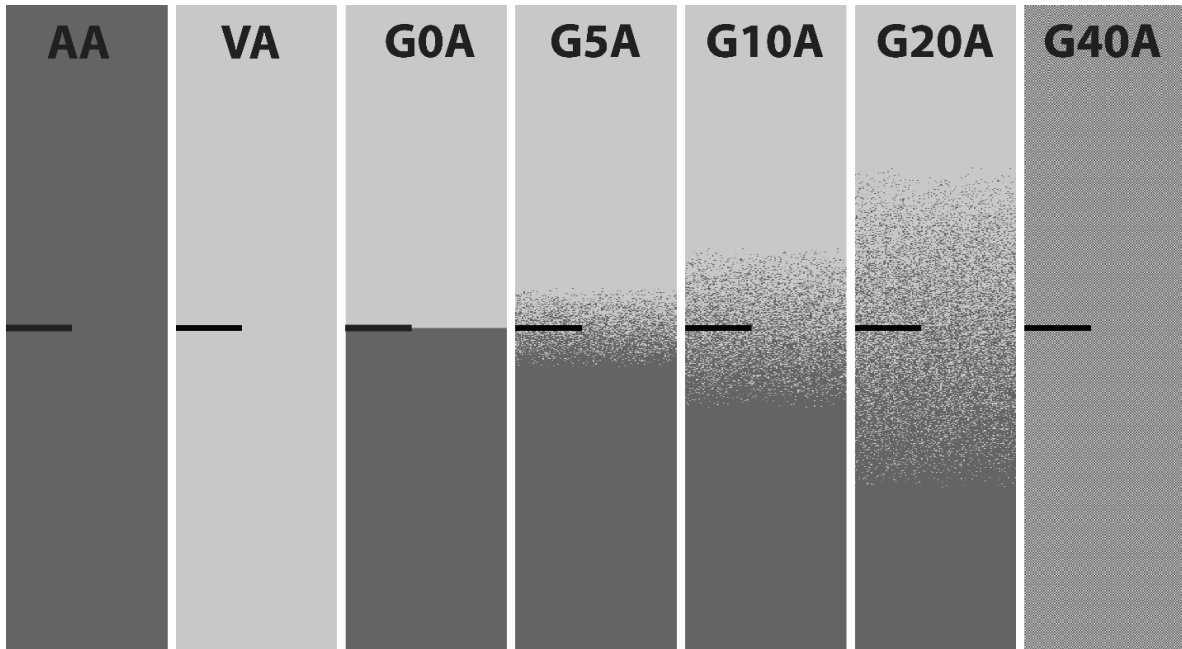


Figure 4. 1 Study A Designs ($L \times W \times t$: 40 mm x 10 mm x 5 mm). The printed notch (Black bar) was 4 mm x 350 μ m

4.3.2.B Samples for Notch Fracture Testing – Study B

Samples were redesigned for Study B. Sample groups tested in Study B included pure TangoBlack+ (Group TB), a 2 mm graded interface (Group G02B) and a 10 mm graded interface (Group G10B). Redesigned samples include the Vero material at both ends of the sample to facilitate gripping, and a graded transition from the grip region to the rest of the sample where necessary. The samples are also made wider (15 mm) and longer (100 mm). Lastly, for the graded samples, the length of the pure-Vero region was reduced to save resin, since virtually no deformation occurs in this region (Fig. 4.2).

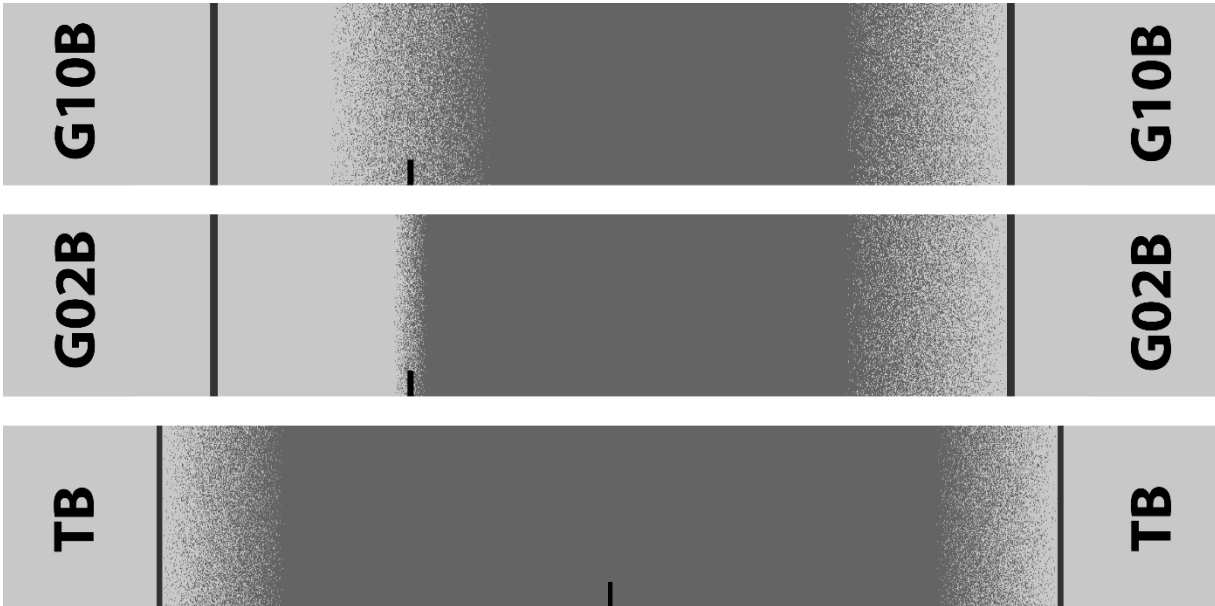


Figure 4. 2 Study B Designs ($L \times W \times t$: 100 mm x 15 mm x 5 mm). The printed notch (Black bar) was 2 mm x 250 μ m

4.3.3.A Notching of Samples – Study A

For preliminary testing, the notch was located at the center of the interface. First, a 4 mm long, 350 μ m wide notch was included in the print file for each sample group. Then, in order to create a sharp crack tip, a razor blade was used to extend the printed notch by an additional 1 mm while samples were fixed inside of a jig. Samples were imaged after notching to determine sample-specific crack lengths in to capture any variation in the notching technique.

4.3.3.B Notching of Samples – Study B

For the updated sample designs, a 2 mm long, 250 μ m notch was printed and then extended to 3.5 mm using a razor blade. Notches were not imaged for the updated sample designs.

4.3.4 Notch Fracture Testing – Study A

Samples were fixed on either end using steel grips. 5 mm on each end was fed into the grips prior to clamping to keep a consistent gauge-length between the free ends of the grips. Tensile testing was performed on an Insight 2[®] electromechanical testing system (MTS systems corporation, Eden Prairie, MN) using a 2 kN load cell and MTS Testworks[®] software. Samples were loaded in tension using a displacement-controlled method with an extension rate of 3 mm/min until complete fracture occurred. Force, P , extension, δ , and time, t , signals were recorded at a rate of 200 Hz throughout the course of testing. The fracture surface was imaged after testing to assess crack propagation behavior.

4.3.4 Notch Fracture Testing – Study B

Samples were fixed on either end using steel grips. Each end was fed into the grips prior to clamping to keep a consistent gauge-length between the free ends of the grips. Tensile testing was performed on TestResources Dynamic Material Analyzer (TestResources, Shakopee, MN) using a 100 lbf load cell. Samples were loaded in tension using a displacement-controlled method with an extension rate of 30 mm/min until complete fracture occurred. Force, P , extension, δ , and time, t , signals were recorded at a rate of 1000 Hz throughout the course of testing. The fracture surface was imaged after testing to assess crack propagation behavior.

4.3.5 Work of Fracture Analysis – Study A and Study B

For both the preliminary testing and updated sample testing, to assess the relative fracture toughness of the different sample groups, the work of fracture, U_f , was calculated as:

$$U_f = \int_0^{\delta_f} P \partial\delta \quad (1)$$

Where δ_f is the extension at complete fracture. From the work of fracture, the fracture toughness, G_f , was determined using:

$$G_f = \frac{U_f}{A_f} \quad (2)$$

Where A_f is the uncracked cross-sectional area of the sample. It should be noted that (2) is only representative of the real fracture toughness in the case of linear-elastic conditions. The soft phase in the present study is highly non-linear-elastic, as such, (2) only provides a comparative measurement between sample groups.

4.4.0.A Results – Study A

Preliminary fracture testing was performed on n=1 for the pure stiff phase (Group VA, VeroYellow™), pure soft phase (Group AA, AgilusTranslucent™), and the bi-material interface sample (G0A) and the graded interface samples (G5A, G10A, & G20A). Group G40A was not evaluated as part of the preliminary work. Samples were printed with notches at the center of each fracture testing specimen and the notch was extended using a razor blade to produce a sharp crack tip radius. For groups VA, AA, and G0A, the cracks propagated across the sample and fracture toughness was evaluated. For Group G5A, the crack initially propagated from the notch, but the specimen failed at the interface of the soft phase with the testing grips prior to complete propagation across the specimen. Group G10A exhibited an opening of the initial crack tip before failing at the interface between the soft phase and the grips, and G20A failed at the interface between the soft phase and the grips prior to any observable opening of the initial crack.

4.4.1.A Notching – Study A

The initial crack lengths varied by sample group but were more consistent within groups. The sharp bi-material sample (Group G0A) had an initial crack length, a , of 4.51 mm (Fig 2). The Group VA samples had an initial crack length of $a = 4.89$ mm. Group AA samples had a mean initial crack length of $a = 5.13$ mm. The G5A, G10A, and G20A samples had initial crack lengths of $a = 5.61$ mm, 5.16 mm, and 5.21 mm, respectively. The drift of the mean crack length from Group G0A to Group G5A corresponds with the order in which groups were notched. The pressure required to extend the crack the final millimeter resulted in a sliding of the bottom plate of the jig, resulting in larger cracks. The jig was readjusted after the G5A group, resulting in the initial crack lengths closer to the target 5 mm for the G10A and G20A groups (Fig. 4.3).

In addition to the inconsistent initial crack lengths, the crack for the sharp bi-material interfaces (Group G0A) could not be aligned perfectly with the interface. The stiff phase at the back of the G0A samples was dimensionally inconsistent, causing the razor (and crack tip) to deflect into the soft phase.

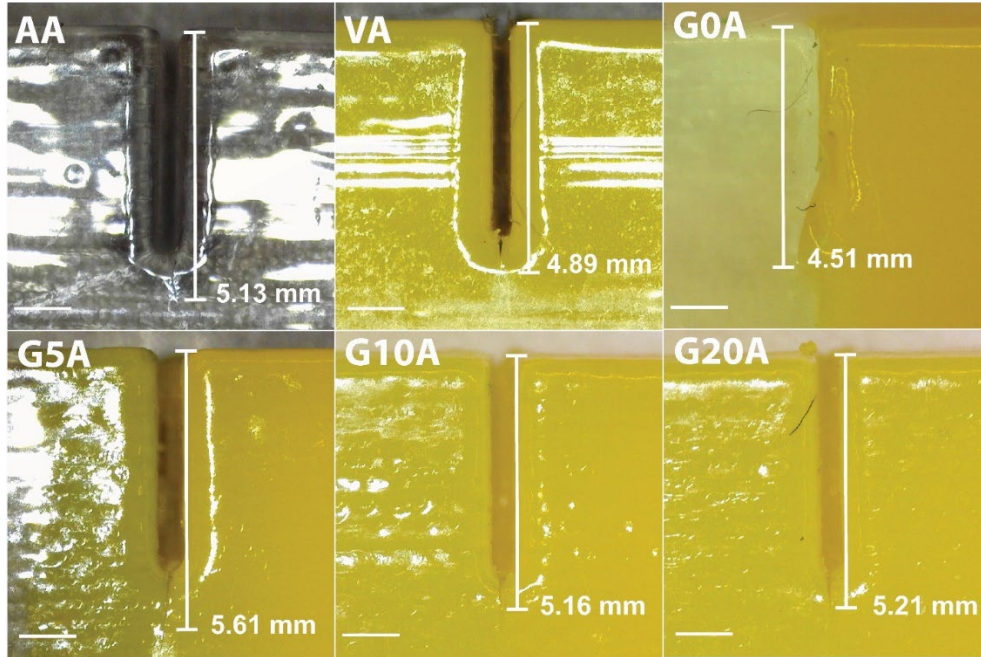


Figure 4.3 Images of the initial crack lengths (Group G40 absent). Scale bars = 1 mm

4.4.2.A Fracture Testing – Study A

Complete fracture was observed for Group VA, Group AA, and Group GOA. For graded samples Groups G5A, G10A, and G20A, the soft phase failed at the grips prior to propagation of the crack across the sample. Even with adjustments to the gripping procedure to reduce the gripping pressure (sandpaper + cyanoacrylate), the soft phase still failed at the interface with the testing grips. The interfacial crack of the G5A sample propagated towards the soft phase prior to complete failure at the grips, but this may have been an effect of the redistribution of stress as the sample began to tear at the interface of the soft phase with the grips.

Preliminary fracture testing results were distinctly different for each of the sample groups evaluated. The largest load was observed for Group VA, which reached a peak load of $P = 330.9\text{ N}$ prior to failure. The peak loads were lowest for Groups AA and GOA ($P = 11.8\text{ N}$ and 16.421 N , respectively). The peak loads for the graded samples decreased with increasing

interfacial width ($P = 41.2\text{ N}$, 36.6 N , and 34.2 N for the Groups G5A, G10A, and G20A, respectively). The highest extension was observed for Group AA, $\delta_f = 24.1\text{ mm}$. The maximum extension of the Group G5A was similar to the soft sample, $\delta_f = 21.7\text{ mm}$. Similar to the maximum load, the maximum extension decreased with interfacial width ($\delta_f = 18.9\text{ mm}$ and 14.7 mm for Groups G10A, and G20A, respectively). Group G0A failed at a similar extension to that of Group G20A, $\delta_f = 14.7\text{ mm}$. The smallest extension at complete fracture was observed for Group VA, $\delta_f = 0.327\text{ mm}$ (Fig. 4.4).

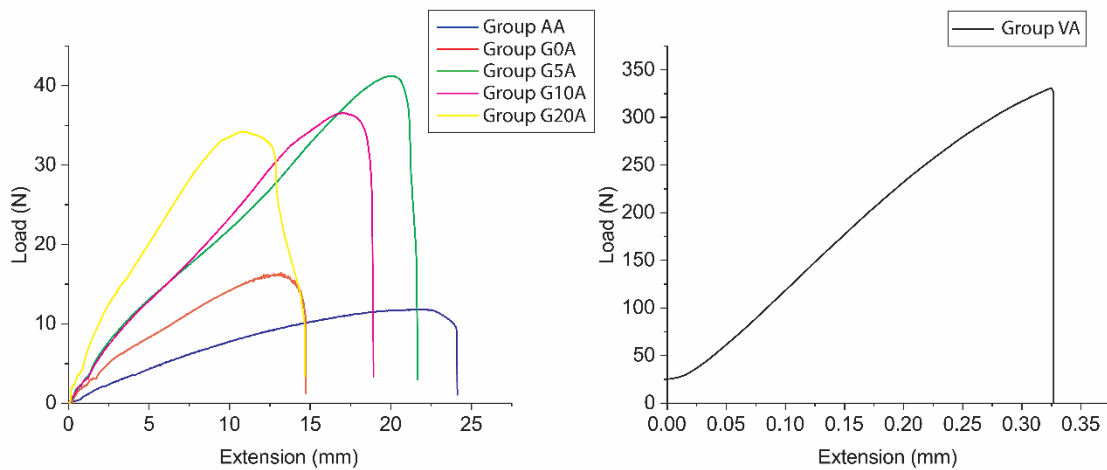


Figure 4. 4 Load vs. Extension curves from fracture testing of samples from Study A.

We were only able to evaluate the fracture toughness of Groups AA, VA, and G0A as a result of the tearing in the soft phase of the G5A, G10A, and G20A samples at the interface with the testing grips. The fracture toughness of Groups AA and VA were $G = 2372.7\text{ J/m}^2$ and 7778.6 J/m^2 , respectively. The fracture toughness of Group G0A fell between Groups VA and AA, $G = 5527.8\text{ J/m}^2$.

4.4.0.B Results – Study B

Notch fracture testing was performed on $n=4$ for each of the three groups in Study B (Groups TB, G02B, G10B). Cracks propagated completely across the sample width for Groups TB and G02B, while the sample consistently failed in the pure soft phase for Group G10B. Notably, none of the samples failed at the interface between the grip and the soft phase. The redesign successfully removed the stress concentration at the grips.

4.4.1.B Notching – Study B

No results to report. Notching was not imaged for Study B.

4.4.2.B Fracture Testing – Study B

Complete fracture was observed for Groups TB and G02B. For Group G10B, the sample failed in the pure soft region without any propagation of the initial crack. The highest peak loads were observed for Group G10B ($P = 48.9\text{ N}$ to 53.6 N), whereas the smallest loads were observed for Group TB ($P = 17.2\text{ N}$ to 19.6 N). Group G02B fell between Groups G10B and Group TB ($P = 27.2\text{ N}$ to 28.5 N). The largest maximum extension was observed for Group TB ($\delta_f = 33.4\text{ mm}$ to 38.1 mm), followed closely by Group G10B ($\delta_f = 35.2\text{ mm}$ to 37.3 mm). Group G02B had the smallest maximum extension ($\delta_f = 27.0\text{ mm}$ to 28.1 mm) (Fig. 4.5).

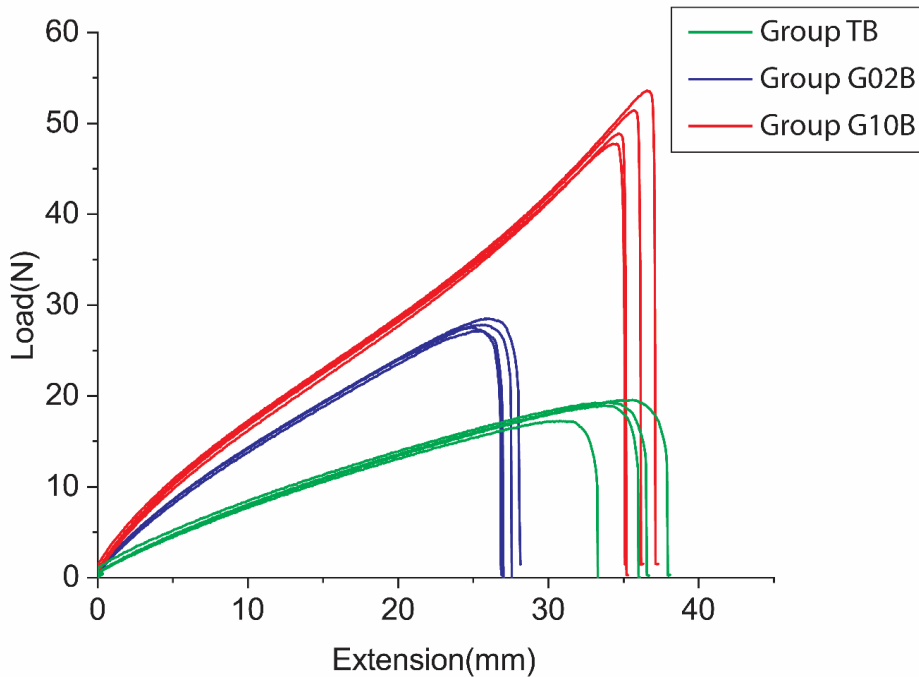


Figure 4. 5 Load vs. Extension curves from fracture testing of samples from Study B.

Fracture toughness was evaluated for Groups TB and G02B, Group G10B was omitted as the sample failed in the soft phase. The fracture toughness of Group TB was smaller than Group G02B, with ranges of $G = 6164.5 \text{ J/m}^2$ to 8020.9 J/m^2 and $G = 7730 \text{ J/m}^2$ to 8514.2 J/m^2 , respectively.

4.5.0 Discussion

The objective of the present study was to evaluate the influence of interfacial width on the fracture toughness of functionally graded interfaces between polymeric materials with divergent material properties. Two preliminary studies were run to achieve this objective. Preliminary study A evaluated the fracture toughness of a sharp bi-material interface as compared to functionally graded interfaces of varying interfacial width. Our notch fracture testing results suggest that the inclusion of a functionally graded interface improves fracture

toughness over a sharp bi-material interface. However, samples with functionally graded interfaces failed prematurely at the interface between the grip and the soft phase, obscuring any conclusions about the role of interfacial width. A subset of samples were redesigned in preliminary study B to include a region of stiff material on either side of the sample to prevent tearing at the grips. Notch fracture testing of this subset of samples demonstrated both an elimination of the stress concentration at the grips and an increase in fracture toughness properties with interfacial width.

4.5.1 FGIs vs. Bi-material Interfaces

With the initial crack for the sharp bi-material sample (Group G0A) ending in the soft phase, we cannot claim that the fracture toughness of the interface was accurately characterized. However, we can argue that a crack propagating through the soft phase near the interface represents the best-case scenario for fracture of a sharp bi-material interface. While the results from the graded interface samples could not be used to determine a fracture toughness, we can say that the use of functionally graded interfaces guarantee failure in the soft phase under tensile loading. Therefore, in the context of a tissue-engineering scaffold, a functionally graded interface, at the very least, makes the scaffold is as tough as the weakest phase under tensile loading. Further testing, with a crack along the interface, will be required to judge whether or not the graded interfaces improve fracture toughness over the bi-material interface.

The results from study B support the conclusions drawn from study A. While a bi-material interface was not evaluated in study B, the considerable increase in peak load and extension when comparing Group G10B to Group G02B suggests that the fracture toughness

increases with interfacial width as predicted by numerical simulations. It is likely that Groups G02B and G10B both exhibit enhanced fracture toughness as compared to a bi-material interface, but this result will need to be confirmed in future testing.

4.5.2 Influence of the Soft Phase

In study A, the interfacial widths were varied (Groups G0A, G5A, G10A, and G20A) while the overall sample dimensions remained constant. Therefore, the size of the stiff and soft phases on either side of the interface decreases with increasing interfacial width. This sample design was chosen as it is relevant to the case of introducing a FGI into a composite material. Tissue engineering scaffolds, as an example, typically have specific size requirements to permit culture inside of a bioreactor or to standardize surgical procedures for implantation. Thus, the introduction of an FGI into an existing composite design would require shrinking the dimensions of the other phases. However, in the case of evaluating fracture properties, the shrinking of the softer phase also directly influences the fracture behavior.

The width and thickness of the soft phase were consistent across designs, but the length decreased with increasing interfacial width. The length of the soft phase was 20 mm, 17.5 mm, 15 mm, and 10 mm for Groups G0A, G5A, G10A, and G20A respectively. With the exception of Group G0A (which included an initial crack that deflected into the soft phase) the maximum extension decreased in the same order (G5, G10, G20). The decrease in maximum extension occurred as a product of the modulus mismatch between the stiff and soft phases and the relationship between extension and strain. The modulus of the stiff phase was approximately 3 orders of magnitude larger than the soft phase¹⁷ and so, under tensile loading, the majority of

the deformation occurred in the soft phase. The extension signal only measures the total deformation of the sample from the initial gauge length. Strain, ε , is related to extension, δ , by:

$$\varepsilon = \frac{\delta}{L} \quad (3)$$

Where L is the initial, undeformed length. This means that if all of the interfacial samples are deformed by the same extension, the largest strain in the soft phase occurs for the group with the smallest soft phase (and largest interfacial width). Failure occurs once a critical stress is reached, and strain is related to stress through Hooke's law. Therefore, failure of the soft phase will occur at smaller extensions for samples with larger interfacial widths, as was observed in the present study.

The dependence on the size of the soft phase also explains the reduced fracture toughness of Group G0A as compared to Group AA. With the initial crack of the Group G0A sample ending in the soft phase, one would expect a similar fracture toughness, however, the size of the soft phase was halved compared to Group AA, and resulted in higher strains at lower extensions, and thus, a lower relative fracture toughness.

Similarly, Mirzaali *et al.* demonstrated an influence of the size of the soft phase on the fracture toughness of notched tension specimens using the same stiff and soft materials as we used in our study¹⁷. They tested step gradients with 5, 10, and 15 steps, a continuous linear gradient, a continuous sigmoidal gradient that approximates a sharp bi-material interface, and two other continuously graded samples where the center region was a mix of the stiff and soft phases. Key differences between our studies are that Mirzaali tested symmetric samples (stiff→graded→soft→graded→stiff), the interfacial width was not varied (all gradients were

100% of the sample length), and the crack was located in the central soft phase. The symmetric sample designs and different gradient shapes resulted in varying sizes of the pure soft phase at the center of the specimen. The size of the soft phase was largest for 5 and 10-step gradients, followed by the 15-step gradient, and smallest for the sigmoid and linear continuous gradients. Fracture toughness decreased with the size of the soft phase and samples with the same size soft phase (5-step vs. 10 step, Linear continuous vs. Sigmoid) exhibited a higher fracture toughness for the more gradual gradient (10-step > 5-step, Linear > Sigmoid).

Interestingly, the samples evaluated in study B did not exhibit the same dependence on the size of the soft phase as was observed in Study A or Mirzaali *et al.* The length of the soft phase was largest for Group TB, followed by Group G02B, and then Group G10B. The largest extension was observed for Group TB, as might be expected given the results of study A. In contrast, the smallest extension was observed for Group G02B, not G10B, as would be predicted from the results of study A. Our results suggest that the elimination of the stress concentration at the grips also mitigates the influence of the soft phase on the observed fracture behavior.

4.5.3 Crack Propagation Behavior

Similar to the fracture testing results, the crack propagation behavior was also distinctly different for each of the sample groups evaluated. The crack propagated straight across the width of the sample for both Group VA and Group AA samples but occurred at very different rates. Once fracture was initiated for Group VA, the crack propagated across the sample almost instantaneously. In fact, the rate of crack propagation had an average crack velocity, v , that was greater than 1000 *mm/s*. As a comparison, the crack propagation of Group AA occurred much

more slowly, at an estimated velocity of 0.11 *mm/s*. The slow crack propagation in the pure soft sample is predicted by the viscoelastic behavior of the Agilus material. The fracture of soft materials is accompanied by the formation of a process zone around the crack ¹⁹. If a material is viscoelastic, mechanical dissipation occurs in the process zone, which in-turn limits the energy available to advance the crack tip ²⁰.

Unlike the stiff and soft samples, the crack of the graded sample did not proceed straight across the sample. Instead, the crack deflected significantly towards the soft phase with a concave upward shape until the interface between the graded and soft region was reached. The crack deflection aligned with Gu and Asaro's model for crack deflection in a functionally graded material ²¹. The model predicted that the material gradient has a strong effect on kink direction for a crack at the center of a functionally graded interface. Specifically, for an edge crack at the center of an FGM, the crack is predicted to propagate towards the softer phase and the sharpness of the kink angle, α , increased with modulus mismatch, α , calculated as:

$$\alpha = \frac{E_{hard} - E_{soft}}{E_{hard} + E_{soft}} \quad (4)$$

The kink angle also depends on the parameter, Ω , calculated as:

$$\Omega = \frac{Im(K^{\infty} h^{i\varepsilon})}{Re(K^{\infty} h^{i\varepsilon})} \quad (5)$$

Where K^{∞} is the complex stress intensity factor, h is the relative thickness of the graded interface above the crack tip. The complex stress intensity factor is defined as:

$$K^{\infty} = K_I + K_{II}i \quad (6)$$

Marur and Tippur previously demonstrated that for an FGI loaded in tension, the mode-mixity, $\tan^{-1}(K_{II}/K_I)$, decreases with increasing interfacial width¹³. When the two works are taken together, we can predict the crack propagation direction for the sample groups tested in the present study.

For homogenous materials the value of $\alpha = 0$ and the loading is purely mode I, predicting a kink angle of 0 degrees, in accordance with the observed behavior of Group VA and Group AA samples. For the graded interfaces with an edge notch located at $h= 0.5$, $\alpha = \sim 1$, and mode-mixity decreases with increasing interfacial width. Therefore, we would predict that the smallest interfacial width (Group G5A) would possess the largest kink angle and the largest interfacial width (Group G40A) would possess the smallest kink angle. For the sharp bi-material interface (Group G0A), $\alpha = \sim 1$, and the mode-mixity is at a maximum, however, the parameter Ω also depends on h , and $h=0$. Thus, we would expect the kink angle for Group G0A to be smaller than the kink-angle for the functionally graded interfaces. The preliminary fracture results reasonably agree with these predictions. The interfacial cracks for Group G0A and G5A samples kinked at angles of approximately 15 and 45 degrees, respectively (Fig. 4.6). Though, it is possible the angle of the G0A sample is influenced by the errant notch, described in the results above.

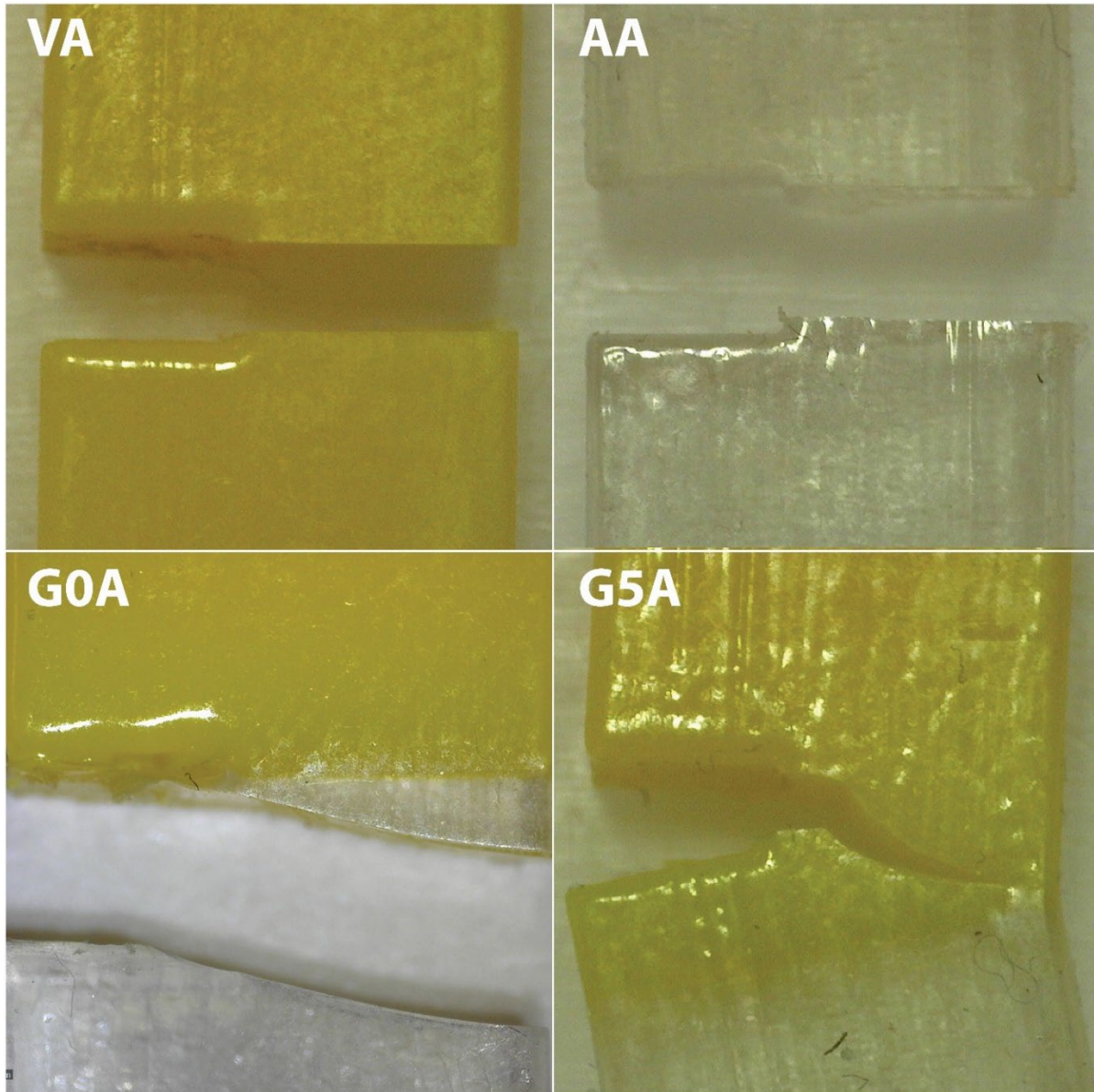


Figure 4. 6 Crack propagation behavior of samples from Study A

The results from study B tentatively align with the predicted crack behavior. The homogenous sample, Group TB exhibited a kink angle of 0 degrees, whereas Group G02B exhibited a kink angle of approximately 8 degrees (Fig. 4.7). While different materials were used in study B, the modulus mismatch of the two phases is similar to study A and the notch is still located at $h = 0.5$. Thus, we expected a kink angle of Group G02B that was larger than

Group G0A from study A. We hypothesize the unexpected behavior does indeed result from the errant notch of Group G0A. This will need to be verified in future testing.

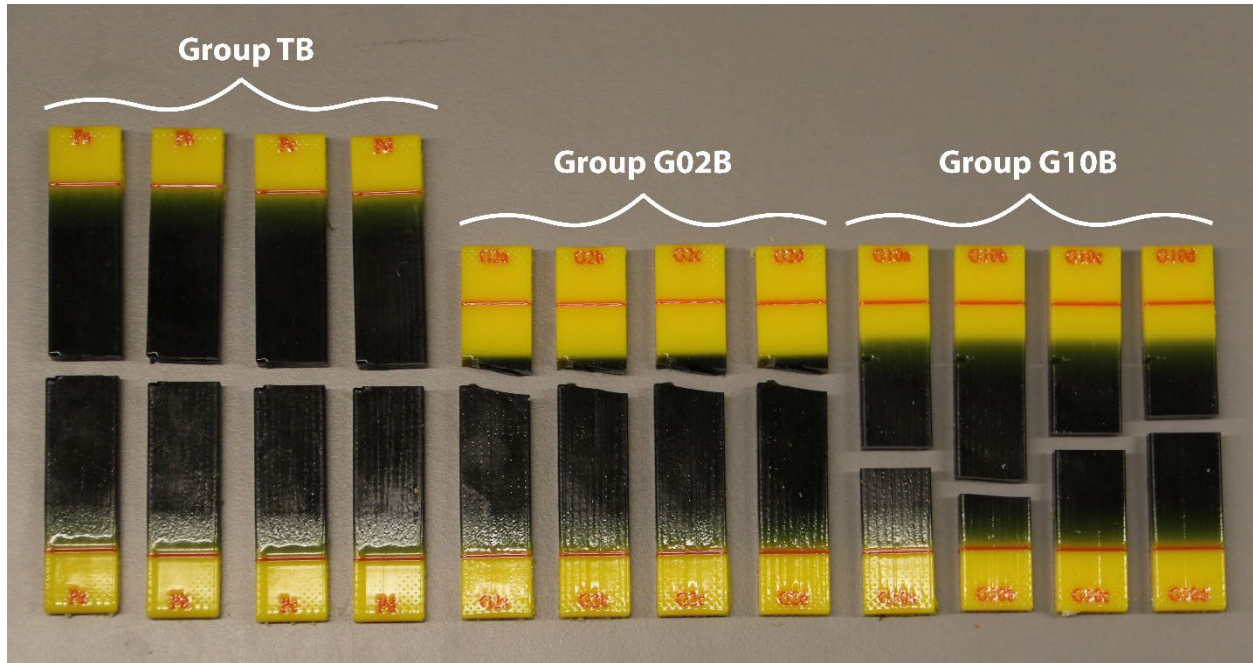


Figure 4. 7 Crack propagation behavior of samples from Study B

4.6.0 Limitations

While the inclusion of the Vero material on either end of the notch fracture samples eliminated failure at the grips and appears to eliminate the influence of the soft phase, only 3 groups have been evaluated to date. Testing of additional interfacial widths is required before we can responsibly conclude that the influence of the soft phase has been eliminated.

Notching remains inconsistent in both our ability to create notches of equal length and locate them in the center of the graded interface. A more advanced jig is required. Design of this jig should focus on achieving a consistent depth and fixing the razor to ensure the always extends the crack straight downward without deflecting towards the soft material.

One of the primary goals of the present study was to evaluate the fracture toughness of property gradients of varying interfacial width as compared to material gradients. Once the remaining testing inconsistencies are accounted for (e.g., inconsistent notching, influence of the soft phase), this comparison should become the primary focus of the study.

4.7.0 Conclusions

The results of the present study thus far highlight the challenges in the experimental validation of functionally graded interfaces. When one phase is significantly more compliant than the other, as is the case here, the FGI is still significantly stiffer than the soft phase. As a result, the FGI (even one with a flaw) acts as a mostly rigid top grip, leading to failure in the soft phase for all but the smallest interfacial widths. Additional testing will be performed with modified designs to determine if the size of the soft phase continues to affect fracture toughness. If the influence of the soft phase persists, another redesign will be required to keep the size of the soft phase consistent across sample groups. Lastly, the comparison between functional property gradients and material gradients needs to be the primary focus of future work. Answering this question would effectively eliminate half of the required testing to optimize the fracture toughness of a functionally graded interface.

4.8.0 Conflicts of Interest

The authors have no conflicts of interest to report

4.9.0 Author Contributions

Andrew Tomaschke: Study Design, Sample Notching, Sample Testing, Data Analysis, Writing, Editing

Lawrence Smith: Study Design, Sample Notching, Sample Testing

Victor Crespo-Cuevas: Sample Testing

Virginia Ferguson: Study Design, Editing

Rob MacCurdy: Study Design

4.10.0 References

- (1) Aisenbrey, E. A.; Tomaschke, A.; Kleinjan, E.; Muralidharan, A.; Pascual-Garrido, C.; McLeod, R. R.; Ferguson, V. L.; Bryant, S. J. A Stereolithography-Based 3D Printed Hybrid Scaffold for In Situ Cartilage Defect Repair. *Macromolecular Bioscience* **2018**, *18* (2), 1700267.
- (2) Schoonraad, S. A.; Fischenich, K. M.; Eckstein, K. N.; Crespo-Cuevas, V.; Savard, L. M.; Muralidharan, A.; Tomaschke, A. A.; Uzcategui, A. C.; Randolph, M. A.; McLeod, R. R.; Ferguson, V. L.; Bryant, S. J. Biomimetic and Mechanically Supportive 3D Printed Scaffolds for Cartilage and Osteochondral Tissue Engineering Using Photopolymers and Digital Light Processing. *Biofabrication* **2021**, *13* (4), 044106.
- (3) Aisenbrey, E. A.; Tomaschke, A. A.; Schoonraad, S. A.; Fischenich, K. M.; Wahlquist, J. A.; Randolph, M. A.; Ferguson, V. L.; Bryant, S. J. Assessment and Prevention of Cartilage Degeneration Surrounding a Focal Chondral Defect in the Porcine Model. *Biochemical and Biophysical Research Communications* **2019**, *514* (3), 940–945.
- (4) Aisenbrey, E. A.; Bryant, S. J. Mechanical Loading Inhibits Hypertrophy in Chondrogenically Differentiating HMSCs within a Biomimetic Hydrogel. *J. Mater. Chem. B* **2016**, *4* (20), 3562–3574.
- (5) Pascual-Garrido, C.; Aisenbrey, E. A.; Rodriguez-Fontan, F.; Payne, K. A.; Bryant, S. J.; Goodrich, L. R. Photopolymerizable Injectable Cartilage Mimetic Hydrogel for the Treatment of Focal Chondral Lesions: A Proof of Concept Study in a Rabbit Animal Model. *Am J Sports Med* **2019**, *47* (1), 212–221.
- (6) Steinmetz, N. J.; Aisenbrey, E. A.; Westbrook, K. K.; Qi, H. J.; Bryant, S. J. Mechanical Loading Regulates Human MSC Differentiation in a Multi-Layer Hydrogel for Osteochondral Tissue Engineering. *Acta Biomaterialia* **2015**, *21*, 142–153.
- (7) Delale, F.; Erdogan, F. Interface Crack in a Nonhomogeneous Elastic Medium. *International Journal of Engineering Science* **1988**, *26* (6), 559–568.

- (8) Evans, A. G.; Rühle, M.; Dalgleish, B. J.; Charalambides, P. G. The Fracture Energy of Bimaterial Interfaces. *Metall Mater Trans A* **1990**, *21* (9), 2419–2429.
- (9) Zawko, S. A.; Suri, S.; Truong, Q.; Schmidt, C. E. Photopatterned Anisotropic Swelling of Dual-Crosslinked Hyaluronic Acid Hydrogels. *Acta Biomaterialia* **2009**, *5* (1), 14–22.
- (10) Dortdivanlioglu, B.; Yilmaz, N. E. D.; Goh, K. B.; Zheng, X.; Linder, C. Swelling-Induced Interface Crease Instabilities at Hydrogel Bilayers. *J Elast* **2021**, *145* (1), 31–47.
- (11) Erdogan, F. Fracture Mechanics of Functionally Graded Materials. *Composites Engineering* **1995**, *5* (7), 753–770.
- (12) Shbeeb, N. I.; Binienda, W. K. Analysis of an Interface Crack for a Functionally Graded Strip Sandwiched between Two Homogeneous Layers of Finite Thickness. *Engineering Fracture Mechanics* **1999**, *64* (6), 693–720.
- (13) Marur, P. R.; Tippur, H. V. Numerical Analysis of Crack-Tip Fields in Functionally Graded Materials with a Crack Normal to the Elastic Gradient. *International Journal of Solids and Structures* **2000**, *37* (38), 5353–5370.
- (14) Muralidharan, A.; Uzcategui, A. C.; McLeod, R. R.; Bryant, S. J. Stereolithographic 3D Printing for Deterministic Control over Integration in Dual-Material Composites. *Advanced Materials Technologies* **2019**, *4* (11), 1900592.
- (15) Rafiee, M.; Farahani, R. D.; Therriault, D. Multi-Material 3D and 4D Printing: A Survey. *Advanced Science* **2020**, *7* (12), 1902307.
- (16) Mirzaali, M. J.; Herranz de la Nava, A.; Gunashekar, D.; Nouri-Goushki, M.; Doubrovski, E. L.; Zadpoor, A. A. Fracture Behavior of Bio-Inspired Functionally Graded Soft–Hard Composites Made by Multi-Material 3D Printing: The Case of Colinear Cracks. *Materials* **2019**, *12* (17), 2735.
- (17) Mirzaali, M. J.; Herranz de la Nava, A.; Gunashekar, D.; Nouri-Goushki, M.; Veeger, R. P. E.; Grossman, Q.; Angeloni, L.; Ghatkesar, M. K.; Fratila-Apachitei, L. E.; Ruffoni, D.; Doubrovski, E. L.; Zadpoor, A. A. Mechanics of Bioinspired Functionally Graded Soft-Hard Composites Made by Multi-Material 3D Printing. *Composite Structures* **2020**, *237*, 111867.
- (18) Mirzaali, M. J.; Cruz Saldívar, M.; Herranz de la Nava, A.; Gunashekar, D.; Nouri-Goushki, M.; Doubrovski, E. L.; Zadpoor, A. A. Multi-Material 3D Printing of Functionally Graded Hierarchical Soft–Hard Composites. *Advanced Engineering Materials* **2020**, *22* (7), 1901142.
- (19) Zhang, T.; Lin, S.; Yuk, H.; Zhao, X. Predicting Fracture Energies and Crack-Tip Fields of Soft Tough Materials. *Extreme Mechanics Letters* **2015**, *4*, 1–8.

- (20) Nguyen, T. D.; Govindjee, S. Numerical Study of Geometric Constraint and Cohesive Parameters in Steady-State Viscoelastic Crack Growth. *International journal of fracture* **2006**, *141* (1–2), 255–268.
- (21) Gu, P.; Asaro, R. J. Crack Deflection in Functionally Graded Materials. *International Journal of Solids and Structures* **1997**, *34* (24), 3085–3098.

Chapter 5

Conclusions

5.1 Overview

Current tissue engineering strategies focus on the development of tissue engineering scaffolds using hydrogels. The ability to accurately characterize the properties of the native tissue and scaffold materials and integrate multiple hydrogel materials in a robust manner are critical to the design and successful implementation. Yet, critical gaps exist in our ability to characterize the microscale properties of soft, hydrated materials and create robust attachments between polymeric materials with divergent mechanical properties.

The studies described in the preceding chapters were conducted to 1) evaluate the influence of surface roughness on small-scale indentation property assessments of hydrogel materials, 2) to experimentally determine the influence of surface roughness on small-scale indentation property assessments of soft, hydrated tissues, and 3) evaluate the relative fracture toughness of a graded interface between polymeric materials with divergent mechanical properties. The primary findings are summarized below and suggestions for future work are discussed.

5.1 Summary of Results

Hydrogels are important materials for many applications of 3D tissue engineering. Accurate property evaluation of soft hydrogels is important for recapitulating tissue properties and for the design of novel materials for tissue regeneration. However, when testing with small indentation probes, the contributions of surface roughness remain largely unknown. The influence of surface roughness on small-scale indentation testing of hydrogel materials was evaluated through depth-sensing microindentation tests on rough and smooth agarose surfaces. Microindentation tests were performed using three different probe radii ($R_i = 50, 105,$ and $250 \mu\text{m}$) and four different displacement rates ($\dot{\delta} = 1, 5, 10,$ and $50 \mu\text{m/s}$) to characterize both the equilibrium and non-equilibrium behavior of 5 wt. %, 7.5 wt. %, and 10 wt. % agarose gels (**Chapter 2**). For each combination of probe size and displacement rate, the effective contact modulus, equilibrium modulus, and fluid load fraction was evaluated. The maximum indentation depth was related to the probe radius by $\delta_{max} = 0.05 * R_i$. The effective contact modulus, E_c , of both rough and smooth samples increased with probe radius and displacement rate. However, the effective contact modulus of the rough surface was reduced by as much as 51% as compared to the smooth surface when evaluated using the $50 \mu\text{m}$ radius probe and slowest displacement rates and by as little as 18% when evaluated using the $250 \mu\text{m}$ radius probe and fastest displacement rates. Similarly, the equilibrium modulus, E_{co} , of the rough surface was reduced by up to 47% when evaluated using the $50 \mu\text{m}$ radius probe and by 22% when evaluated using $250 \mu\text{m}$ radius probe. In contrast to the effective contact modulus, equilibrium modulus only increased with probe radius. The fluid load fraction of the rough surface was similar to those evaluated from tests on the smooth surface across all

combinations of probe size and displacement rate. Cryo-focused ion beam milling and scanning electron microscopy (Cryo-FIB/SEM) was used to evaluate the near surface morphology of rough and smooth agarose surfaces and revealed a disrupted agarose network near the surface of the rough agarose.

The increase in equilibrium modulus with probe radius and in-turn, indentation depth, combined with the findings of the Cryo-FIB/SEM imaging suggest that surface roughness has a 2-fold effect. First, surface roughness alters the relationship between probe displacement and contact area used in indentation analyses. Second, surface roughness may also act as a near-surface region of decreased stiffness. Furthermore, the converging properties between rough and smooth surfaces with increasing probe radius demonstrate that the influence of surface roughness decreases with increasing indentation depth. These findings establish an improved understanding of the influence of surface roughness on the indentation of soft, hydrated materials. The results of this work will facilitate more accurate design inputs and faster optimization of novel materials for the use of hydrogels including for tissue engineering applications.

Surface roughness may exert a profound influence over microindentation property measurements of articular cartilage and other soft tissues. Thus, the influence of surface roughness on microindentation testing was evaluated through AFM-based and depth-sensing microindentation tests of rough and smooth porcine articular cartilage surfaces (**Chapter 3**). For the depth-sensing microindentation, three probe radii ($R_i = 50, 105, \text{ and } 250 \mu\text{m}$) and four different displacement rates ($\dot{\delta} = 1, 5, 10, \text{ and } 50 \mu\text{m/s}$) to characterize both the equilibrium and non-equilibrium behavior of the rough and smooth cartilage surfaces. The effective contact

modulus, equilibrium modulus, and fluid load fraction were evaluated for each combination of probe radius and displacement rate. The effective contact modulus of the both the rough and smooth surfaces increased with probe radius and displacement rate. Additionally, the effective contact modulus of the rough surface was reduced by 95% using the 105 μm radius probe, 80% using the 50 μm radius probe and by 75% using the 250 μm probe. The equilibrium modulus increased also significantly for both samples with increasing probe radius and indentation depth. The rough surface reduced the equilibrium modulus by 94% using the 105 μm radius probe, 80% using the 50 μm radius probe and by 82% using the 250 μm probe. Fluid load fractions were approximately equal between the rough and smooth surfaces. Fluid load fraction measures the fraction of the load carried by the interstitial fluid pressurization under loading and depends on the equilibrium modulus and intrinsic permeability. Our results suggest that, in addition to altering the area of the probe in contact, the rough surface also disrupted the local collagen network, creating a near-surface region of decreased stiffness.

The AFM-based indentation was performed on the rough and smooth surfaces using two different probe sizes ($R_i = 1$ and 12.25 μm) and four different displacement rates ($\dot{\delta} = 1, 5, 10,$ and 50 $\mu\text{m/s}$) as a way to critically evaluate AFM as a tool for performing microscale property assessments of soft, hydrated materials. The effective contact moduli were reduced by up to 91% for the rough surface when indentations were made with the 12.25 μm radius probe. In contrast, there was a significant overlap in the measured effective contact moduli for the rough and smooth surfaces when indentations were performed with the 1 μm radius probe. A reduction in the measured effective moduli of the smooth sample was also found when comparing the results of AFM-based indentation and depth-sensing indentation. Taken

together the results suggest that AFM-based indentation is sensitive to the influence of surface roughness and should be avoided as a tool to characterize soft, hydrated tissues with rough surfaces.

The results from indentation testing of rough and smooth cartilage surfaces enhance our understanding of the influence of surface roughness on the indentation of soft, hydrated tissues and will facilitate more accurate characterization of the microscale properties of tissues. Researchers will be able to use this information to define more accurate design inputs for tissue engineering, achieve more meaningful comparisons between the mechanical properties and behavior of healthy and pathological tissues, and increase their ability to interpret and contextualize the results of other studies involving the microscale characterization of soft tissues.

Composite hydrogels can be used to create tissue engineer scaffolds with complex functionality (e.g., combining a mechanically robust hydrogel structure with a soft cellular environment). However, a key challenge exists in the ability to create robust interfaces between materials with divergent mechanical properties. Functionally graded interfaces (FGIs) reduce the property mismatch at dissimilar interfaces by increasing the dimension over which the property change occurs. Yet little is understood about FGIs and the potential improvements over sharp interfaces between soft materials. To address this gap in the literature, the influence of interfacial width on the fracture toughness of functionally graded interfaces will be evaluated through single-edge notch fracture testing of dissimilar polymer interfaces (**Chapter 4**). Preliminary testing failure behavior of graded specimens was strongly dependent on the relative amount of the soft phase present and the interfacial cracks did not propagate across

the specimen. However, the consistent failure of the pure soft-phase upon introduction of a functionally graded interface suggests an enhanced fracture toughness over that of a bi-material interface. A redesign of notch-fracture specimens, with the inclusion of a stiff region for gripping on either end, eliminated the failure at the grips and appears to have mitigated the influence of the size of the soft phase. Future testing should focus on evaluating the influence of interfacial width on fracture toughness as well as the fracture toughness of functional property gradients as compared to material gradients.

5.2 Discussion of future research directions

5.2.1 Experiments to further elucidate the influence of surface roughness on indentation of soft, hydrated materials.

Indentation of casted rough and smooth Agarose hydrogel surfaces with identical roughness to samples evaluated in Chapter 2. By casting rough surfaces, we can separate the influence of surface roughness from the influence of a disrupted matrix. This may explain why the influence of surface roughness persists at indentation depths beyond the scale of the surface roughness profile.

Indentation of rough and smooth Agarose surfaces in Chapter 2 were limited to two surface profiles and a single indentation depth for each probe radius used in the study. A validated finite element model would allow us to explore the influence of indentation depth separately from probe radius.

5.2.2 Translational considerations

The progression of osteoarthritis (OA) is associated with fibrillation of the articular surface, GAG loss, increased permeability, and a reduced compressive stiffness of articular cartilage compared to healthy tissue. In Chapter 3, roughened articular cartilage cross-sections were associated with a drastic reduction in the properties evaluated via indentation. However, it is unclear whether the conclusions from Chapter 3 can be translated to explain the property changes associated with OA. Hypertonic solutions eliminate the fixed charge effect of the GAGs confined within the ECM, allowing assessment of the ECM's intrinsic properties. Indentation of rough cartilage surfaces compared with indentation of smooth surfaces bathed in a hypertonic solution may permit the separation of the influence of the disrupted network from the influence of GAG loss associated with the progression of OA.

5.2.3 Further fracture testing experiments

Multi-material printing currently does not permit the additive manufacturing of continuous functional gradients between hydrogel materials. Once this technique is developed and refined, fracture toughness experiments of functional hydrogel materials should be performed to assess the role of differential swelling on fracture toughness.

Bibliography

- (1) Buckwalter, J. A.; Mankin, H. J. Articular Cartilage: Part I. *Journal of Bone and Joint Surgery, American volume* **1997**, *79* (4), 600.
- (2) Hagg, R.; Hedbom, E.; Möllers, U.; Aszódi, A.; Fässler, R.; Bruckner, P. Absence of the A1(IX) Chain Leads to a Functional Knock-out of the Entire Collagen IX Protein in Mice *. *Journal of Biological Chemistry* **1997**, *272* (33), 20650–20654.
- (3) Xu, J.; Wang, W.; Ludeman, M.; Cheng, K.; Hayami, T.; Lotz, J. C.; Kapila, S. Chondrogenic Differentiation of Human Mesenchymal Stem Cells in Three-Dimensional Alginate Gels. *Tissue Engineering Part A* **2008**, *14* (5), 667–680.
- (4) Zelenski, N. A.; Leddy, H. A.; Sanchez-Adams, J.; Zhang, J.; Bonaldo, P.; Liedtke, W.; Guilak, F. Type VI Collagen Regulates Pericellular Matrix Properties, Chondrocyte Swelling, and Mechanotransduction in Mouse Articular Cartilage. *Arthritis & Rheumatology* **2015**, *67* (5), 1286–1294.
- (5) DR, E. The Collagens of Articular Cartilage. *Sem. Arthritis Rheumatism* **1991**, *21*, 211.
- (6) Kwan, A. P.; Cummings, C. E.; Chapman, J. A.; Grant, M. E. Macromolecular Organization of Chicken Type X Collagen in Vitro. *Journal of Cell Biology* **1991**, *114* (3), 597–604.
- (7) Kääb, M. J.; Ito, K.; Clark, J. M.; Nötzli, H. P. Deformation of Articular Cartilage Collagen Structure under Static and Cyclic Loading. *Journal of Orthopaedic Research* **1998**, *16* (6), 743–751.
- (8) Korhonen, R. K.; Laasanen, M. S.; Töyräs, J.; Rieppo, J.; Hirvonen, J.; Helminen, H. J.; Jurvelin, J. S. Comparison of the Equilibrium Response of Articular Cartilage in Unconfined Compression, Confined Compression and Indentation. *J Biomech* **2002**, *35* (7), 903–909.
- (9) Buckwalter, J. A.; Mankin, H. J.; Grodzinsky, A. J. Articular Cartilage and Osteoarthritis. *Instructional Course Lectures-American Academy of Orthopaedic Surgeons* **2005**, *54*, 465.
- (10) Sokoloff, L. *Biology of Degenerative Joint Disease*. **1969**.
- (11) Sophia Fox, A. J.; Bedi, A.; Rodeo, S. A. The Basic Science of Articular Cartilage: Structure, Composition, and Function. *Sports Health* **2009**, *1* (6), 461–468.
- (12) Maroudas, A. Distribution and Diffusion of Solutes in Articular Cartilage. *Biophysical Journal* **1970**, *10* (5), 365–379.

- (13) Donnan, F. G.; Harris, A. B. CLXXVII.—The Osmotic Pressure and Conductivity of Aqueous Solutions of Congo-Red, and Reversible Membrane Equilibria. *Journal of the Chemical Society, Transactions* **1911**, 99, 1554–1577.
- (14) Maroudas, A. Physicochemical Properties of Cartilage in the Light of Ion Exchange Theory. *Biophysical Journal* **1968**, 8 (5), 575–595.
- (15) Torzilli, P. A.; Askari, E.; Jenkins, J. T. Water Content and Solute Diffusion Properties in Articular Cartilage. In *Biomechanics of Diarthrodial Joints*; Ratcliffe, A., Woo, S. L.-Y., Mow, V. C., Eds.; Springer: New York, NY, 1990; pp 363–390.
- (16) Seireg, A.; Arvikar, R. J. The Prediction of Muscular Load Sharing and Joint Forces in the Lower Extremities during Walking. *Journal of Biomechanics* **1975**, 8 (2), 89–102.
- (17) Guilak, F.; Ratcliffe, A.; Lane, N.; Rosenwasser, M. P.; Mow, V. C. Mechanical and Biochemical Changes in the Superficial Zone of Articular Cartilage in Canine Experimental Osteoarthritis. *Journal of Orthopaedic Research* **1994**, 12 (4), 474–484.
- (18) Maroudas, A.; Bannon, C. Measurement of Swelling Pressure in Cartilage and Comparison with the Osmotic Pressure of Constituent Proteoglycans. *Biorheology* **1981**, 18 (3–6), 619–632.
- (19) Chen, A. C.; Bae, W. C.; Schinagl, R. M.; Sah, R. L. Depth- and Strain-Dependent Mechanical and Electromechanical Properties of Full-Thickness Bovine Articular Cartilage in Confined Compression. *Journal of Biomechanics* **2001**, 34 (1), 1–12.
- (20) Schinagl, R. M.; Gurskis, D.; Chen, A. C.; Sah, R. L. Depth-Dependent Confined Compression Modulus of Full-Thickness Bovine Articular Cartilage. *Journal of Orthopaedic Research* **1997**, 15 (4), 499–506.
- (21) Mow, V. C.; Kuei, S. C.; Lai, W. M.; Armstrong, C. G. Biphasic Creep and Stress Relaxation of Articular Cartilage in Compression: Theory and Experiments. *Journal of Biomechanical Engineering* **1980**, 102 (1), 73–84.
- (22) Bonnevie, E. D.; Baro, V. J.; Wang, L.; Burris, D. L. Fluid Load Support during Localized Indentation of Cartilage with a Spherical Probe. *Journal of Biomechanics* **2012**, 45 (6), 1036–1041.
- (23) Moore, A. C.; Zimmerman, B. K.; Chen, X.; Lu, X. L.; Burris, D. L. Experimental Characterization of Biphasic Materials Using Rate-Controlled Hertzian Indentation. *Tribology International* **2015**, 89, 2–8.
- (24) McCutchen, C. W. The Frictional Properties of Animal Joints. *Wear* **1962**, 5 (1), 1–17.

- (25) Soltz, M. A.; Ateshian, G. A. Experimental Verification and Theoretical Prediction of Cartilage Interstitial Fluid Pressurization at an Impermeable Contact Interface in Confined Compression. *Journal of Biomechanics* **1998**, *31* (10), 927–934.
- (26) Ateshian, G. A.; Lai, W. M.; Zhu, W. B.; Mow, V. C. An Asymptotic Solution for the Contact of Two Biphasic Cartilage Layers. *Journal of Biomechanics* **1994**, *27* (11), 1347–1360.
- (27) Spilker, R. L.; Suh, J.-K.; Mow, V. C. A Finite Element Analysis of the Indentation Stress-Relaxation Response of Linear Biphasic Articular Cartilage. *Journal of Biomechanical Engineering* **1992**, *114* (2), 191–201.
- (28) Maroudas, A. Physicochemical Properties of Articular Cartilage. *Adult articular cartilage* **1979**.
- (29) Lai, W. M.; Hou, J. S.; Mow, V. C. A Triphasic Theory for the Swelling and Deformation Behaviors of Articular Cartilage. *Journal of Biomechanical Engineering* **1991**, *113* (3), 245–258.
- (30) Lu, X. L.; Sun, D. D. N.; Guo, X. E.; Chen, F. H.; Lai, W. M.; Mow, V. C. Indentation Determined Mechanochemical Properties and Fixed Charge Density of Articular Cartilage. *Annals of Biomedical Engineering* **2004**, *32* (3), 370–379.
- (31) Wahlquist, J. A.; DelRio, F. W.; Randolph, M. A.; Aziz, A. H.; Heveran, C. M.; Bryant, S. J.; Neu, C. P.; Ferguson, V. L. Indentation Mapping Revealed Poroelastic, but Not Viscoelastic, Properties Spanning Native Zonal Articular Cartilage. *Acta Biomaterialia* **2017**, *64*, 41–49.
- (32) Fischenich, K. M.; Wahlquist, J. A.; Wilmoth, R. L.; Cai, L.; Neu, C. P.; Ferguson, V. L. Human Articular Cartilage Is Orthotropic Where Microstructure, Micromechanics, and Chemistry Vary with Depth and Split-Line Orientation. *Osteoarthritis and Cartilage* **2020**, *28* (10), 1362–1372.
- (33) Chen, X.; Zimmerman, B. K.; Lu, X. L. Determine the Equilibrium Mechanical Properties of Articular Cartilage from the Short-Term Indentation Response. *Journal of Biomechanics* **2015**, *48* (1), 176–180.
- (34) Fairbank, T. J. Knee Joint Changes after Meniscectomy. *The Journal of Bone and Joint Surgery. British volume* **1948**, *30-B* (4), 664–670.
- (35) Felson, D. T.; Anderson, J. J.; Naimark, A.; Walker, A. M.; Meenan, R. F. Obesity and Knee Osteoarthritis. *Ann Intern Med* **1988**, *109* (1), 18–24.
- (36) Blazek, K.; Favre, J.; Asay, J.; Erhart-Hledik, J.; Andriacchi, T. Age and Obesity Alter the Relationship between Femoral Articular Cartilage Thickness and Ambulatory Loads in

- Individuals without Osteoarthritis. *Journal of Orthopaedic Research* **2014**, 32 (3), 394–402.
- (37) Collins, K. H.; Hart, D. A.; Seerattan, R. A.; Reimer, R. A.; Herzog, W. High-Fat/High-Sucrose Diet-Induced Obesity Results in Joint-Specific Development of Osteoarthritis-like Degeneration in a Rat Model. *Bone & Joint Research* **2018**, 7 (4), 274–281.
- (38) Reijman, M.; Pols, H. a. P.; Bergink, A. P.; Hazes, J. M. W.; Belo, J. N.; Lievense, A. M.; Bierma-Zeinstra, S. M. A. Body Mass Index Associated with Onset and Progression of Osteoarthritis of the Knee but Not of the Hip: The Rotterdam Study. *Annals of the Rheumatic Diseases* **2007**, 66 (2), 158–162.
- (39) Widmyer, M. R.; Utturkar, G. M.; Leddy, H. A.; Coleman, J. L.; Spritzer, C. E.; Moorman, C. T.; DeFrate, L. E.; Guilak, F. High Body Mass Index Is Associated With Increased Diurnal Strains in the Articular Cartilage of the Knee. *Arthritis & Rheumatism* **2013**, 65 (10), 2615–2622.
- (40) Grotle, M.; Hagen, K. B.; Natvig, B.; Dahl, F. A.; Kvien, T. K. Obesity and Osteoarthritis in Knee, Hip and/or Hand: An Epidemiological Study in the General Population with 10 Years Follow-Up. *BMC Musculoskelet Disord* **2008**, 9 (1), 132.
- (41) Martin, J. A.; Buckwalter, J. A. Aging, Articular Cartilage Chondrocyte Senescence and Osteoarthritis. *Biogerontology* **2002**, 3 (5), 257–264.
- (42) Jeon, O. H.; David, N.; Campisi, J.; Elisseeff, J. H. Senescent Cells and Osteoarthritis: A Painful Connection. *J Clin Invest* **2018**, 128 (4), 1229–1237.
- (43) Sharma, L.; Song, J.; Dunlop, D.; Felson, D.; Lewis, C. E.; Segal, N.; Torner, J.; Cooke, T. D. V.; Hietpas, J.; Lynch, J.; Nevitt, M. Varus and Valgus Alignment and Incident and Progressive Knee Osteoarthritis. *Annals of the Rheumatic Diseases* **2010**, 69 (11), 1940–1945.
- (44) Brouwer, G. M.; Tol, A. W. V.; Bergink, A. P.; Belo, J. N.; Bernsen, R. M. D.; Reijman, M.; Pols, H. a. P.; Bierma-Zeinstra, S. M. A. Association between Valgus and Varus Alignment and the Development and Progression of Radiographic Osteoarthritis of the Knee. *Arthritis & Rheumatism* **2007**, 56 (4), 1204–1211.
- (45) Lane, N. E.; Lin, P.; Christiansen, L.; Gore, L. R.; Williams, E. N.; Hochberg, M. C.; Nevitt, M. C. Association of Mild Acetabular Dysplasia with an Increased Risk of Incident Hip Osteoarthritis in Elderly White Women: The Study of Osteoporotic Fractures. *Arthritis & Rheumatism* **2000**, 43 (2), 400–404.
- (46) Gosvig, K. K.; Jacobsen, S.; Sonne-Holm, S.; Palm, H.; Troelsen, A. Prevalence of Malformations of the Hip Joint and Their Relationship to Sex, Groin Pain, and Risk of Osteoarthritis: A Population-Based Survey. *JBJS* **2010**, 92 (5), 1162–1169.

- (47) Doherty, M.; Courtney, P.; Doherty, S.; Jenkins, W.; Maciewicz, R. A.; Muir, K.; Zhang, W. Nonspherical Femoral Head Shape (Pistol Grip Deformity), Neck Shaft Angle, and Risk of Hip Osteoarthritis: A Case–Control Study. *Arthritis & Rheumatism* **2008**, *58* (10), 3172–3182.
- (48) Bardakos, N. V.; Villar, R. N. Predictors of Progression of Osteoarthritis in Femoroacetabular Impingement. *The Journal of Bone and Joint Surgery. British volume* **2009**, *91-B* (2), 162–169.
- (49) Mandelbaum, B. R.; Browne, J. E.; Fu, F.; Micheli, L.; Mosely, J. B.; Erggelet, C.; Minas, T.; Peterson, L. Articular Cartilage Lesions of the Knee. *Am J Sports Med* **1998**, *26* (6), 853–861.
- (50) Mankin, H. J. Biochemistry and Metabolism of Articular Cartilage in Osteoarthritis. *Osteoarthritis, diagnosis and medical/surgical management*. **1984**, 109–154.
- (51) Sah, R. L.; Yang, A. S.; Chen, A. C.; Hant, J. J.; Halili, R. B.; Yoshioka, M.; Amiel, D.; Coutts, R. D. Physical Properties of Rabbit Articular Cartilage after Transection of the Anterior Cruciate Ligament. *Journal of Orthopaedic Research* **1997**, *15* (2), 197–203.
- (52) Setton, L. A.; Elliott, D. M.; Mow, V. C. Altered Mechanics of Cartilage with Osteoarthritis: Human Osteoarthritis and an Experimental Model of Joint Degeneration. *Osteoarthritis and Cartilage* **1999**, *7* (1), 2–14.
- (53) Felson, D. T. Osteoarthritis as a Disease of Mechanics. *Osteoarthritis and Cartilage* **2013**, *21* (1), 10–15.
- (54) James Williams, H.; Ward, J. R.; Egger, M. J.; Neuner, R.; Brooks, R. H.; Clegg, D. O.; Field, E. H.; Skosey, J. L.; Alarcón, G. S.; Willkens, R. F.; Paulus, H. E.; Jon Russell, I.; Sharp, J. T. Comparison of Naproxen and Acetaminophen in a Two-Year Study of Treatment of Osteoarthritis of the Knee. *Arthritis & Rheumatism* **1993**, *36* (9), 1196–1206.
- (55) Bradley, J. D.; Brandt, K. D.; Katz, B. P.; Kalasinski, L. A.; Ryan, S. I. Comparison of an Antiinflammatory Dose of Ibuprofen, an Analgesic Dose of Ibuprofen, and Acetaminophen in the Treatment of Patients with Osteoarthritis of the Knee. *New England Journal of Medicine* **1991**, *325* (2), 87–91.
- (56) Clegg, D. O.; Reda, D. J.; Harris, C. L.; Klein, M. A.; O’Dell, J. R.; Hooper, M. M.; Bradley, J. D.; Bingham, C. O.; Weisman, M. H.; Jackson, C. G.; Lane, N. E.; Cush, J. J.; Moreland, L. W.; Schumacher, H. R.; Oddis, C. V.; Wolfe, F.; Molitor, J. A.; Yocum, D. E.; Schnitzer, T. J.; Furst, D. E.; Sawitzke, A. D.; Shi, H.; Brandt, K. D.; Moskowitz, R. W.; Williams, H. J. Glucosamine, Chondroitin Sulfate, and the Two in Combination for Painful Knee Osteoarthritis. *New England Journal of Medicine* **2006**, *354* (8), 795–808.

- (57) McAlindon, T. E.; LaValley, M. P.; Gulin, J. P.; Felson, D. T. Glucosamine and Chondroitin for Treatment of Osteoarthritis: A Systematic Quality Assessment and Meta-Analysis. *JAMA* **2000**, *283* (11), 1469–1475.
- (58) Reginster, J. Y.; Deroisy, R.; Rovati, L. C.; Lee, R. L.; Lejeune, E.; Bruyere, O.; Giacovelli, G.; Henrotin, Y.; Dacre, J. E.; Gossett, C. Long-Term Effects of Glucosamine Sulphate on Osteoarthritis Progression: A Randomised, Placebo-Controlled Clinical Trial. *The Lancet* **2001**, *357* (9252), 251–256.
- (59) Livesley, P.; Doherty, M.; Needoff, M.; Moulton, A. Arthroscopic Lavage of Osteoarthritic Knees. *The Journal of Bone and Joint Surgery. British volume* **1991**, *73-B* (6), 922–926.
- (60) Chang, R. W.; Falconer, J.; David Stulberg, S.; Arnold, W. J.; Manheim, L. M.; Dyer, A. R. A Randomized, Controlled Trial of Arthroscopic Surgery versus Closed-Needle Joint Lavage for Patients with Osteoarthritis of the Knee. *Arthritis & Rheumatism* **1993**, *36* (3), 289–296.
- (61) Gibson, J.; White, M.; Chapman, V.; Strachan, R. Arthroscopic Lavage and Debridement for Osteoarthritis of the Knee. *The Journal of Bone and Joint Surgery. British volume* **1992**, *74-B* (4), 534–537.
- (62) Moseley, J. B.; Wray, N. P.; Kuykendall, D.; Willis, K.; Landon, G. Arthroscopic Treatment of Osteoarthritis of the Knee: A Prospective, Randomized, Placebo-Controlled Trial: Results of a Pilot Study. *Am J Sports Med* **1996**, *24* (1), 28–34.
- (63) Kim, H. K.; Moran, M. E.; Salter, R. B. The Potential for Regeneration of Articular Cartilage in Defects Created by Chondral Shaving and Subchondral Abrasion. An Experimental Investigation in Rabbits. *J Bone Joint Surg Am* **1991**, *73* (9), 1301–1315.
- (64) Tew, S. R.; Kwan, A. P. L.; Hann, A.; Thomson, B. M.; Archer, C. W. The Reactions of Articular Cartilage to Experimental Wounding: Role of Apoptosis. *Arthritis & Rheumatism* **2000**, *43* (1), 215–225.
- (65) Mitchell, N.; Shepard, N. Effect of Patellar Shaving in the Rabbit. *Journal of Orthopaedic Research* **1987**, *5* (3), 388–392.
- (66) Hunziker, E. B.; Quinn, T. M. Surgical Removal of Articular Cartilage Leads to Loss of Chondrocytes from Cartilage Bordering the Wound Edge. *J BJS* **2003**, *85* (suppl_2), 85–92.
- (67) Glossop, N. D.; Jackson, R. W.; Koort, H. J.; Reed, S. C.; Randle, J. A. The Excimer Laser in Orthopaedics. *Clin Orthop Relat Res* **1995**, No. 310, 72–81.
- (68) Tabib, W.; Beaufils, P.; Blin, J. L.; Trémoulet, J.; Hardy, P. [Arthroscopic meniscectomy with Ho-Yag laser versus mechanical meniscectomy. Mid-term results of a randomized

- prospective study of 80 meniscectomies]. *Rev Chir Orthop Reparatrice Appar Mot* **1999**, 85 (7), 713–721.
- (69) Breinan, H. A.; Martin, S. D.; Hsu, H.-P.; Spector, M. Healing of Canine Articular Cartilage Defects Treated with Microfracture, a Type-II Collagen Matrix, or Cultured Autologous Chondrocytes. *Journal of Orthopaedic Research* **2000**, 18 (5), 781–789.
- (70) Knutsen, G.; Engebretsen, L.; Ludvigsen, T. C.; Drogset, J. O.; Grøntvedt, T.; Solheim, E.; Strand, T.; Roberts, S.; Isaksen, V.; Johansen, O. Autologous Chondrocyte Implantation Compared with Microfracture in the Knee: A Randomized Trial. *JBJS* **2004**, 86 (3), 455–464.
- (71) Mithoefer, K.; Williams, R. J. I.; Warren, R. F.; Potter, H. G.; Spock, C. R.; Jones, E. C.; Wickiewicz, T. L.; Marx, R. G. The Microfracture Technique for the Treatment of Articular Cartilage Lesions in the Knee: A Prospective Cohort Study. *JBJS* **2005**, 87 (9), 1911–1920.
- (72) Steadman, J. R.; Rodkey, W. G.; Singleton, S. B.; Briggs, K. K. Microfracture Technique Forfull-Thickness Chondral Defects: Technique and Clinical Results. *Operative Techniques in Orthopaedics* **1997**, 7 (4), 300–304.
- (73) Steadman, J. R.; Briggs, K. K.; Rodrigo, J. J.; Kocher, M. S.; Gill, T. J.; Rodkey, W. G. Outcomes of Microfracture for Traumatic Chondral Defects of the Knee: Average 11-Year Follow-Up. *Arthroscopy: The Journal of Arthroscopic & Related Surgery* **2003**, 19 (5), 477–484.
- (74) DiBartola, A. C.; Everhart, J. S.; Magnussen, R. A.; Carey, J. L.; Brophy, R. H.; Schmitt, L. C.; Flanigan, D. C. Correlation between Histological Outcome and Surgical Cartilage Repair Technique in the Knee: A Meta-Analysis. *The Knee* **2016**, 23 (3), 344–349.
- (75) Nehrer, S.; Spector, M.; Minas, T. Histologic Analysis of Tissue after Failed Cartilage Repair Procedures. *Clin Orthop Relat Res* **1999**, No. 365, 149–162.
- (76) Buckwalter, J. A.; Mow, V. C.; Ratcliffe, A. Restoration of Injured or Degenerated Articular Cartilage. *JAAOS - Journal of the American Academy of Orthopaedic Surgeons* **1994**, 2 (4), 192–201.
- (77) Knutsen, G.; Drogset, J. O.; Engebretsen, L.; Grøntvedt, T.; Isaksen, V.; Ludvigsen, T. C.; Roberts, S.; Solheim, E.; Strand, T.; Johansen, O. A Randomized Trial Comparing Autologous Chondrocyte Implantation with Microfracture: Findings at Five Years. *JBJS* **2007**, 89 (10), 2105–2112.
- (78) Saris, D. B. F.; Vanlauwe, J.; Victor, J.; Almqvist, K. F.; Verdonk, R.; Bellemans, J.; Luyten, F. P. Treatment of Symptomatic Cartilage Defects of the Knee: Characterized Chondrocyte Implantation Results in Better Clinical Outcome at 36 Months in a

- Randomized Trial Compared to Microfracture. *Am J Sports Med* **2009**, *37* (1_suppl), 10–19.
- (79) Kon, E.; Gobbi, A.; Filardo, G.; Delcogliano, M.; Zaffagnini, S.; Marcacci, M. Arthroscopic Second-Generation Autologous Chondrocyte Implantation Compared with Microfracture for Chondral Lesions of the Knee: Prospective Nonrandomized Study at 5 Years. *Am J Sports Med* **2009**, *37* (1), 33–41.
- (80) Basad, E.; Ishaque, B.; Bachmann, G.; Stürz, H.; Steinmeyer, J. Matrix-Induced Autologous Chondrocyte Implantation versus Microfracture in the Treatment of Cartilage Defects of the Knee: A 2-Year Randomised Study. *Knee surgery, sports traumatology, arthroscopy* **2010**, *18* (4), 519–527.
- (81) Saris, D. B. F.; Vanlauwe, J.; Victor, J.; Haspl, M.; Bohnsack, M.; Fortems, Y.; Vandekerckhove, B.; Almqvist, K. F.; Claes, T.; Handelberg, F.; Lagae, K.; van der Bauwhede, J.; Vandenuecker, H.; Yang, K. G. A.; Jelic, M.; Verdonk, R.; Veulemans, N.; Bellemans, J.; Luyten, F. P. Characterized Chondrocyte Implantation Results in Better Structural Repair When Treating Symptomatic Cartilage Defects of the Knee in a Randomized Controlled Trial versus Microfracture. *Am J Sports Med* **2008**, *36* (2), 235–246.
- (82) Basad, E.; Stürz, H.; Steinmeyer, J. Treatment of Chondral Defects with MACI or Microfracture. First Results of a Comparative Clinical Study. *Orthopädische Praxis* **2004**, *40*, 6–10.
- (83) Hangody, L.; Vásárhelyi, G.; Hangody, L. R.; Sükösd, Z.; Tibay, G.; Bartha, L.; Bodó, G. Autologous Osteochondral Grafting—Technique and Long-Term Results. *Injury* **2008**, *39* (1, Supplement), 32–39.
- (84) Hangody, L.; Dobos, J.; Baló, E.; Pánics, G.; Hangody, L. R.; Berkes, I. Clinical Experiences With Autologous Osteochondral Mosaicplasty in an Athletic Population: A 17-Year Prospective Multicenter Study. *Am J Sports Med* **2010**, *38* (6), 1125–1133.
- (85) Jakob, R. P.; Franz, T.; Gautier, E.; Mainil-Varlet, P. Autologous Osteochondral Grafting in the Knee: Indication, Results, and Reflections. *Clinical Orthopaedics and Related Research (1976-2007)* **2002**, *401*, 170–184.
- (86) Kock, N. B.; van Tankeren, E.; Oyen, W. J. G.; Wymenga, A. B.; van Susante, J. L. C. Bone Scintigraphy after Osteochondral Autograft Transplantation in the Knee. *Acta Orthopaedica* **2010**, *81* (2), 206–210.
- (87) Koulalis, D.; Schultz, W.; Heyden, M.; König, F. Autologous Osteochondral Grafts in the Treatment of Cartilage Defects of the Knee Joint. *Knee Surg Sports Traumatol Arthrosc* **2004**, *12* (4), 329–334.

- (88) Quarch, V. M. A.; Enderle, E.; Lotz, J.; Frosch, K.-H. Fate of Large Donor Site Defects in Osteochondral Transfer Procedures in the Knee Joint with and without TruFit Plugs. *Arch Orthop Trauma Surg* **2014**, *134* (5), 657–666.
- (89) Reverte-Vinaixa, M. M.; Joshi, N.; Díaz-Ferreiro, E. W.; Teixidor-Serra, J.; Domínguez-Oronoz, R. Medium-Term Outcome of Mosaicplasty for Grade III-IV Cartilage Defects of the Knee. *J Orthop Surg (Hong Kong)* **2013**, *21* (1), 4–9.
- (90) Harris, W. H.; Sledge, C. B. Total Hip and Total Knee Replacement. *New England Journal of Medicine* **1990**, *323* (11), 725–731.
- (91) Labek, G.; Thaler, M.; Janda, W.; Agreiter, M.; Stöckl, B. Revision Rates after Total Joint Replacement. *The Journal of Bone and Joint Surgery. British volume* **2011**, *93-B* (3), 293–297.
- (92) Erickson, I. E.; Kestle, S. R.; Zellars, K. H.; Farrell, M. J.; Kim, M.; Burdick, J. A.; Mauck, R. L. High Mesenchymal Stem Cell Seeding Densities in Hyaluronic Acid Hydrogels Produce Engineered Cartilage with Native Tissue Properties. *Acta Biomaterialia* **2012**, *8* (8), 3027–3034.
- (93) Chung, C.; Burdick, J. A. Influence of Three-Dimensional Hyaluronic Acid Microenvironments on Mesenchymal Stem Cell Chondrogenesis. *Tissue Engineering Part A* **2009**, *15* (2), 243–254.
- (94) Almeida, H. V.; Eswaramoorthy, R.; Cunniffe, G. M.; Buckley, C. T.; O’Brien, F. J.; Kelly, D. J. Fibrin Hydrogels Functionalized with Cartilage Extracellular Matrix and Incorporating Freshly Isolated Stromal Cells as an Injectable for Cartilage Regeneration. *Acta Biomaterialia* **2016**, *36*, 55–62.
- (95) Naderi-Meshkin, H.; Andreas, K.; Matin, M. M.; Sittinger, M.; Bidkhorji, H. R.; Ahmadiankia, N.; Bahrami, A. R.; Ringe, J. Chitosan-Based Injectable Hydrogel as a Promising in Situ Forming Scaffold for Cartilage Tissue Engineering. *Cell Biology International* **2014**, *38* (1), 72–84.
- (96) Chao, P.-H. G.; Yodmuang, S.; Wang, X.; Sun, L.; Kaplan, D. L.; Vunjak-Novakovic, G. Silk Hydrogel for Cartilage Tissue Engineering. *Journal of Biomedical Materials Research Part B: Applied Biomaterials* **2010**, *95B* (1), 84–90.
- (97) Noguchi, T.; Yamamuro, T.; Oka, M.; Kumar, P.; Kotoura, Y.; Hyonyt, S.-H.; Ikadat, Y. Poly(Vinyl Alcohol) Hydrogel as an Artificial Articular Cartilage: Evaluation of Biocompatibility. *Journal of Applied Biomaterials* **1991**, *2* (2), 101–107.
- (98) Oka, M.; Ushio, K.; Kumar, P.; Ikeuchi, K.; Hyon, S. H.; Nakamura, T.; Fujita, H. Development of Artificial Articular Cartilage. *Proc Inst Mech Eng H* **2000**, *214* (1), 59–68.

- (99) Maher, S. a.; Doty, S. b.; Torzilli, P. a.; Thornton, S.; Lowman, A. m.; Thomas, J. d.; Warren, R.; Wright, T. m.; Myers, E. Nondegradable Hydrogels for the Treatment of Focal Cartilage Defects. *Journal of Biomedical Materials Research Part A* **2007**, *83A* (1), 145–155.
- (100) Nguyen, L. H.; Kudva, A. K.; Saxena, N. S.; Roy, K. Engineering Articular Cartilage with Spatially-Varying Matrix Composition and Mechanical Properties from a Single Stem Cell Population Using a Multi-Layered Hydrogel. *Biomaterials* **2011**, *32* (29), 6946–6952.
- (101) Nguyen, Q. T.; Hwang, Y.; Chen, A. C.; Varghese, S.; Sah, R. L. Cartilage-like Mechanical Properties of Poly (Ethylene Glycol)-Diacrylate Hydrogels. *Biomaterials* **2012**, *33* (28), 6682–6690.
- (102) Schoonraad, S. A.; Fischenich, K. M.; Eckstein, K. N.; Crespo-Cuevas, V.; Savard, L. M.; Muralidharan, A.; Tomaschke, A. A.; Uzcategui, A. C.; Randolph, M. A.; McLeod, R. R.; Ferguson, V. L.; Bryant, S. J. Biomimetic and Mechanically Supportive 3D Printed Scaffolds for Cartilage and Osteochondral Tissue Engineering Using Photopolymers and Digital Light Processing. *Biofabrication* **2021**, *13* (4), 044106.
- (103) Zhang, X.; Yan, Z.; Guan, G.; Lu, Z.; Yan, S.; Du, A.; Wang, L.; Li, Q. Polyethylene Glycol Diacrylate Scaffold Filled with Cell-Laden Methacrylamide Gelatin/Alginate Hydrogels Used for Cartilage Repair. *J Biomater Appl* **2021**, 08853282211044853.
- (104) Aisenbrey, E. A.; Tomaschke, A.; Kleinjan, E.; Muralidharan, A.; Pascual-Garrido, C.; McLeod, R. R.; Ferguson, V. L.; Bryant, S. J. A Stereolithography-Based 3D Printed Hybrid Scaffold for In Situ Cartilage Defect Repair. *Macromolecular Bioscience* **2018**, *18* (2), 1700267.
- (105) Wichterle, O.; Lím, D. Hydrophilic Gels for Biological Use. *Nature* **1960**, *185* (4706), 117–118.
- (106) Oyen, M. L. Mechanical Characterisation of Hydrogel Materials. *International Materials Reviews* **2014**, *59* (1), 44–59.
- (107) Ahmed, E. M. Hydrogel: Preparation, Characterization, and Applications: A Review. *Journal of Advanced Research* **2015**, *6* (2), 105–121.
- (108) Oyen, M. L. Mechanical Characterisation of Hydrogel Materials. *International Materials Reviews* **2014**, *59* (1), 44–59.
- (109) Gyles, D. A.; Castro, L. D.; Silva, J. O. C.; Ribeiro-Costa, R. M. A Review of the Designs and Prominent Biomedical Advances of Natural and Synthetic Hydrogel Formulations. *European Polymer Journal* **2017**, *88*, 373–392.

- (110) Xiong, J.-Y.; Narayanan, J.; Liu, X.-Y.; Chong, T. K.; Chen, S. B.; Chung, T.-S. Topology Evolution and Gelation Mechanism of Agarose Gel. *J. Phys. Chem. B* **2005**, *109* (12), 5638–5643.
- (111) Karimi, A.; Navidbakhsh, M. Mechanical Properties of PVA Material for Tissue Engineering Applications. *Materials Technology* **2014**, *29* (2), 90–100.
- (112) Deiber, J. A.; Ottone, M. L.; Piaggio, M. V.; Peirotti, M. B. Characterization of Cross-Linked Polyampholytic Gelatin Hydrogels through the Rubber Elasticity and Thermodynamic Swelling Theories. *Polymer* **2009**, *50* (25), 6065–6075.
- (113) Fukubayashi, T.; Kurosawa, H. The Contact Area and Pressure Distribution Pattern of the Knee: A Study of Normal and Osteoarthrotic Knee Joints. *Acta Orthopaedica Scandinavica* **1980**, *51* (1–6), 871–879.
- (114) Brand, R. A. Joint Contact Stress. *Iowa Orthop J* **2005**, *25*, 82–94.
- (115) Alexopoulos, L. G.; Williams, G. M.; Upton, M. L.; Setton, L. A.; Guilak, F. Osteoarthritic Changes in the Biphasic Mechanical Properties of the Chondrocyte Pericellular Matrix in Articular Cartilage. *Journal of Biomechanics* **2005**, *38* (3), 509–517.
- (116) Gong, J. p.; Katsuyama, Y.; Kurokawa, T.; Osada, Y. Double-Network Hydrogels with Extremely High Mechanical Strength. *Advanced Materials* **2003**, *15* (14), 1155–1158.
- (117) Evans, A. G.; Rühle, M.; Dalglish, B. J.; Charalambides, P. G. The Fracture Energy of Bimaterial Interfaces. *Metall Mater Trans A* **1990**, *21* (9), 2419–2429.
- (118) Zawko, S. A.; Suri, S.; Truong, Q.; Schmidt, C. E. Photopatterned Anisotropic Swelling of Dual-Crosslinked Hyaluronic Acid Hydrogels. *Acta Biomaterialia* **2009**, *5* (1), 14–22.
- (119) Lee, Y. D.; Erdogan, F. Residual/Thermal Stresses in FGM and Laminated Thermal Barrier Coatings. *International Journal of Fracture* **1994**, *69* (2), 145–165.
- (120) Hasanov, S.; Gupta, A.; Nasirov, A.; Fidan, I. Mechanical Characterization of Functionally Graded Materials Produced by the Fused Filament Fabrication Process. *Journal of Manufacturing Processes* **2020**, *58*, 923–935.
- (121) Muralidharan, A.; Uzcategui, A. C.; McLeod, R. R.; Bryant, S. J. Stereolithographic 3D Printing for Deterministic Control over Integration in Dual-Material Composites. *Advanced Materials Technologies* **2019**, *4* (11), 1900592.
- (122) HERTZ, H. On the Contact of Elastic Solids. *Z. Reine Angew. Mathematik* **1881**, *92*, 156–171.
- (123) Boussinesq, J. *Application Des Potentiels à l'étude de l'équilibre et Du Mouvement Des Solides Élastiques: Principalement Au Calcul Des Déformations et Des Pressions Que*

Produisent, Dans Ces Solides, Des Efforts Quelconques Exercés Sur Une Petite Partie de Leur Surface Ou de Leur Intérieur: Mémoire Suivi de Notes Étendues Sur Divers Points de Physique, Mathématique et d'analyse; Gauthier-Villars, 1885; Vol. 4.

- (124) Sneddon, I. N. Boussinesq's Problem for a Rigid Cone. *Mathematical Proceedings of the Cambridge Philosophical Society* **1948**, 44 (4), 492–507.
- (125) Sneddon, I. N. The Relation between Load and Penetration in the Axisymmetric Boussinesq Problem for a Punch of Arbitrary Profile. *International journal of engineering science* **1965**, 3 (1), 47–57.
- (126) Oliver, W. C.; Pharr, G. M. An Improved Technique for Determining Hardness and Elastic Modulus Using Load and Displacement Sensing Indentation Experiments. *Journal of Materials Research* **1992**, 7 (6), 1564–1583.
- (127) Oliver, W. C.; Pharr, G. M. Measurement of Hardness and Elastic Modulus by Instrumented Indentation: Advances in Understanding and Refinements to Methodology. *Journal of Materials Research* **2004**, 19 (1), 3–20.
- (128) Tabor, D.; Taylor, G. I. A Simple Theory of Static and Dynamic Hardness. *Proceedings of the Royal Society of London. Series A. Mathematical and Physical Sciences* **1948**, 192 (1029), 247–274.
- (129) Stilwell, N. A.; Tabor, D. Elastic Recovery of Conical Indentations. *Proc. Phys. Soc.* **1961**, 78 (2), 169–179.
- (130) Bulychev, S. I. Mechanical Properties of Materials Studied from Kinetic Diagrams of Load versus Depth of Impression during Microimpression. *Prob. Prochn.* 9, 79 (1976) SI Bulychev, VP Alekhin. *Zavod Lab* **1987**, 53, 76.
- (131) Bulychev, S. I.; Alekhin, V. P.; Shorshorov, M. Kh.; Ternovskij, A. P. Mechanical Properties of Materials Studied from Kinetic Diagrams of Load versus Depth of Impression during Microimpression. *Strength Mater* **1976**, 8 (9), 1084–1089.
- (132) Bulychev, S. I.; Alekhin, V. P.; Shorshorov, M. K.; Ternovskij, A. P.; Shnyrev, G. D. Determination of Young Modulus by the Hardness Indentation Diagram. *Zavodskaya Laboratoriya* **1975**, 41 (9), 1137–1140.
- (133) Ternovskij, A. P.; Alekhin, V. P.; Shorshorov, M. K.; Khrushchev, M. M.; Skvortsov, V. N. The Character of the Variation of Microhardness with Indentation Size and the Deformation Behavior of Materials under Conditions of Concentrated Surface Loading. *Zavodskaya Laboratoriya* **1973**, 39 (1242), 20.
- (134) Shorshorov, M. K.; Bulychev, S. I.; ALEKHIN, V. The Work of Plastic and Elastic-Deformation during Indicator Impression. *DOKLADY AKADEMII NAUK SSSR* **1981**, 259 (4), 839–842.

- (135) Pethica, J. B.; Hutchings, R.; Oliver, W. C. Hardness Measurement at Penetration Depths as Small as 20 Nm. *Philosophical Magazine A* **1983**, *48* (4), 593–606.
- (136) Blau, P. J. *Microindentation Techniques in Materials Science and Engineering: A Symposium Sponsored by ASTM Committee E-4 on Metallography and by the International Metallographic Society, Philadelphia, PA, 15-18 July 1984*; Astm International, 1986.
- (137) Doerner, M. F.; Nix, W. D. A Method for Interpreting the Data from Depth-Sensing Indentation Instruments. *Journal of Materials Research* **1986**, *1* (04), 601–609.
- (138) Oyen, M. L. Spherical Indentation Creep Following Ramp Loading. *Journal of Materials Research* **2005**, *20* (08), 2094–2100.
- (139) Mattice, J. M.; Lau, A. G.; Oyen, M. L.; Kent, R. W. Spherical Indentation Load-Relaxation of Soft Biological Tissues. *Journal of Materials Research* **2006**, *21* (8), 2003–2010.
- (140) Mak, A. F.; Lai, W. M.; Mow, V. C. Biphasic Indentation of Articular Cartilage—I. Theoretical Analysis. *Journal of Biomechanics* **1987**, *20* (7), 703–714.
- (141) Mow, V. C.; Gibbs, M. C.; Lai, W. M.; Zhu, W. B.; Athanasiou, K. A. Biphasic Indentation of Articular Cartilage—II. A Numerical Algorithm and an Experimental Study. *Journal of Biomechanics* **1989**, *22* (8), 853–861.
- (142) Chaudhuri, O.; Gu, L.; Darnell, M.; Klumpers, D.; Bencherif, S. A.; Weaver, J. C.; Huebsch, N.; Mooney, D. J. Substrate Stress Relaxation Regulates Cell Spreading. *Nat Commun* **2015**, *6* (1), 6365.
- (143) Chaudhuri, O.; Gu, L.; Klumpers, D.; Darnell, M.; Bencherif, S. A.; Weaver, J. C.; Huebsch, N.; Lee, H.; Lippens, E.; Duda, G. N.; Mooney, D. J. Hydrogels with Tunable Stress Relaxation Regulate Stem Cell Fate and Activity. *Nature Materials* **2016**, *15* (3), 326–334.
- (144) Galli, M.; Oyen, M. L. Spherical Indentation of a Finite Poroelastic Coating. *Appl. Phys. Lett.* **2008**, *93* (3), 031911.
- (145) Ebenstein, D. M. Nano-JKR Force Curve Method Overcomes Challenges of Surface Detection and Adhesion for Nanoindentation of a Compliant Polymer in Air and Water. *Journal of Materials Research* **2011**, *26* (08), 1026–1035.
- (146) Ebenstein, D. M.; Wahl, K. J. A Comparison of JKR-Based Methods to Analyze Quasi-Static and Dynamic Indentation Force Curves. *Journal of Colloid and Interface Science* **2006**, *298* (2), 652–662.
- (147) Kohn, J. C.; Ebenstein, D. M. Eliminating Adhesion Errors in Nanoindentation of Compliant Polymers and Hydrogels. *Journal of the Mechanical Behavior of Biomedical Materials* **2013**, *20*, 316–326.

- (148) Johnson, K. L.; Kendall, K.; Roberts, A. D. Surface Energy and the Contact of Elastic Solids. *Proceedings of the Royal Society A: Mathematical, Physical and Engineering Sciences* **1971**, *324* (1558), 301–313.
- (149) Holm, R. Wissenschaftliche Veröffentlichungen Aus Den Siemens. *Werken* **1929**, *7* (2), 217–258.
- (150) Archard, J. F.; Allibone, T. E. Elastic Deformation and the Laws of Friction. *Proceedings of the Royal Society of London. Series A. Mathematical and Physical Sciences* **1957**, *243* (1233), 190–205.
- (151) Greenwood, J. A.; Johnson, K. L.; Matsubara, E. A Surface Roughness Parameter in Hertz Contact. *Wear* **1984**, *100* (1), 47–57.
- (152) Xia, Y.; Bigerelle, M.; Marteau, J.; Mazeran, P.-E.; Bouvier, S.; Iost, A. Effect of Surface Roughness in the Determination of the Mechanical Properties of Material Using Nanoindentation Test. *Scanning* **2014**, *36* (1), 134–149.
- (153) Wai, S. W.; Spinks, G. M.; Brown, H. R.; Swain, M. Surface Roughness: Its Implications and Inference with Regards to Ultra Microindentation Measurements of Polymer Mechanical Properties. *Polymer Testing* **2004**, *23* (5), 501–507.
- (154) Chung, S. M.; Yap, A. U. J. Effects of Surface Finish on Indentation Modulus and Hardness of Dental Composite Restoratives. *Dental Materials* **2005**, *21* (11), 1008–1016.
- (155) Donnelly, E.; Baker, S. P.; Boskey, A. L.; van der Meulen, M. C. H. Effects of Surface Roughness and Maximum Load on the Mechanical Properties of Cancellous Bone Measured by Nanoindentation. *J Biomed Mater Res A* **2006**, *77* (2), 426–435.
- (156) Qasmi, M.; Delobelle, P. Influence of the Average Roughness Rms on the Precision of the Young's Modulus and Hardness Determination Using Nanoindentation Technique with a Berkovich Indenter. *Surface and Coatings Technology* **2006**, *201* (3), 1191–1199.
- (157) Miller, M.; Bobko, C.; Vandamme, M.; Ulm, F.-J. Surface Roughness Criteria for Cement Paste Nanoindentation. *Cement and Concrete Research* **2008**, *38* (4), 467–476.
- (158) Chen, Z.; Diebels, S. Modelling and Parameter Re-Identification of Nanoindentation of Soft Polymers Taking into Account Effects of Surface Roughness. *Computers & Mathematics with Applications* **2012**, *64* (9), 2775–2786.
- (159) Ritchie, R. O.; Liu, D. Chapter 2 - Foundations of Fracture Mechanics. In *Introduction to Fracture Mechanics*; Ritchie, R. O., Liu, D., Eds.; Elsevier, 2021; pp 3–9.
- (160) Irwin, G. R. *Onset of Fast Crack Propagation in High Strength Steel and Aluminum Alloys*; Naval Research Lab Washington DC, 1956.

- (161) Zhang, T.; Lin, S.; Yuk, H.; Zhao, X. Predicting Fracture Energies and Crack-Tip Fields of Soft Tough Materials. *Extreme Mechanics Letters* **2015**, *4*, 1–8.
- (162) Creton, C.; Ciccotti, M. Fracture and Adhesion of Soft Materials: A Review. *Rep. Prog. Phys.* **2016**, *79* (4), 046601.
- (163) Mayumi, K.; Guo, J.; Narita, T.; Hui, C. Y.; Creton, C. Fracture of Dual Crosslink Gels with Permanent and Transient Crosslinks. *Extreme Mechanics Letters* **2016**, *6*, 52–59.
- (164) Greensmith, H. W. Rupture of Rubber. X. The Change in Stored Energy on Making a Small Cut in a Test Piece Held in Simple Extension. *Journal of Applied Polymer Science* **1963**, *7* (3), 993–1002.
- (165) Lee, W. Y.; Stinton, D. P.; Berndt, C. C.; Erdogan, F.; Lee, Y.-D.; Mutasim, Z. Concept of Functionally Graded Materials for Advanced Thermal Barrier Coating Applications. *Journal of the American Ceramic Society* **1996**, *79* (12), 3003–3012.
- (166) Delale, F.; Erdogan, F. Interface Crack in a Nonhomogeneous Elastic Medium. *International Journal of Engineering Science* **1988**, *26* (6), 559–568.
- (167) Chen, Y. F.; Erdogan, F. The Interface Crack Problem for a Nonhomogeneous Coating Bonded to a Homogeneous Substrate. *Journal of the Mechanics and Physics of Solids* **1996**, *44* (5), 771–787.
- (168) Shbeeb, N. I.; Binienda, W. K. Analysis of an Interface Crack for a Functionally Graded Strip Sandwiched between Two Homogeneous Layers of Finite Thickness. *Engineering Fracture Mechanics* **1999**, *64* (6), 693–720.
- (169) Marur, P. R.; Tippur, H. V. Numerical Analysis of Crack-Tip Fields in Functionally Graded Materials with a Crack Normal to the Elastic Gradient. *International Journal of Solids and Structures* **2000**, *37* (38), 5353–5370.
- (170) Mirzaali, M. J.; Herranz de la Nava, A.; Gunashekar, D.; Nouri-Goushki, M.; Veeger, R. P. E.; Grossman, Q.; Angeloni, L.; Ghatkesar, M. K.; Fratila-Apachitei, L. E.; Ruffoni, D.; Doubrovski, E. L.; Zadpoor, A. A. Mechanics of Bioinspired Functionally Graded Soft-Hard Composites Made by Multi-Material 3D Printing. *Composite Structures* **2020**, *237*, 111867.
- (171) Galli, M.; Comley, K. S. C.; Shean, T. A. V.; Oyen, M. L. Viscoelastic and Poroelastic Mechanical Characterization of Hydrated Gels. *Journal of Materials Research* **2009**, *24* (03), 973–979.
- (172) Mow, V. C.; Gibbs, M. C.; Lai, W. M.; Zhu, W. B.; Athanasiou, K. A. Biphasic Indentation of Articular Cartilage—II. A Numerical Algorithm and an Experimental Study. *Journal of Biomechanics* **1989**, *22* (8), 853–861.

- (173) Hu, Y.; Zhao, X.; Vlassak, J. J.; Suo, Z. Using Indentation to Characterize the Poroelasticity of Gels. *Applied Physics Letters* **2010**, *96* (12), 121904.
- (174) Bush, B. G.; Shapiro, J. M.; DelRio, F. W.; Cook, R. F.; Oyen, M. L. Mechanical Measurements of Heterogeneity and Length Scale Effects in PEG-Based Hydrogels. *Soft Matter* **2015**, *11* (36), 7191–7200.
- (175) Meier, Y. A.; Zhang, K.; Spencer, N. D.; Simic, R. Linking Friction and Surface Properties of Hydrogels Molded Against Materials of Different Surface Energies. *Langmuir* **2019**, *35* (48), 15805–15812.
- (176) Gombert, Y.; Simič, R.; Roncoroni, F.; Dübner, M.; Geue, T.; Spencer, N. D. Structuring Hydrogel Surfaces for Tribology. *Advanced Materials Interfaces* **2019**, *6* (22), 1901320.
- (177) Johnson, C. L.; Dunn, A. C. Tribological Characterization of Gradient-Density Polyacrylamide Hydrogel Surfaces. *Exp Mech* **2021**, *61* (5), 829–842.
- (178) Ebenstein, D. M. Nano-JKR Force Curve Method Overcomes Challenges of Surface Detection and Adhesion for Nanoindentation of a Compliant Polymer in Air and Water. *Journal of Materials Research* **2011**, *26* (08), 1026–1035.
- (179) Oyen, M. L.; Shean, T. A. V.; Strange, D. G. T.; Galli, M. Size Effects in Indentation of Hydrated Biological Tissues. *Journal of Materials Research* **2012**, *27* (1), 245–255.
- (180) Normand, V.; Lootens, D. L.; Amici, E.; Plucknett, K. P.; Aymard, P. New Insight into Agarose Gel Mechanical Properties. *Biomacromolecules* **2000**, *1* (4), 730–738.
- (181) Moore, A. C.; Burris, D. L. Tribological and Material Properties for Cartilage of and throughout the Bovine Stifle: Support for the Altered Joint Kinematics Hypothesis of Osteoarthritis. *Osteoarthritis and Cartilage* **2015**, *23* (1), 161–169.
- (182) Stolz, M.; Raiteri, R.; Daniels, A. U.; VanLandingham, M. R.; Baschong, W.; Aebi, U. Dynamic Elastic Modulus of Porcine Articular Cartilage Determined at Two Different Levels of Tissue Organization by Indentation-Type Atomic Force Microscopy. *Biophysical Journal* **2004**, *86* (5), 3269–3283.
- (183) Loparic, M.; Wirz, D.; Daniels, A. U.; Raiteri, R.; VanLandingham, M. R.; Guex, G.; Martin, I.; Aebi, U.; Stolz, M. Micro- and Nanomechanical Analysis of Articular Cartilage by Indentation-Type Atomic Force Microscopy: Validation with a Gel-Microfiber Composite. *Biophysical Journal* **2010**, *98* (11), 2731–2740.
- (184) Paietta, R. C.; Campbell, S. E.; Ferguson, V. L. Influences of Spherical Tip Radius, Contact Depth, and Contact Area on Nanoindentation Properties of Bone. *Journal of Biomechanics* **2011**, *44* (2), 285–290.

- (185) Richard, F.; Villars, M.; Thibaud, S. Viscoelastic Modeling and Quantitative Experimental Characterization of Normal and Osteoarthritic Human Articular Cartilage Using Indentation. *Journal of the Mechanical Behavior of Biomedical Materials* **2013**, *24*, 41–52.
- (186) Stolz, M.; Gottardi, R.; Raiteri, R.; Miot, S.; Martin, I.; Imer, R.; Staufer, U.; Raducanu, A.; Düggelein, M.; Baschong, W.; Daniels, A. U.; Friederich, N. F.; Aszodi, A.; Aebi, U. Early Detection of Aging Cartilage and Osteoarthritis in Mice and Patient Samples Using Atomic Force Microscopy. *Nature Nanotechnology* **2009**, *4* (3), 186–192.
- (187) Yoshioka, M.; Coutts, R. D.; Amiel, D.; Hacker, S. A. Characterization of a Model of Osteoarthritis in the Rabbit Knee. *Osteoarthritis and Cartilage* **1996**, *4* (2), 87–98.
- (188) Desrochers, J.; Amrein, M. A.; Matyas, J. R. Structural and Functional Changes of the Articular Surface in a Post-Traumatic Model of Early Osteoarthritis Measured by Atomic Force Microscopy. *Journal of Biomechanics* **2010**, *43* (16), 3091–3098.
- (189) Cooke, M. E.; Lawless, B. M.; Jones, S. W.; Grover, L. M. Matrix Degradation in Osteoarthritis Primes the Superficial Region of Cartilage for Mechanical Damage. *Acta Biomaterialia* **2018**, *78*, 320–328.
- (190) Krishnan, R.; Caligaris, M.; Mauck, R. L.; Hung, C. T.; Costa, K. D.; Ateshian, G. A. Removal of the Superficial Zone of Bovine Articular Cartilage Does Not Increase Its Frictional Coefficient. *Osteoarthritis and Cartilage* **2004**, *12* (12), 947–955.
- (191) Chandran, P. L.; Dimitriadis, E. K.; Mertz, E. L.; Horkay, F. Microscale Mapping of Extracellular Matrix Elasticity of Mouse Joint Cartilage: An Approach to Extracting Bulk Elasticity of Soft Matter with Surface Roughness. *Soft Matter* **2018**, *14* (15), 2879–2892.
- (192) Hutter, J. L.; Bechhoefer, J. Calibration of Atomic-force Microscope Tips. *Review of Scientific Instruments* **1993**, *64* (7), 1868–1873.
- (193) Long, R.; Hall, M. S.; Wu, M.; Hui, C.-Y. Effects of Gel Thickness on Microscopic Indentation Measurements of Gel Modulus. *Biophysical Journal* **2011**, *101* (3), 643–650.
- (194) Korhonen, R. K.; Wong, M.; Arokoski, J.; Lindgren, R.; Helminen, H. J.; Hunziker, E. B.; Jurvelin, J. S. Importance of the Superficial Tissue Layer for the Indentation Stiffness of Articular Cartilage. *Medical Engineering & Physics* **2002**, *24* (2), 99–108.
- (195) Li, L. P.; Soulhat, J.; Buschmann, M. D.; Shirazi-Adl, A. Nonlinear Analysis of Cartilage in Unconfined Ramp Compression Using a Fibril Reinforced Poroelastic Model. *Clinical Biomechanics* **1999**, *14* (9), 673–682.
- (196) Soulhat, J.; Buschmann, M. D.; Shirazi-Adl, A. A Fibril-Network-Reinforced Biphasic Model of Cartilage in Unconfined Compression. *Journal of Biomechanical Engineering* **1999**, *121* (3), 340–347.

- (197) Aisenbrey, E. A.; Tomaschke, A. A.; Schoonraad, S. A.; Fischenich, K. M.; Wahlquist, J. A.; Randolph, M. A.; Ferguson, V. L.; Bryant, S. J. Assessment and Prevention of Cartilage Degeneration Surrounding a Focal Chondral Defect in the Porcine Model. *Biochemical and Biophysical Research Communications* **2019**, *514* (3), 940–945.
- (198) Aisenbrey, E. A.; Bryant, S. J. Mechanical Loading Inhibits Hypertrophy in Chondrogenically Differentiating HMSCs within a Biomimetic Hydrogel. *J. Mater. Chem. B* **2016**, *4* (20), 3562–3574.
- (199) Pascual-Garrido, C.; Aisenbrey, E. A.; Rodriguez-Fontan, F.; Payne, K. A.; Bryant, S. J.; Goodrich, L. R. Photopolymerizable Injectable Cartilage Mimetic Hydrogel for the Treatment of Focal Chondral Lesions: A Proof of Concept Study in a Rabbit Animal Model. *Am J Sports Med* **2019**, *47* (1), 212–221.
- (200) Steinmetz, N. J.; Aisenbrey, E. A.; Westbrook, K. K.; Qi, H. J.; Bryant, S. J. Mechanical Loading Regulates Human MSC Differentiation in a Multi-Layer Hydrogel for Osteochondral Tissue Engineering. *Acta Biomaterialia* **2015**, *21*, 142–153.
- (201) Dortdivanlioglu, B.; Yilmaz, N. E. D.; Goh, K. B.; Zheng, X.; Linder, C. Swelling-Induced Interface Crease Instabilities at Hydrogel Bilayers. *J Elast* **2021**, *145* (1), 31–47.
- (202) Erdogan, F. Fracture Mechanics of Functionally Graded Materials. *Composites Engineering* **1995**, *5* (7), 753–770.
- (203) Rafiee, M.; Farahani, R. D.; Therriault, D. Multi-Material 3D and 4D Printing: A Survey. *Advanced Science* **2020**, *7* (12), 1902307. <https://doi.org/10.1002/adv.201902307>.
- (204) Mirzaali, M. J.; Herranz de la Nava, A.; Gunashekar, D.; Nouri-Goushki, M.; Doubrovski, E. L.; Zadpoor, A. A. Fracture Behavior of Bio-Inspired Functionally Graded Soft–Hard Composites Made by Multi-Material 3D Printing: The Case of Colinear Cracks. *Materials* **2019**, *12* (17), 2735.
- (205) Mirzaali, M. J.; Cruz Saldívar, M.; Herranz de la Nava, A.; Gunashekar, D.; Nouri-Goushki, M.; Doubrovski, E. L.; Zadpoor, A. A. Multi-Material 3D Printing of Functionally Graded Hierarchical Soft–Hard Composites. *Advanced Engineering Materials* **2020**, *22* (7), 1901142.
- (206) Nguyen, T. D.; Govindjee, S. Numerical Study of Geometric Constraint and Cohesive Parameters in Steady-State Viscoelastic Crack Growth. *International journal of fracture* **2006**, *141* (1–2), 255–268.
- (207) Gu, P.; Asaro, R. J. Crack Deflection in Functionally Graded Materials. *International Journal of Solids and Structures* **1997**, *34* (24), 3085–3098.